Enhancing Backscatter Communication Networks: Optimization and Integration with Emerging Technologies

by

Azar Hakimi Najafabadi

A thesis submitted in partial fulfillment of the requirements for the degree of

Doctor of Philosophy

in

Communications

Department of Electrical and Computer Engineering
University of Alberta

Abstract

Future wireless networks require low cost, high spectral efficiency, and high energy efficiency. To achieve these goals, backscatter communication (BackComm) networks rely on passive reflective backscatter devices (tags). However, passive transmission causes low data rates and ranges. To address these, this thesis aims to address (1) BackComm optimization algorithms and (2) integration of BackComm with other wireless technologies.

The thesis starts with examining a monostatic backscatter Communication (Monostatic BackComm) network consisting of multiple tags with a full-duplex (FD) multiple-input multiple-output (MIMO) reader (backscatter receiver) that is subject to self-interference (SI), which reduces the achievable data rate, throughput, and coverage. Practical SI cancellation methods cannot fully remove it but rather leave residual self-interference (RSI). Thus, to remedy this problem, an algorithm is designed to optimize the reader's precoder and combiner filters and the tag reflection coefficients. The constraints limit the effects of the RSI and allow the energy harvested by the tags to exceed a minimum.

To enhance spectral efficiency, this thesis integrates BackComm as a secondary network with a downlink non-orthogonal multiple access (NOMA) system as the primary network in a spectrum-sharing environment. In the secondary network, backscatter device (BD) reflects the primary signal while modulating its data onto it. An intelligent reflecting surface (IRS) with backscattering is integrated as a BD to leverage its transmit diversity. The downlink NOMA users are the cooperative receivers who decode both primary and secondary signals. However, a power-splitting (PS) technique is proposed to prevent interference where the downlink signal can be split into modulated and unmodulated parts. Then, the IRS uses

the latter to transfer its data. It is shown that the interference from the secondary system (IRS-backscattering) on the primary system can be controlled without any performance degradation.

Cooperative symbiotic radio (SR) backscattering is introduced within a spectrum-sharing system. The primary motivation is to address the Backcomm limitations by exploiting an active node, such as the User Equipment (UE). An innovative system model comprising two transmission phases is proposed to achieve this objective. The initial phase involves a traditional SR phase, where the assigned BD utilizes the UE's uplink signal to modulate its data towards a common base station (BS). In the subsequent phase, the UE decodes and embeds the associate BD's signal within its data, employing power splitting techniques to allocate distinct power levels to each stream. The analysis of this system encompasses the throughput optimization for both UE and BD.

Also, integrated sensing and communication (ISAC) has emerged to improve spectrum utilization. The thesis proposes an integrated sensing and SR network to study the coexistence and spectrum-sharing among systems. The downlink system leverages SR assisted by an IRS-empowered BackComm system, while the uplink BS performs target sensing. System parameters are optimized to maximize the communication rate while ensuring that sensing and backscatter signals meet their required quality of service (QoS).

Preface

The essential content of Chapter 3 is published in the following journal and conference papers:

- **A. Hakimi**, S. Zargari, C. Tellambura, S. Herath, "Sum Rate Maximization of MIMO Monostatic Backscatter Networks by Suppressing Residual SelfInterference," IEEE Trans. On Comm., vol. 71, no. 1, pp.512-526, Nov. 2022.

- **A. Hakimi**, S. Zargari, C. Tellambura, and S. Herath, " Sum Rate Maximization of Full-Duplex MIMO Monostatic Backscatter Networks Under Residual Self-Interference," IEEE 17th Canadian Workshop on Information Theory (CWIT), pp.103-108, Jun 2022.

The essential content of Chapter 4 is published in the following journal paper:

- **A. Hakimi**, S. Zargari, C. Tellambura, and S. Herath, "IRS-Enabled Backscattering in a Downlink Non-Orthogonal Multiple Access System", Commun. Lett., vol. 26, no. 12, pp. 2984-2988, Sep. 2022.

The essential content of Chapter 5 is submitted in the following journal paper:

- **A. Hakimi**, S. Zargari, C. Tellambura, "Efficient Resource Management in Uplink Symbiotic and Cooperative Backscatter Networks," submitted to IEEE Comm. Lett. On Comm., Jun. 2024.

The essential content of Chapter 6 is accepted in the following journal paper:

- **A. Hakimi**, S. Zargari, C. Tellambura, "IRS-Empowered Backscatter Communication Within a Broadcasting ISAC System," accepted to IEEE Wirel. Commun. Lett. Sep. 2024.

For each publication listed above, I was responsible for developing the system model, performing the mathematical analysis, and conducting the computer simulations under the supervision of Prof. Chintha Tellambura, and in collaboration with Dr. Sanjeewa Herath and Shayan Zargari for Chapters 3 and 4. I led the manuscript writing, with contributions to the content and writing from Prof. Chintha Tellambura and Shayan Zargari.

To My Family

Acknoledgments

I am proud to thank those who made this thesis possible. Without the direction and aid of several individuals who, in one way or another, contributed and extended their valued support in the preparation and completion of this study, it would not have been feasible.

First and foremost, I would like to express my deepest appreciation to my supervisor, Prof. Chintha Tellambura, for the opportunity to pursue this PhD degree under his guidance. Prof. Tellambura's tremendous support, invaluable advice, and rigorous research attitude have been instrumental throughout my research journey, and for this, I am truly grateful.

I would also like to extend my heartfelt gratitude to my colleagues and collaborators for the insightful discussions, as well as their valuable suggestions and feedback on my work. Additionally, I wish to acknowledge the financial support provided by Huawei Canada.

Finally, I express my heartfelt gratitude to my family, particularly my parents for their unwavering support and encouragement throughout the years. I dedicate this thesis to my resilient grandmother, who instilled toughness and strength in me. In loving memory, I would like to dedicate this thesis to the gentle spirit of my grandfather, who taught me valuable lessons on the significance of kindness and generosity, not just towards others but also towards oneself. Also, I would like to dedicate this thesis to my sister whose constant presence and unwavering support have been invaluable. I am beyond lucky to have been gifted a sister like her.

Contents

List of Tables

List of Figures

List of Notations

Notation	Meaning
Boldface lower case letters (e.g. $\mathbf{a}$)	Vectors
Boldface capital case letters (e.g. $\mathbf{A}$)	Matrices
$\mathbf{A}^H$	Hermitian conjugate transpose
$\mathbf{A}^T$	Transpose
$\mathrm{Tr}(\mathbf{A})$	Trace
$\|\|\mathbf{A}\|\|_*$	Trace norm
$\mathrm{Rank}(\mathbf{A})$	Rank
$\mathbf{A}^\star$	Conjugate
$\mathbf{A} \succeq \mathbf{0}$	Positive semidefinite matrix
$\nabla_{\mathbf{x}} f(\mathbf{x})$	Gradient vector over $\mathbf{x}$
$\mathbf{I}_M$	M-by-M identity matrix
$\mathrm{diag}(\cdot)$	Diagonalization operation
$\|\cdot\|$	Euclidean norm of a complex vector
$\|\cdot\|$	Absolute value of a complex scalar
$\mathcal{C}^{M\times N}$	$M \times N$ dimensional complex matrix
$\mathbb{E}[\cdot]$	The expectation operator
$f_X(.)$	The probability density function of variable X
$F_X(.)$	The cumulative distribution function of variable X
$\mathcal{CN}(\boldsymbol{\mu}, \mathbf{C})$	Circularly symmetric complex Gaussian (CSCG) variable with mean $\boldsymbol{\mu}$ and covariance matrix $\mathbf{C}$

List of Acronyms

Ambient BackComm ambient backscatter communication.

AO alternating optimization.

AP access point.

ASK amplitude-shift keying.

BackComm backscatter communication.

BD backscatter device.

BER bit error rate.

Bistatic BackComm bistatic backscatter communication.

BPSK binary phase-shift keying.

BS base station.

CSI channel state information.

EH energy harvesting.

FD full-duplex.

FSK frequency-shift keying.

HD half-duplex.

IoT Internet of things.

IRS intelligent reflecting surface.

ISAC integrated sensing and communication.

MIMO multiple-input multiple-output.

MISO multiple-input single-output.

Monostatic BackComm monostatic backscatter Communication.

NOMA non-orthogonal multiple access.

OMA orthogonal multiple access.

OOK on-off keying.

PS power-splitting.

PSK phase-shift keying.

QoS quality of service.

RF radio frequency.

RFID radio frequency identification.

RSI residual self-interference.

SCA successive convex approximation.

SDMA spatial domain multiple access.

SDP semi-definite programming.

SDR semi-definite relaxation.

SI self-interference.

SIC successive interference cancellation.

SINR signal-to-interference-plus-noise ratio.

SNR signal-to-noise ratio.

SR symbiotic radio.

TDMA time-division multiple access.

WPCN wireless-powered communication Network.

Chapter 1

Introduction

This chapter outlines the motivation for this thesis, emphasizing the need for advanced communication techniques to improve backscatter communication (BackComm) performance, which is crucial for Internet of things (IoT) applications. It identifies research challenges and gaps where existing techniques fail to handle weak, backscattered signals and interference. The chapter also details the thesis's contributions and provides an overview of its organization.

1.1 Motivation

The explosive growth of networked sensors and devices is leading to the IoT networks. Passive IoT, according to 3GPP (3rd Generation Partnership Project), refers to a specific category of IoT devices that do not actively transmit signals but instead rely on external sources for their functionality [1]. These devices typically operate in a mode where they do not initiate communications but respond to incoming signals or commands from the network or other active devices.

Passive IoT addresses the demand for low-cost, low-power devices, making batteryless solutions highly desirable due to their cost-effectiveness and minimal power consumption. Additionally, they reduce logistical challenges related to battery recharging and replacement, as well as associated environmental costs. While wireless energy harvesting (EH) can power IoT devices, conventional power-hungry components like mixers, oscillators, and analog-to-

digital converters make exclusive reliance on EH inefficient [2–5].

Key characteristics of passive IoT devices, according to 3GPP, include [1, 6]:

1. **No Active Transmission:** These devices do not actively send signals or data packets on their own initiative. They remain dormant until triggered by external stimuli.

2. **Activation by External Signals:** Passive IoT devices are designed to wake up or respond when they receive signals or commands from active devices or the network. This helps conserve energy and resources.

3. **Energy Efficiency:** By minimizing active transmissions, passive IoT devices can conserve battery power and extend operational lifetimes without frequent recharging or battery replacement.

4. **Use Cases:** Typical applications of passive IoT devices include sensors that activate in response to proximity, environmental changes, or specific triggers. They are often used when intermittent monitoring or event-driven data collection is sufficient. For instance, the logistics sector is one of the IoT's most demanding markets. Based on the forecast, global parcel volume is expected to reach 220–262 billion by 2026 [1, 6].

In summary, the 3GPP defines passive IoT devices as characterized by their energy-efficient behavior, reliance on external triggers for activation, and minimal or no active transmission capabilities on their own accord. These features make them suitable for applications where energy consumption and network lifetime are critical factors.

In response to these needs, BackComm has emerged as a critical enabler of passive IoT [2,7–10]. The key principle is that the backscatter device (BD), also referred to as a tag[1], utilizes passive reflection rather than active transmission for data communication. Unlike traditional devices, the BD lacks an active radio frequency (RF) chain to generate RF signals for data conveyance. Instead, it relies solely on passive components, such as antennas and switches, to modulate its data onto incident RF signals from an external source and reflect the modulated signal. As a result, the power consumption of BD is reduced dramatically,

[1]Throughout this thesis, BD and tag are used interchangeably to refer to the passive reflector.

and EH may be sufficient to achieve the BD's functions even without an onboard battery. More details on the Backcomm functionalities and architecture can be found in Chapter 2.

However, like many technological innovations, BackComm has advantages and disadvantages. While it is energy efficient, where BDs operate without power-hungry active RF components, it significantly compromises data rate and coverage. Additionally, it is an interference-limited system.

1.2 BackComm Research Challenges

Here are the key research challenges:

1. **Poor performance:** BackComm systems exhibit notable poor performance, including limited transmission range (< 1m) and a constrained data rate ($\sim$ 1Kbps) [4, 7]. However, according to 3GPP requirements, these networks must support data rates of $10-100$ Kbps to accommodate a variety of applications, providing coverage of $100-200$ meters for industrial applications and $10-20$ meters for smart home applications [11].

   While prior works have attempted to enhance range through bistatic BackComm configurations, focusing on factors such as antenna design, tag's modulation [12] and proposing long-range (LoRa) BackComm [13], this thesis primarily aims to address this bottleneck by optimizing system parameters.

2. **Signal detection at the reader:** The backscatter link is inherently weak, given the passive nature of the tag, which lacks signal amplification. Additionally, the backscatter link is susceptible to a dyadic channel effect, as it depends on external sources power and carrier signal (more details in Section 2.4). Consequently, the tag signals may quickly become attenuated or buried by stronger interference sources, such as an ambient RF source signal, which hinder tag signal detection by the reader [14].

   Subsequently, prior research efforts have focused on addressing these BackComm challenges. For instance, [15, 16] delves into detecting tag signals amidst RF carrier source interference. In [15], the authors propose interference cancellation techniques leveraging the structure of RF carrier emitters and coding during tag signal transmission.

They introduce optimal and energy detectors, characterizing the performance of analytical bit error rate (BER). Meanwhile, [16] explores the simultaneous operation of a commercial Bluetooth chipset alongside a carrier source, emphasizing carrier signal suppression achieved up to 50 dB.

This thesis contributes to addressing this challenge. While the aforementioned works have focused on interference removal for tag signal detection, this thesis concentrates on system parameter design for the reader and interference management. These topics are discussed in Chapter 3 and Chapter 5.

3. **Poor spectral efficiency:** The total number of global passive IoT devices is projected to reach 29.7 billion by 2027 [3]. A study indicates that supporting IoT applications in healthcare, utilities, and motorways alone would require 76 GHz of spectrum if each service were allocated a dedicated frequency band [17]. Therefore, spectrum-efficient BackComm solutions are needed.

   Subsequently, spectrum-sharing networks significantly influence BackComm and necessitate further exploration [18, 19]. For example, [18] examines underlay cognitive backscatter systems where primary access points simultaneously transmit primary signals and receive backscatter signals in a full-Duplex manner. Conversely, [19] proposes ambient backscatter-based spectrum-sharing networks coexisting with cellular primary networks, introducing attenuation factors to manage transmit power and interference thresholds.

   This thesis addresses this challenge by incorporating symbiotic radio (SR) as a spectrum-friendly technique into BackComm. Despite cognitive spectrum sharing, SR is capable of managing RF source signal interference, as explored in Chapters 4, 5, and 6.

4. **Self-interference and mutual interference:** BackComm systems are interference-limited. The primary sources of interference are self-interference (SI) in Monostatic BackComm (manifesting as RF source interference in ambient backscatter communication (Ambient BackComm)) and mutual interference among tags in multi-tag scenarios. Both significantly impact BackComm system performance.

A previous study [20] introduces Reflective Intelligent Surface (RIS)-assisted ambient backscatter communication, focusing on RIS phase-shift designs to minimize RF source and RIS cascaded link interference at the receiver. Similarly, [21] optimizes system parameters to mitigate RF source interference. To address mutual interference, [21–23] propose orthogonal-based resource allocation among tags to prevent mutual interference.

This thesis also contributes to addressing the interference limitations in BackComm through signal and system parameter design. Specifically, it focuses on suppressing and controlling SI and mutual interference in Chapter 3 while managing RF source interference in Chapters 4, 5, and 6.

More literature reviews on these challenges are available in individual chapters and Chapter 2. However, many open research challenges in BackComm still need to be addressed. These aspects require further exploration beyond what has been studied in [20–23] and the references therein. This thesis aims to explore several BackComm setups to bridge existing research gaps and advance the field. Robust system setups are designed for practical scenarios like multi-tag environments with interference. Spectrum-sharing systems are developed to improve spectral efficiency while controlling and canceling interference. The research integrates wireless technologies into BackComm, enhances system performance through advanced design, and develops optimization algorithms. By incorporating these advanced designs, this research seeks to significantly improve the performance and efficiency of BackComm systems, ensuring they meet the demands of passive IoT applications.

The specific contributions of this thesis are discussed next.

1.3 Thesis Contributions

This thesis aims to improve the BackComm performance by creating optimization algorithms and incorporating them with other cutting-edge technologies summarized as follows:

- **Developing optimization algorithms:** The primary goal is to maximize the sum rate of various BackComm configurations by optimizing system parameters, ensuring

the minimum required power for tags while meeting minimum QoS and interference thresholds. Convex and non-convex algorithmic solutions will be developed.

- **Integration with emerging technologies:** As they comprise passive tags, BackComm networks exhibit limited communication range, poor data rates, spectrum scarcity, and interference issues. This suggests addressing these challenges by using emerging wireless technologies such as IRS, MIMO, spectrum sharing, cooperative communications, and ISAC.

The following describes the contributions of this thesis:

1. When a single reader is employed to serve multiple tags, interference issues degrade the system performance. To tackle this challenge, Chapter 3 proposes MIMO and FD for the reader [24–26]. Leveraging spatial diversity with the MIMO reader, spatial domain multiple access (SDMA) is proposed to effectively separate signals from each tag, thus reducing inter-tag signal collision. However, for Monostatic BackComm, the reader must operate in the FD mode and employ precise beamforming techniques. This necessity arises due to two reasons. Firstly, the received power at the tag must exceed a threshold for reliable activation. Secondly, significant propagation delays can occur due to the round-trip communication from the reader to the tag and back to the reader. However, the main challenge of FD is SI. Although SI cancellation is possible, the FD reader remains susceptible to residual self-interference (RSI), which impacts the rate. In the thesis, innovative methods are devised to control this destructive interference. System parameters such as precoders, combiners, and tag reflection coefficients in a MIMO-FD Monostatic BackComm network with multiple tags are optimized. The optimization criterion is to maximize the system's sum rate while minimizing the impact of RSI, and considering energy constraints for tags as an additional optimization constraint.

2. In keeping with the second theme, spectrum-sharing systems offer a solution where BackComm acts as a secondary system, utilizing spectrum from a licensed primary network. An innovative spectrum-sharing solution is proposed in Chapter 4. In this

setup, a downlink NOMA system serves as the primary network, while the BackComm network utilizes this downlink signal for its data transmission. An IRS-enabled backscatter design with dual functions is introduced to enhance the BackComm link. The IRS assists the primary system in relaying its data and also reflects its own data by modulating over the downlink signal. To mitigate interference from IRS data, the primary transmitter adopts power splitting to transmit two spectrally distinct signals, enhancing signal detection at the receivers. The investigation focuses on rate maximization for this proposed system design.

3. Chapter 5 proposes SR BackComm with cooperative communication for the following reasons. In BackComm, the main problem is the weakened backscatter link due to the tag's dyadic channel and passive characteristics. Our insight suggests that coexistence for spectrum-sharing and collaboration with other cellular nodes, such as user equipment (UE), could effectively address this challenge. Thus, Chapter 5 delves deeply into the design of Backcomm systems involving spectrum sharing with cooperative cellular nodes, like UEs. This system design utilizes two phases of uplink transmission. The initial phase involves a conventional SR phase where the assigned BD uses the uplink UE signal to backscatter its data. The cooperative aspect is introduced in the second phase, wherein the UE decodes the particular BD's signal, allocates a portion of its power to embed it into its message, and transmits it to a common receiver (e.g., BS). The sum throughput maximization problem is the main focus.

4. Chapter 6, to further explore the BackComm network coexistence and spectrum sharing, merges an ISAC system and SR. The system features multiple users, a BS, a target, a sensor, and a IRS. The full duplex BS transmits data in the downlink and performs target sensing in the uplink. The IRS is optimized to enhance the downlink sum rate and modulates and reflects the sensor data by backscattering alongside the joint communication and sensing signals. The primary objective is to maximize the sum rate while ensuring a minimum signal-to-noise ratio (SNR) requirement for both the IRS data and target sensing.

Overall, this thesis contributes to the field of BackComm by developing optimization algo-

rithms and integrating them with emerging wireless technologies. The thesis proposes convex and non-convex optimization algorithms to maximize the BackComm data rates while considering the power requirement of the tags and meeting QoS and interference thresholds. It develops algorithms integrating BackComm with IRS, MIMO, spectrum sharing, cooperative communications, and ISAC. These algorithms address limitations like limited communication range, poor data rates, and interference issues. Specific solutions include using MIMO and FD technologies to mitigate inter-tag interference, employing IRS for spectrum sharing and backscatter link enhancement, and implementing cooperative communication to maximize throughput. These innovations aim to improve BackComm network performance, efficiency, and integration, advancing the capabilities and applications of passive IoT devices in various network scenarios.

1.4 Organization of Thesis

The remainder of the thesis is structured as follows. Chapter 2 surveys backscatter communication principles and conducts a literature review on integrating BackComm with other technologies, including MIMO, FD, IRS, and SR. Following that, Chapter 3 investigates the MIMO monostatic BackComm with FD reader considering the RSI at the FD reader. Then, Chapter 4 proposes IRS-enabled backscattering in a downlink NOMA system. Subsequently, to manage interference in the BackComm, a cooperative symbiotic radio backscatter system is proposed in Chapter 5. In Chapter 6, IRS-empowered backscatter in ISAC system is studied. In conclusion, Chapter 7 summarizes the research presented in this thesis and suggests potential avenues for further research.

Chapter 2

BackComm Integration With MIMO, FD, IRS, And ISAC

This chapter reviews the fundamentals of BackComm and its integration with MIMO, FD, SR, IRS, and ISAC. The chapter is divided into two sections. The first explores the core concepts of BackComm, covering basic configurations, tag details, channel modeling, and the reader. The second focuses on how BackComm can be integrated with other technologies.

2.1 Background of BackComm

A fundamental BackComm setup comprises three key components: a BD (tag), an RF emitter, and a backscatter receiver (reader), see Figure 2.1. The subsequent sections will discuss each component in detail.

2.1.1 Tag's general features

Traditionally, tags have been used in radio frequency identification (RFID) technology, which utilizes RF waves for automatic object identification and tracking. RFID tags are simple devices composed of a microchip and an antenna. They operate passively, relying on EH instead of a battery. As a result, they do not require power-intensive components like oscillators, analog-to-digital converters, or amplifiers. Consequently, they cannot generate

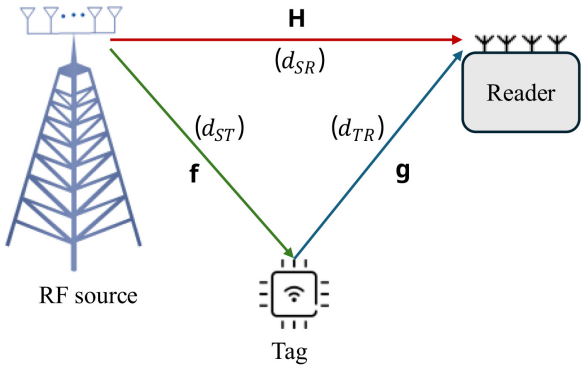

Figure 2.1: Ambient BackComm system.

Table 2.1: Comparison of Conventional and Next BackComm Systems

Name:	Coverage	Rate	Energy source
conventional RFID	<1 m	<640 Kbps	Dedicated
New BackComm	<3km	<10 Mbps	Dedicated and ambient

an RF signal to initiate data transmission. When tags come into the range of an RFID reader, the reader emits radio waves that power up the tag and read its data. Typically, the minimum RF energy level required to activate a commercial passive RFID tag and enable it to transmit its stored data to the reader is around -20 dBm. However, commercial RFID readers have limited coverage, usually less than 1 meter, necessitating dense deployment of readers [27]. The emerging passive BackComm technology addresses this limitation by leveraging dedicated and ambient energy sources. Table 2.1 provides a summary and comparison of key properties between conventional RFID and the next-generation BackComm [27]. Modulation and EH units are crucial in every tag, as described below.

2.1.2 Tag modulation unit

Modulation is the process of mapping digital data to RF signals for data communication. As previously mentioned, a tag cannot generate RF signals independently. Instead, it relies on passive backscatter modulation, also known as load modulation. This is accomplished by the tag adjusting the load impedance presented to the RF antenna based on the data. For example, Fig. 2.2 illustrates the modulation block of a tag, where the load impedance presented to the antenna is selected. The mismatch between the load and antenna impedance values generates a reflection coefficient, whose phase and/or amplitude can represent data

points. This forms the basis of load modulation.

If the tag uses an M-ary modulation format, its reflection coefficients can be expressed as

$$\Gamma_i = \begin{cases} \frac{Z_i - Z_a^\star}{Z_i + Z_a^\star} = \sqrt{\alpha_i} e^{j\phi_i}, & i = 1, \dots M \\ 0, & i = 0 \end{cases} \tag{2.1}$$

where $0 < \alpha_i \leq 1$ is the tag fraction power reflection and $e^{j\phi_i} = q_i$ is the tag's normalized reflected symbol (e.i. $|q_i|^2 \leq 1$) selected from M-ary modulation. Also, Z_a denotes antenna impedance, and Z_i denotes the load impedance of state i. When the antenna impedance matches the load impedance (e.g., $Z_a^\star = Z_0$), the tag absorbs the signal completely, so the reflection coefficient is zero. Otherwise, the tag operates in the reflection mode with varying reflected power levels. The tag can harvest and reflect simultaneously by utilizing a portion of the received power for EH and the remaining power for modulation which is pertinent to power-splitting EH mode. This process is further discussed in Sections 2.1.3 and 3.2.

Generally, the tag may perform three basic modulation schemes, including amplitude-shift keying (ASK), phase-shift keying (PSK), and frequency-shift keying (FSK) pertinent to changing the amplitude, phase, and frequency of the received RF signal, respectively [10, 14, 28, 29].

- ASK is an amplitude modulation that conveys the binary data by changing the amplitude level of the RF signal. The on-off keying (OOK) is the simplest form of ASK. However, it is more prone to be affected by noise. The reader can detect the ASK signal employing both coherent and noncoherent detectors [28].

- PSK is a type of modulation that transfers binary bits by varying the phase of the incident RF signal [10]. For example, Figure. 3.2 shows the QPSK backscatter modulator for a tag. The power reflection coefficient (e.g., $\alpha_i = \alpha$) is 0.8 for all four modulation symbols, while the phase can be selected based on the tag's information bits. Although the PSK modulation is less vulnerable to error than ASK, it requires a coherent demodulator, making the detection process more complicated [10].

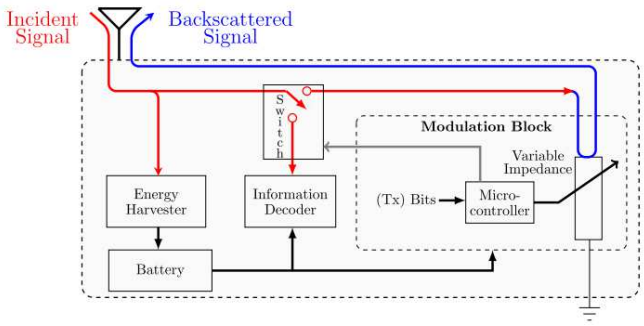

Figure 2.2: Tag circuit diagram [27].

- FSK is a type of frequency modulation in which the RF signal's frequency is shifted between two frequencies f_1 and f_2 in response to changes in the digital signal, or bits 1 and 0. As a result of its resistance to noise and changes in signal intensity, FSK modulation is frequently utilized in BackComm systems. However, it requires more spectrum compared to other modulation schemes. Coherent and noncoherent detectors can both be used to recover FSK signals [29].

2.1.3 Energy harvesting operation of the tag

Tags, acting as low-power nodes, are equipped with EH capabilities, enabling continuous sensing, data transfer, and energy-efficient communication. For instance, in a smart home scenario, numerous backscatter sensors with EH devices and rechargeable batteries are strategically placed throughout the house [30]. These self-sufficient nodes eliminate the need for external battery charging or replacement. They perform various tasks, such as gas leak detection, power management, motion detection, surveillance, and more [31, 32].

As a result, there are several benefits of using EH in BackComm networks.

- Renewable energy harvesting, like solar or wind power and ambient RF sources, enhances the sustainability of IoT networks, reducing their environmental footprint [31].

- EH ensures a continuous power supply for tags, enhancing their reliability and minimizing downtime [13].

- EH eliminates the expenses associated with battery replacements and grid connections, resulting in long-term cost savings [13].

RF energy harvesting offers numerous advantages in various areas and applications, providing simultaneous energy delivery to multiple nodes while ensuring dependability, predictability, and controllability. For instance, a cellular global system for mobile communications (GSM) base station generates 0.1 $\mu W/cm^2$ of RF energy. In turn, the EH unit of a tag should output power within the range of 1μW-100μW to meet its power requirements [33,34].

The EH unit functions in two modes: (i) Time-splitting (TS) and (ii) Power-splitting (PS).

- Time-splitting: In this mode, the EH and reflection processes occur in separate time slots. During the time slots allocated for EH, the tag adjusts its antenna impedance to match the load impedance, allowing the EH module to absorb the incident RF signal completely. Consequently, the tag utilizes an energy storage or battery to store the harvested power for subsequent reflection. During the time slots allocated for data communications, the tag will reflect the incident RF signal according to Section 2.1.2.

- Power-splitting: with this, the EH and reflection occur simultaneously [35]. Suppose the reflection coefficients of all tag load impedance values have a constant magnitude, i.e., $|\Gamma_i|^2 = \alpha_i = \alpha$. Therefore, the received power at the tag antenna, P_r, is split, and αP_r is used for reflection, and the remaining $(1-\alpha)P_r$ for EH [35].

In addition, to model an EH circuit and quantify the amount of harvested power, the linear model is often assumed due to its tractability. For the linear model, the harvested DC power is a linear function of the input power, defined as

$$P_h = \eta \alpha P_r, \tag{2.2}$$

where $\eta \in (0, 1]$ is the power conversion efficiency and P_r is the received power at the node. In particular, η varies according to the different EH technologies. For instance, photovoltaic and piezoelectric circuits can achieve up to 40% and 30% efficiency, respectively [36]. However, in practice, the EH circuit has components with non-linear characteristics (e.g., rectifier or capacitor). Thus, the output power is a nonlinear function of the input power, including a saturation plateau for large input powers and zero output for input power

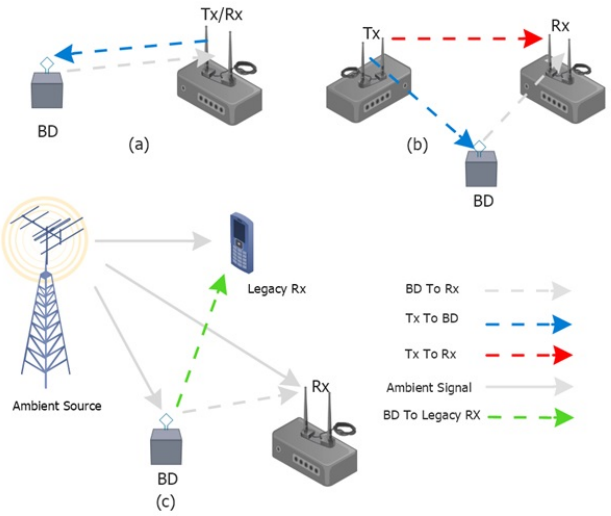

Figure 2.3: BackComm systems: (a) monostatic, (b) bistatic, (c) ambient .

less than the sensitivity threshold (e.g., -20 dBm for commercially available passive RFID tags [37]) [38]. The nonlinear models, such as sigmoid [39], piecewise functions [40], and a nonlinear model based on error function [38], are thus developed to quantify the harvested DC power. For example, the piecewise nonlinear EH can be modeled as

$$P_h = \begin{cases} 0, & P_r \leq P_{\text{sen}}, \\ \eta \left(P_r - P_{\text{sen}} \right), & P_r \in [P_{\text{sen}}, P_{\text{sat}}], \\ \eta \left(P_{\text{sat}} - P_{\text{sen}} \right), & P_r \geq P_{\text{sat}} \end{cases} \tag{2.3}$$

where P_{sen} and P_{sat} denote sensitivity and saturation power, respectively. This model captures the sensitivity and saturation effect of practical EH circuits. Also, it assumes a linear response up to the saturation level.

2.2 RF emitter

Depending on the type of RF emitter, the three configurations are Monostatic BackComm, bistatic backscatter communication (Bistatic BackComm), and Ambient BackComm, as shown in Figure 2.3.

- Monostatic BackComm: It is characterized by the reader, who is also the source of the RF signal to excite tags to modulate their data [41] (Fig. 2.3. (a)). Basically, the reader acts both the external RF source and the data sink for the tags. Thus, it transmits an RF signal for tags to reflect and/or absorb for EH purposes. Thus, the signal must travel from the reader to the tag and back. So, the deeper fading arises because of the colocated RF and a reader device. This doubly near-far dilemma may also have a significant impact on Monostatic BackComm performance. Subsequently, signal loss at the tag and the reader results in a lower modulated backscatter signal strength and a larger energy-outage probability when the reader and the backscatter transmitter, or tag, are placed far apart. Consequently, this mode is appropriate for short-range RFID applications.

- Bistatic BackComm: A dedicated baseband RF emitter sends an RF signal to the tags to backscatter their data [42] (Figure 2.3. (b)). In contrast to Monostatic BackComm, the round-trip path-loss can be eliminated in this configuration. Besides, multiple carrier emitters can be placed around the tags. Therefore, the communication range can be expanded. The tag can also draw power from multiple RF signals, reducing the energy outage probability. As a result, this configuration has been studied before [12]. Consequently, signal waveforms can be optimized to achieve a tradeoff between the amount of energy harvested at the tags and the reliability of the communication [43].

- Ambient BackComm: This is similar to Bistatic BackComm with the difference that instead of a dedicated RF emitter, tags leverage ambient signals such as TV, WiFi, cellular RF, and others (Figure 2.3. (c)) [44]. Using nearby ambient RF sources eliminates the need to deploy and manage dedicated RF sources. As a result, Ambient BackComm costs and energy usage can be decreased. On the other hand, although tags can use ambient signals opportunistically, such RF sources are unpredictable and uncontrollable. In addition, since the BackComm uses unlicensed signals, the interference from the BackComm network on legacy receivers should not degrade the performance of the licensed network.

More specifically, many of the properties of the RF signal emitter, as determined by

either the reader, power beacon, or ambient source as an RF emitter, are in accordance with local regulations. For example, RFID systems use carriers around $860 - 960$ MHz, and the equivalent isotropic radiated power (EIRP) at the reader is compliant with local regulations. In another example, in Ambient BackComm setup, the tags can use signals in very high frequency (VHF) (30 MHz to 300 MHz) band such as FM base station signal and ultra high frequency (UHF) (300 MHz to 3 GHz) band like TV tower signal. In particular, These RF sources can transmit up to 1MW for the TV tower and up to 100KW for the FM base station [45]. As a result, the distance between the tag and the RF source can range several kilometers. Furthermore, ambient Wi-Fi 2.4 GHz signal works with a radiated power of 100 mW, and Wi-Fi 5 GHz allows a maximum of 1000 mW EIRP. Subsequently, the RF source signal can reach and support those tags located within several meters of Wi-Fi.

2.3 Backscatter receiver (Reader)

The reader is a standalone node (apart from the RF emitter) in all configurations except Monostatic BackComm, paired with an RF emitter. In fact, reader characteristics such as receiver sensitivity, reader antenna gain, and the number of antennas directly impact the reliability of BackComm communication. For example, at a sensitivity of -60 dBm, an incoming signal of -65 dBm cannot be detected [7].

Many detection schemes for the reader have been proposed to extract data from tag signals. Noncoherent detection is one of the most popular schemes [46]. The complexity of the backscatter receiver circuit is particularly reduced because the noncoherent detection does not require estimating the carrier phase. However, coherent detection can be used to increase the bitrate compared to noncoherent detection. Coherent detection differs from noncoherent detection because it necessitates understanding the carrier phase, making the backscatter receiver circuit more challenging. Many existing works assume that ambient RF signals in Ambient BackComm systems follow zero-mean circularly symmetric complex Gaussian distributions because the ambient RF signals are uncertain or even unknown at the backscatter receiver. Therefore, maximum-likelihood (ML) detectors can then be used to find the modulated signals at the reader [47]. Nevertheless, other factors, such as multi-

antenna at the reader, can affect the detection performance of backscattered links at the reader.

Also, the multi-antenna readers can benefit from multiplexing gain and a higher spatial degree of freedom. Hence, studies show the gain of the multi-antenna readers over single antenna ones [41, 48].

2.3.1 Data Detection at the Reader

In BackComm systems, the reader must detect signals to decode the tag's data. However, signal detection in BackComm is more challenging than in conventional communication systems. There are two reasons. Firstly, the tag's signal is weak because the dyadic channel increases fading. This weak signal can be overshadowed by strong interference from ambient sources in Ambient BackComm or carrier emitters in batteryless BackComm systems. As a result, traditional signal detection methods may not be applicable in BackComm. Depending on the reader's capabilities, detection techniques can be classified into coherent and non-coherent detection [14].

Coherent detection

This method necessitates precise knowledge of the receiver's channel state information (CSI) and the carrier phase. When it comes to error probability, coherent detectors are optimal. Among coherent methods, the ML detector is an optimal algorithm [49]. However, other techniques like the asymptotically optimal generalized likelihood ratio test (GLRT) can be used as it maximizes the rate of decay of the probability [50].

Non-Coherent detection

Non-coherent detection does not necessitate knowledge of the carrier phase and CSI. While this requirement reduction leads to decreased receiver complexity, it comes at the cost of lower spectral efficiency or a potential performance penalty.

When it comes to BackComm, the envelope detector, which is a non-coherent detection based on the average energy of the received signal, is simple with a low complexity method

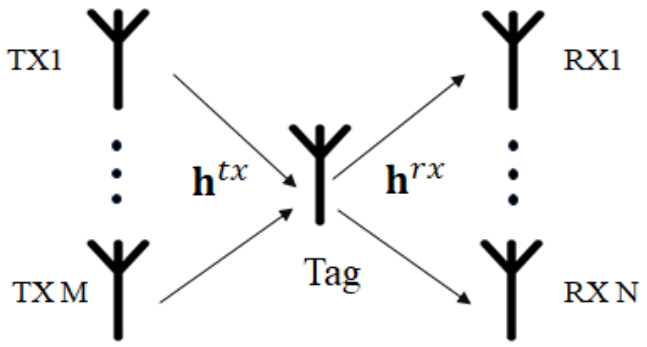

Figure 2.4: The (M,1,N) dyadic backscatter channel.

[51], [52].

2.4 BackComm Channel

Backscatter channels (Figure 2.4) exhibit atypical fading characteristics. To illustrate them, consider a simple example. Let $\mathbf{h}^{tx} \in \mathcal{C}^{M\times 1}$ and $\mathbf{h}^{rx} \in \mathcal{C}^{N\times 1}$ represent the channels between the RF source and the tag, and between the tag and the reader, respectively, where M is the number of transmit antennas at the RF emitter, and N is the number of receive antennas at the reader. The channel coefficient the reader observes is the fundamental quantity determining the capacity and communication range.

In this scenario, the tag antenna acts as a "pinhole" during the forward link (i.e., RF source to tag) [53], consolidating all multipath components at a single physical point. The tag then rescatters the combined signal to the receive antennas. As a result, the backscatter channel can be described by the tuple $(M, 1, N)$, and the effective channel is the product of the forward and backward (i.e., tag-to-reader) channels, represented as $\mathbf{h}^{rx}(\mathbf{h}^{\mathbf{tx}})^H$, known as a dyadic channel.

This dyadic effect reduces the channel capacity. Moreover, the dyadic backscatter channel results in deeper fades, i.e., a higher probability of severe fades than conventional links. This occurs because the dyadic channel is the product of two fading variables.

To gain better insight, Figure 2.5 illustrates the envelope probability density function (PDF) of the single-antenna BackComm with Rayleigh channel compared to the PDF of a conventional channel. Clearly, the dyadic channel suffers from deeper fading, leading to

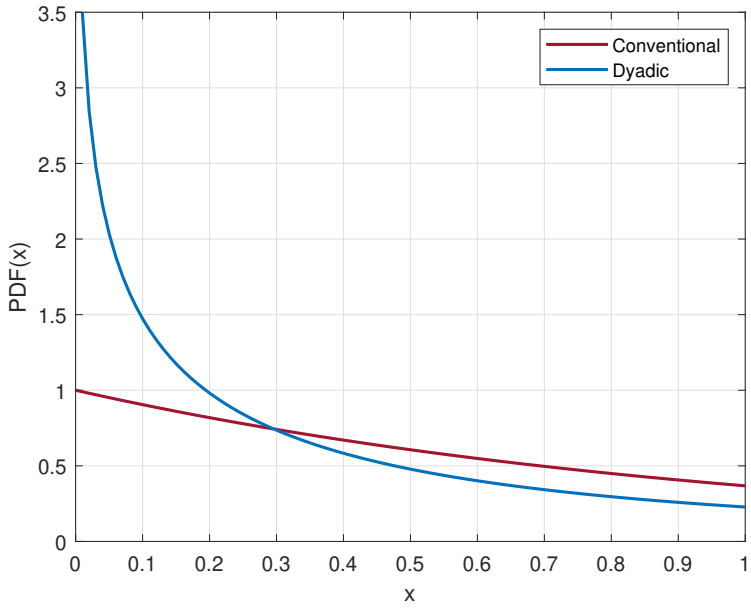

Figure 2.5: A comparison of dyadic PDF and conventional channel PDF for Rayleigh channel.

more frequent outages. Furthermore, path loss (i.e., large-scale fading) is additive in these channels. Consequently, these impairments fundamentally affect the tags' data rate and communication range.

2.5 BackComm Integrated with Other Technologies

The following section explores the benefits and potential synergies of integrating BackComm with other advanced technologies, highlighting how these combinations can enhance overall system performance, improve efficiency, and enable new applications.

2.5.1 Integration of BackComm with MIMO

MIMO technology offers numerous advantages compared to its single-input single-output (SISO) counterpart. Multiple antennas enhance diversity, particularly in slow-fading conditions, while providing advantages of power and degrees of freedom in fast-fading scenarios [54]. Hence, the integration of MIMO with BackComm can be employed to harness its potential. Consider, for instance, the MIMO RFID system, whose fading characteristics di-

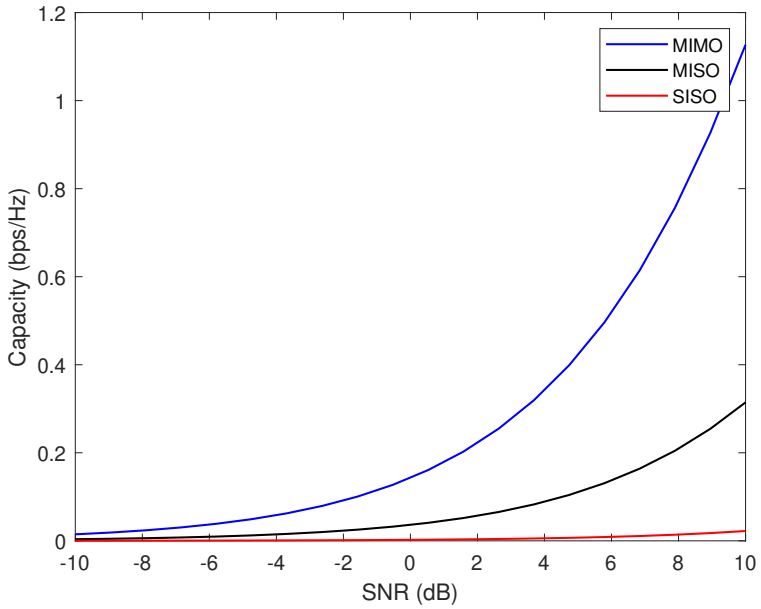

Figure 2.6: Capacity comparison of MIMO(4×4), MISO (4×1) and SISO (1×1) BackComm with 5m tag-reader distance.

verge from traditional MIMO links relying on far-field propagating modes. The distinctive feature of the BackComm channel, in contrast to the conventional M transmit N receive antenna Rayleigh MIMO channel, lies in the dyadic backscatter channel (see Section 2.4).

Figure 2.4 depicts the dyadic channel between M-transmit antennas and N-receive antenna in a single-tag scenario. Figure 2.6 illustrates the achieved capacity for three different antenna configurations of tag-reader pair. For instance, 4×4, 4×1, and 1×1 are for MIMO, multiple-input single-output (MISO), and SISO, respectively. The performance gap between MIMO and the other two widens in high SNR conditions. This highlights the superiority of MIMO in achieving capacity within the BackComm framework.

Furthermore, to address the reliability and security of RFID systems, [55] propose noise-injection precoding in a MIMO Monostatic BackComm network. The objective is to maximize the secrecy rate by optimizing the energy power and the precoding matrix of the injected artificial noise at the reader. Besides, resource allocation in a MIMO backscatter-assisted wireless-powered Communication Network is proposed in [56]. Users are assumed to work in either a wireless-powered communication network or backscatter mode. The aim is to maximize the sum throughput of this system over time allocation, mode selection, and

precoder matrix while considering finite alphabet inputs. Considering multi-tag in MIMO reader Monostatic BackComm in [57], the authors first propose the least-squares-based channel estimation and then use the estimated channel to optimize the transceiver design to maximize the minimum backscatter throughput of among all tags. Similarly, [26] considers multi-tag Monostatic BackComm; however, the reader is a massive MIMO reader. Four different transceiver configurations are proposed. The study demonstrates that the overall transmit power can be proportionally reduced by the square of the transmit antennas, with no compromise in performance.

Thus, integrating MIMO with BackComm yields performance gains. These include improving communication link reliability, bit-error-rate reduction, and capacity gains [25, 26], [55–57]. Although many Backcomm studies exploit the diversity and multiplexing gain introduced by MIMO, more research questions remain. For instance, Ambient BackComm or Bistatic BackComm can be analyzed with multiple-antenna tags. The tag's design must be simple to fulfill the low-power and low-cost requirements, often constrained to a single antenna. Nevertheless, tags with more than one antenna can significantly enhance data rates.

2.5.2 Integration of BackComm with FD

In contrast to its half-duplex (HD) counterpart, FD communication enables simultaneous transmission and reception on a single channel [58]. This capability has the potential to enhance spectral efficiency twofold, distinguishing it from HD alternatives that can only transmit in a single direction at any given time. Several studies have introduced FD into BackComm [18, 59–62]

In [59], the FD multiple mobile users transmit data to a common access point (AP) while simultaneously receiving the signal from their associated BD. The interference from multi-users is avoided at the AP according to the carrier sense multiple access. The PHY-layer outage probabilities are derived, and cross-layer outage capacities for both systems are examined. The incorporation of FD in the information transfer BackComm system is presented in [60] to minimize latency and enhance spectrum utilization efficiency. Nevertheless, this FD system leads to an exacerbation of interference links. Time-hopping full-duplex

Table 2.2: Summary of MIMO BackComm optimization problems

#	System Model	Design Obj.	Opt. Method	Main Finding(s)
[26]	Massive MIMO-Monostatic BackComm	Precoder and combiner design	ZF, MF, opt. backscatter coefficient	Best performance of MF-ZF in terms of spectral and energy efficiency
[55]	MIMO-Monostatic BackComm with noise injection	Max. secrecy rate	AO, sequential parametric CA	Better secrecy rate among other baselines
[56]	MIMO-FD Monostatic BackComm WPCN	Max. sum throughput	AO, gradient-based strategy, ADMM	Better performance of Backscatter WPCN compare to WPCN
[57]	CE and fairness MIMO monostatic BackComm	Max. minimum backscattered throughput	Least-square, eigenvalue decomposition	Over seven-fold increase in tag backscatter throughput

* ZF: Zero forcing, MF: Match filter, AO: Alternative optimization, CA: Convex approximation, ADMM: Alternating direction method of multipliers.

multiple access is proposed based on interference suppression by spread spectrum to avoid interference. In another example, in [61], the FD access point transmits OFMA signal to a legacy user while receiving signal from multi-BDs in a time-division multiple access (TDMA) manner. The numerical results demonstrate the superior throughput of the FD system compared to the HD AP. Similarly, in [18], an underlay cognitive BackComm system is proposed where FD AP transmits a primary signal to primary users while receiving a signal from BD in the uplink via TDMA manner. The uplink transmission of BDs is structured to ensure that any resulting interference does not compromise the quality of the primary transmission. The aim is to maximize the throughput while satisfying network requirements.

Monostatic BackComm with FD communications has been studied in [63], [24], [64], [26], and [41].

2.5.3 Integration of BackComm with Symbiotic Radio (SR)

The widespread deployment of IoT devices will bring about an upsurge in energy-efficient communication and radio spectrum utilization. SR serves as a transformative solution that

Table 2.3: Summary of SR BackComm optimization problem

#	System Model	Design Obj.	Opt. Method	Main Finding(s)
[65]	MIMO-SR backscatter	Sum capacity max.	Penalty-based algorithm	Reaching sum capacity close to capacity upper bound
[66]	MIMO-SR massive BD	Rate analysis and precoding opt.	MMSE, SVD	SR mutualism is fully exploited with massive BD
[23]	FD SR multi-BD NOMA dynamic-TDMA system	Minimum throughput max. among BD	BCD, SCO	Proposed design outperforms dynamic-TDMA
[67]	SR with multi-antenna transmitter	Weighted sum-rate max. and PT min.	SDR	Primary rate is improved using BD
[68]	MIMO-SR with IRS-backscattering	PT Min.	AO, SDR	Benefits of the IRS-assisted MIMO-SR system

* MMSE: Minimum mean square error, SVD: Singular value decomposition, BCD: Block coordinate decent, SCO: Successive convex optimization, PT: Power transmit, SDR: Semi-definite relaxation.

enables radio systems to share resources by establishing symbiotic relationships collaboratively [67, 69]. Such connections can either be mutualistic, where both parties benefit from the interaction, or parasitic, wherein one party gains advantages at the expense of the other. This innovative approach underscores the dynamic nature of radio broadcasting, emphasizing the potential for interdependence and cooperation among different entities within the radio ecosystem. Therefore, symbiotic radio refers to the coexistence of two radios with a symbiotic relationship to share a radio system [69]. Unlike cognitive radio (CR), which is defined because not all of the radio spectrum is occupied all the time, and white spaces/spectrum holes can be utilized by the secondary users, in SR, the secondary depends on the spectrum of the primary network for its transmission. Their relation can be parasitic (e.g., when two systems in an association share radio resources, one system profits while the other suffers) or commensal (e.g., one system benefits by sharing the radio resources, but the other gets no benefit or harm).

A good example of an SR system is where the secondary system is a low-power system like BackComm, where BD cannot generate any RF signal and depends on the signal from the

primary system's coexistence. The main difference between the SR and Ambient BackComm is that the primary receiver can benefit from the extra propagation link from BD reflection in commensal SR. In the following, we review the recent works that propose system optimization in SR backscatter.

A MIMO SR BackComm system with the cooperative receiver (e.g., the primary receiver and BD receiver are integrated) is proposed in [65]. All nodes are multi-antenna, aiming to maximize the sum capacity of the primary system and backscatter by optimizing the transmit beamforming. The results demonstrate that the achieved optimal sum capacity is close to the capacity upper bound using the penalty-based algorithm. The MIMO SR with massive BD is studied in [66] where after deriving the achievable rate of both primary and backscatter rate, the precoding optimization problem is studied to maximize the primary communication rate while guaranteeing a minimum rate for the secondary system. An FD-SR in a NOMA dynamic-TDMA with multi-BD is investigated in [23] where an FD-AP transmit an orthogonal frequency division multiplexing signal to a legacy user while receiving signal form BDs. The goal is to maximize the minimum throughput among BDs while satisfying other systems' requirements, such as legacy user throughput, EH at BDs, and other constraints. The results emphasize the better performance of NOMA dynamic-TDMA over dynamic-TDMA for both legacy users and BD. In a similar vein, considering the basic SR BackComm system, authors in [67] derive the achievable rates and solve two problems: (1): weighted sum-rate maximization and (2): transmit power minimization over transmit beamforming. Furthermore, the utilization of IRS as a BD is presented in a MIMO-SR system in the study by Zhang et al. [68]. In this model, the IRS functions as a secondary transmitter. It not only improves the link of the primary system but also utilizes the signal from the primary transmitter to modulate its data, reflecting it to the secondary receiver. Throughout this investigation, the objective is to minimize the transmit power at the primary receiver while ensuring a quality of service for each system.

The SR technique developed recently aims to harness the benefits of both CR and Ambient BackComm, effectively addressing the shortcomings associated with these two technologies [70]. SR can leverage the spectrum sharing between primary and secondary systems. However, it can attain mutual spectrum-sharing benefits rather than interfere with spectrum-

sharing in CR. The main advantage of SR over Ambient BackComm is the joint decoding of both system messages, which makes the BackComm more reliable.

2.5.4 Integration of BackComm with IRS

To pave the way for the development of intelligent and adaptable wireless channels and radio propagation environments in the next era of mobile communication, groundbreaking technologies such as IRS have recently emerged [71]. An IRS, a two-dimensional planar structure, comprises many passive reflecting elements, each capable of dynamically adjusting the incident signal phase and/or amplitude. This dynamic adjustment enhances communication links, addressing channel fading and interference challenges.

The reflecting elements constituting an IRS are constructed using low-cost and low-power printed dipoles. These dipoles have the unique ability to modify the properties of impinging signals without the need for an elaborate RF chain [72]. In addition, the IRS works in FD mode without introducing any SI; therefore, it can compete with its counterparts, e.g., HD and FD relay, which has low-spectral efficiency in HD case and need sophisticated techniques to suppress SI, in FD mode. As a result, by harnessing this innovative technology, it becomes possible to create highly efficient and responsive wireless communication systems, ushering in a new era of connectivity where adaptability and intelligence are key features.

As a result, the IRS can also help the BackComm network overcome its inadequacies. IRS is used in BackComm in two separate ways in existing research: (1) IRS-assisted BackComm and (2) IRS-backscattering itself as a tag that is described as follows.

IRS-assisted BackComm:

Within this category, the IRS is seamlessly integrated into the BackComm as an independent node, significantly enhancing its overall performance. For example, in [73], the IRS is proposed to a NOMA BackComm system as an auxiliary link to enhance the backscatter link. The objective is to optimize the overall sum rate of this system by considering power reflections at backscatter devices and the phase shift introduced by the IRS. The findings reveal superior performance compared to a system lacking the integration of an IRS. In the

Table 2.4: Summary of IRS BackComm optimization problem

#	System Model		Design Obj.	Opt. Method	Main Findings
[73]	IRS-assisted	IRS-assisted NOMA backscatter	Sum rate max.	AO, SCA, manifold opt.	It outperforms NOMA BackComm without IRS
[74]		Backscatter-assisted WPCN using TDMA	Total throughput max.	AO, SCA SDR, BCD	2-bit resolution IRS is enough to suffices near optimal performance
[75]	IRS-Backscattering	Multi-user MISO SR system	Weighted sum rate max.	AO, FP	IRSs transmission benefits PR
[76]		IRS-enabled joint backscattering and communication	MOOP opt. to user rate max. goodout of BackComm	AO, Gradient-Method	Number of reflecting elements, impact system performance
[77]		IRS-assisted MISO multiuser downlink SR	Primary system sum rate max. max. SER	SCA	Better performance compared to different benchmarks
[78]		Multi-cell uplink transmission with IRS	Weighted sum rate max. problem	AO, FP	Number of reflecting elements impact performance

* SCA: Successive convex approximation, MOOP: Multi-objective optimization, SER: Symbol error rate, FP: Fractional programming, PR: Primary receiver

study by [74], multi-energy-constraint users operate in two transmission modes: backscatter and active transmission. These modes are supported by both a wireless-powered communication Network (WPCN) and the IRS, facilitating the transmission of their data to an AP in a TDMA fashion. The sum-throughput maximization problem is studied to optimize IRS reflection coefficients, time and power allocation, transmit beamforming at the power station, and receive beamforming at the AP. Furthermore, the application of IRS in a multi-tag Bistatic BackComm is considered in [79], where the tags implement frequency-shift-keying to avoid inter-tag interference at the receiver. They try to minimize the power of the carrier emitter while optimizing the IRS phase shifts. In addition, as illustrated in [80] and [81], the IRS acts as a transmitter of all received signals and multicast confidential information via backscattering to users, respectively.

IRS-enabled backscattering:

In this category, it is assumed that the IRS has its own information to reflect. In this instance, backscattering can be considered an IRS technology use case or special case. As illustrated in [75], the IRS acts not only as an enhancement link for the primary network but also as a backscatter device to enable backscatter transmission in a multi-user MISO SR system. The goal is to maximize the weighted sum rate of both the primary and BackComm systems. This optimization encompasses factors such as transmit beamforming at the primary transmitter and passive beamforming at the IRSs, accounting for scenarios involving ideal, continuous phase, and discrete-phase considerations. Similarly, the IRS in work [76] adjusts its phase shifts to convey its data as a backscatter device to a base station (BS) while helping the user's data in the primary network. The aim is to maximize the user average transmission rate of the primary communication and the good output of the BackComm by solving the formulated multi-objective optimization problem (MOOP). Similarly, IRS in [77] uses the primary network signal to modulate and reflect its data toward the secondary receiver while conveying the primary network information since the direct link between the primary transmitter and the primary receiver cannot be established. Subsequently, they jointly optimize the beamformer at the AP and the phase shifts at the IRS to maximize the average sum rate of primary networks while maximum tolerable symbol error rate constraint for the secondary network. Moreover, in the work by Xu et al. [78], an uplink transmission scheme is introduced for a multi-cell system. This approach involves empowering IRSs through a dedicated power beacon, which subsequently modulates its connected users' information to the associated BS. The objective is to optimize the weighted sum rate by optimizing the active beamforming at the power beacon, passive beamforming at the IRSs, and the scheduling of uplink users.

The IRS can be utilized to facilitate passive communication technologies, such as BackComm. The integration can be leveraged in two different ways. First, the IRS can be deployed in BackComm as an FD-relay to amplify the tag's reflected signals. In this scenario, the transmit-diversity capabilities of the IRS improve Backcom performance. Even if the IRS is moderately small, it can significantly decrease the transmit power at the carrier

emitter in Bistatic BackComm [82]. The integration takes another form with IRS-enabling backscattering, where each element of the IRS functions as a backscatter device, reflecting its sensed data. Likewise, in this configuration, BackComm can harness transmit diversity through IRS-enabling backscattering [77].

2.5.5 Integration of ISAC and BackComm

In addition to communicating with BDs, the future BS will need to sense the environment for high-resolution applications and protect the system from attacks [83]. ISAC has been developed to perform sensing and communication simultaneously using a common waveform, the same frequency band, and hardware [84]. ISAC offers low cost, low power consumption, and compact size, making it ideal for applications requiring both communication and sensing services. Consequently, ISAC and BackComm systems are being explored.

Reference [83] proposes an integrated sensing and IRS BackComm system. The BS simultaneously detects signals from multiple IRS backscatter data and the echo signal from a target. The sum rate of all devices is maximized under the Cramér–Rao bound constraint for the target's direction of arrival estimation. Reference [85] considers ISAC for SR, where the shared receiver can locate the moving IRS-backscattering by estimating the direction of arrival. Reference [86] analyzes the achieved communication rate in integrated sensing and BackComm where a tag uses the BS downlink signal to backscatter the signal toward its recipient. Simultaneously, the BS can also use this signal to sense targets.

2.6 Conclusion

This chapter provides a concise introduction to the background necessary for the rest of the thesis. It covers the fundamentals of BackComm and reviews the integration of MIMO, FD, IRS, and ISAC technologies. Each of these technologies offers significant advantages: MIMO enhances communication link reliability and capacity; FD improves tag activation and data reception efficiency in multi-backscatter scenarios; IRS technology enables better signal manipulation and transmission diversity, enhancing backscattering capabilities in BackComm networks; and SR techniques optimize spectrum utilization and mutual sharing between

primary and secondary systems, boosting reliability through joint decoding. Additionally, integrating ISAC introduces precise sensing and communication capabilities, promising advancements in tracking and positioning within BackComm applications. Collectively, these integrations propel BackComm networks towards higher performance, efficiency, and broader applicability across various wireless communication scenarios.

Chapter 3

Sum Rate Maximization of MIMO Monostatic BackComm by Suppressing RSI

This chapter examines the multi-tag Monostatic BackComm system with a multi-antenna FD reader. However, the reader experiences SI levels much higher (e.g., 160 dB) than the desired signal. However, since SI cancellation is imperfect, residual SI (RSI) dramatically degrades system performance. This chapter thus optimizes the precoder and combiner at the reader and tag reflection coefficients to maximize the sum rate and suppress the RSI subject to the tag EH constraints. Because this problem is non-convex, alternating optimization (AO) along with successive convex approximation (SCA), semi-definite relaxation (SDR), and geometric programming (GP) are utilized to solve this problem.

3.1 Introduction

As outlined in Section 2.2, there are BackComm configurations: Monostatic BackComm, Bistatic BackComm, and Ambient BackComm. Of the three, Monostatic BackComms enable many IoT applications such as smart homes/cities, healthcare, wearables, and more [31], [27, 87]. This is primarily attributed to their cost efficiencies [48]. This Chapter focuses on the Monostatic BackComm networks.

Table 3.1: Summary of Related Works

Ref.	EH Const.	RSI Const.	Opt. Precoder and Combiner	Opt. Ref. Coeffi.	Obj. Function	Solution Approaches
[48]	X	X	✓	✓	Sum Rate	Fractional Programming, SDR
[91]	X	X	✓	✓	Max–Min Rate	SCA, LPF, AO Bisection Search,
[26]	X	X	-	✓	Sum Rate	Analytical Solution
[34]	✓	-	-	X	Max–Min Rate	SQP
Our work	✓	✓	✓	✓	Sum Rate	SDR, SCA, GP, AO

Specifically, tags can be categorized into the following different groups:

- **Passive:** These have no RF components, do not generate RF signals, and communicate by passive reflections. These are thus pure batteryless devices entirely powered by EH from an external source.

- **Semi-passive:** These have the same characteristics as above except for limited battery and energy storage capability. Consequently, these tags have increased weight and cost compared to the passive ones.

- **Active:** These are battery-powered devices with RF components and communicate by active transmissions. Consequently, they communicate over $300 - 700$ feet compared to that of semi-passive tags with about 100 feet range [88].

As passive and semi-passive tags have the most applications because of their low cost, low power consumption, and non-generation of radio noise [87], such tags are the focus of this research. Furthermore, EH can power passive tags and reduce recharging/replacement costs in semi-passive tags, improving energy efficiency [8, 89, 90].

The reader in the Monostatic BackComm network is both transmitting and receiving simultaneously. Such FD operation can double the spectral efficiency, reduce the latency, and enhance the communication range [92,93]. However, the cost of these benefits is SI. The SI in conventional wireless networks can be as high as 110 dB above the received signal [94]. However, this gap can be even more significant for the Monostatic BackComm networks for the following reasons. First, since the RF signal travels from the reader to the tag and back to the reader, it experiences double path loss. Second, passive backscatter modulation of the tag

results in further losses. Due to these factors, it is estimated that the reader sees a received RF signal with about 160 dB loss for a tag at 100 feet. This loss depends on transmit/receive antenna gain, polarization mismatch, and other parameters [95, Table 3]. Although analog and digital SI cancellation techniques can achieve 70 dB suppression [92, 93], factors such as the transceiver impairments [96], propagation channel impairments, and estimation errors negate the possibility of perfect cancellation.

Even if the reader adopts some of these SI cancellation techniques, there will be RSI, which must be considered in the complete system design. Hence, by considering the RSI, this work aims to develop the transceiver design for the reader of a multi-tag Monostatic BackComm network. The reader utilizes spatial degrees of freedom (e.g., multiple antennas) to suppress the effect of RSI while the tags perform EH.

3.1.1 Motivation and Contribution

Optimal transceiver designs to limit RSI power level while providing the required power of tags have not been studied before. The reason for this gap is that previous works assume that the SI is completely eliminated by the reader's analog/digital SI cancellation techniques [48, 91]. This Chapter of the thesis fills out this research gap by investigating the design of transceivers for a MIMO reader, which is subject to non-zero RSI. The network supports uplink transmissions of multiple tags randomly scattered in a square region, and the tags reflect the RF carrier to send their data to the reader. These transmissions occur simultaneously. The reader separates the data signals of different tags via spatial filtering. Our contributions are summarized as follows:

- Unlike previous works, this study considers a more realistic model where the reader's analog/digital SI cancellation processes are imperfect, resulting in non-negligible RSI. The level of RSI is represented by the coefficient $\beta > 0$. All previous works implicitly assume $\beta = 0$. An algorithmic approach is developed to limit the effect of RSI for the regime $\beta > 0$.

- The sum rate of the network is maximized by jointly optimizing the transmit (precoder) and receive (combiner) beamformers at the reader, as well as the reflection coefficients

of the tags, subject to the RSI constraint at the reader and the EH constraint at the tags. Existing works [26, 48, 91] do not consider these constraints. This study concurrently considers both the energy and RSI constraints, a novel aspect that has not been previously studied.

- The resulting optimization problem is non-convex due to variable entanglement. To address this, the AO paradigm (also known as block coordinate descent) is exploited. This approach splits the main problem into several easy-to-solve subproblems and iterates among them sequentially until convergence. The formulation divides the variables into three blocks: the precoder vector ($\mathbf{f}$), the combiner vectors ($\mathbf{g}_k, k = 1, \ldots, K$), and the tag reflection coefficients ($\alpha_k, k = 1, \ldots, K$), where K is the number of tags. First, $\mathbf{f}$ is optimized by applying the SCA and SDR techniques. Unlike [48], which applies Gaussian randomization to compute $\mathbf{f}$, it is proven that the SDR solution is indeed tight.

- In the second subproblem, the combiner vector for the k-th tag signal, $\mathbf{g}_k, k = 1, \ldots, K$, is designed based on the minimum mean-squared error (MMSE) filter and the generalized Rayleigh quotient form of the received signal-to-interference-plus-noise ratio (SINR).

- The third subproblem optimizes $\alpha_k, k = 1, \ldots, K$ for $\mathbf{f}$ and $\mathbf{g}_k$ from the previous steps. Previously, such problems have been attacked with linear programming feasibility (LPF) [91], which is based on a bisection search and has a slow rate of convergence. This work instead develops an algorithm based on the GP paradigm to find α_k.

- Extensive numerical and simulation results are provided to assess the proposed algorithm. Specifically, three comparative benchmarks are studied: (i) tags without EH requirement, (ii) no RSI suppression at the reader, and (iii) randomly selected α_k. These comparative benchmarks help evaluate the efficacy of the proposed designs. The numerical results demonstrate the performance gains of the proposed design compared to these benchmarks.

Although [26,48,91] investigate Monostatic BackComm network models, our contribution

differs in two fundamental ways. These papers omit the RSI presence at the reader and the possibility of EH at the tags. Our work incorporates both of these critical factors. Even though [91] considers the tags that perform EH, there are no minimum energy constraints. Table 3.1 compares and contrasts our work in several recent papers.

3.1.2 Related Works

A key problem of Monostatic BackComm is the dyadic path-loss, making reliable detection a serious challenge. Thus, symbol error rate (SER) and bit error rate have been analyzed in [24,97]. In [24], the authors study the achievable diversity gains with unitary and orthogonal designs. Furthermore, the authors in [97] develop block-level unitary query and modified orthogonal-like space-time codes. Their simulations validate the proposed coding designs compared to other baselines regarding BER and SER. The optimal transceiver design at the Monostatic BackComm reader and the optimal tag reflection coefficients have been studied in [26, 48, 91]. Specifically, [48] jointly optimizes the downlink energy beamforming, receive combining at the reader, and tag reflection coefficients. This work reduces the reflection coefficient optimization to a binary power control problem. In addition, it also analyzes the sub-optimal joint design for two extreme cases, i.e., high and low SNR regimes. Reference [91] maximizes the minimum rate of the tags to collect data with fairness while considering EH at tags. SDMA allows all tags to reflect simultaneously. The reader's performance can be optimized by exploiting the available spatial degrees of freedom (DoF). This can be done with well-known precoders and combiners, namely matched filter (MF) and zero-forcing (ZF). Accordingly, [26] derives the capacity lower bound for four different combinations of these transceiver configurations for a massive MIMO reader and discusses the impact of imperfect CSI. However, all these works assume that the reader achieves perfect SI cancellation.

EH in the BackComm networks is considered in [5, 34, 90, 98]. For example, [34] uses energy beamforming to improve energy transfer efficiency. The energy beamforming is designed to maximize the minimum rate of tags subject to the energy constraint. The reader uses maximum-ratio combining (MRC) and ZF receivers while using the estimated backscatter CSI. Authors in [5] propose an EH relay-assisted network and maximize the system throughput by jointly optimizing the beamforming, power splitting (PS) ratio, and other parameters.

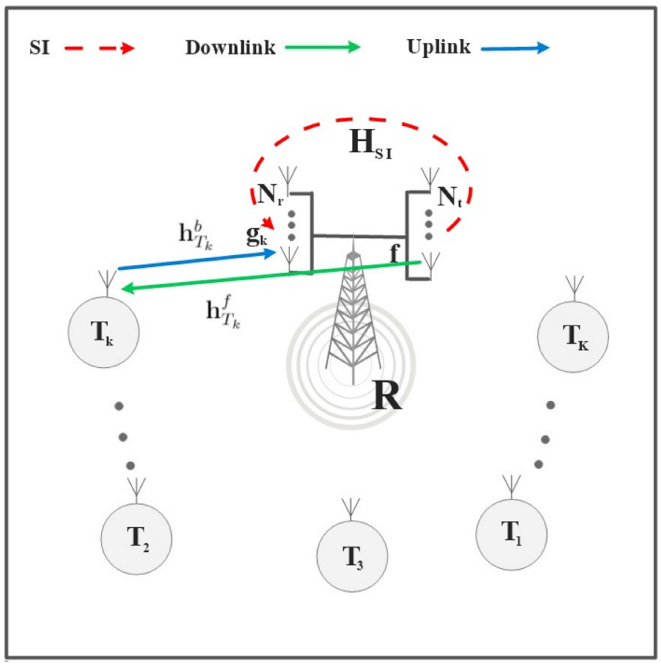

Figure 3.1: Monostatic BackComm network with reader ($\mathbf{R}$) and tags ($\mathbf{T_k}$, $k \in \mathcal{K}$).

Besides, [90] investigates hybrid nodes. Depending on ambient RF signals and the amount of harvested energy, the nodes select backscatter or active RF modes. Reference [98] studies the energy beamforming using the estimated backscatter CSI and derives optimal resource allocation to maximize the harvested energy at the receivers.

FD BackComm system is considered in [18, 60, 99]. In [60], authors study the BER, energy transfer efficiency, and outage probability. To mitigate interference, the authors also propose a time-hopping FD scheme. Reference [99] studies an Ambient BackComm system in which an FD-AP transmits an orthogonal frequency division multiplexing (OFDM) signal to the legacy user and BDs. The goal is to maximize the minimum throughput of all BDs by jointly optimizing the reflection coefficient, reflecting time, and subcarrier power allocation. Likewise, [18] considers resource allocation in an FD cognitive backscatter network where the AP transmits the primary signal and receives backscatter signals simultaneously.

3.2 System Model

Figure 3.1 shows an Monostatic BackComm network consisting of $K \geq 1$ single antenna tags indexed by $k \in \mathcal{K} = \{1, \ldots, K\}$, randomly distributed in a $r \times r$ square region [100]. The multiple antenna reader located at the center transmits an RF carrier in the downlink while receiving the backscattered signals via the uplink. Let us denote the k-th tag and the reader as $\mathbf{T_k}$ and $\mathbf{R}$, respectively. The reader is equipped with $N_t \geq 1$ and $N_r \geq 1$ transmit and receive antennas, respectively. Practically, current BackComm networks can only achieve low data rates and communication range in the order of 10 Kbps and a few meters, respectively [101]. However, this system leverages a multi-antenna reader to enhance the capacity, data rate, and communication range by exploiting spatial diversity gains. Consequently, this network may be applicable in various applications involving warehouses, wearables, biomedicals, and smart homes.

The following key/standard assumptions are made:

A1: Each tag uses load modulation, which depends on the complex reflection coefficient of the k-th tag, $\forall k \in \mathcal{K}$ [10]:

$$\Gamma_{i,k} = \frac{Z_i - Z_{a,k}^{\star}}{Z_i + Z_{a,k}} \tag{3.1}$$

where $Z_{a,k}$ denotes the antenna impedance of the k-th tag, and Z_i is the i-th load impedance $i \in \{1, 2, \ldots, M\}$. Although binary backscatter modulators have been widely investigated, they limit the data rate and are spectrally inefficient. Thus, higher-order modulation ($M > 2$) is considered by using more than two impedance values. Denote $\Gamma_{i,k} = |\Gamma_k| e^{j\theta_i}$ where $\theta_i \in [0, 2\pi]$. All the tags use the same set of phases $\{\theta_1, \theta_2, \ldots, \theta_M\}$ to convey their data, which amounts to a M-ary phase-shift keying (PSK) constellation. That is why $\angle\Gamma_{i,k}$ does not depend on a particular tag but reduces to θ_i. This is a reasonable assumption, as practical systems will employ identical tags. The load impedances required to generate it can be computed via the Smith chart techniques [102].

The index i in the power reflection coefficient $|\Gamma_{i,k}|^2$ is dropped because a set of load

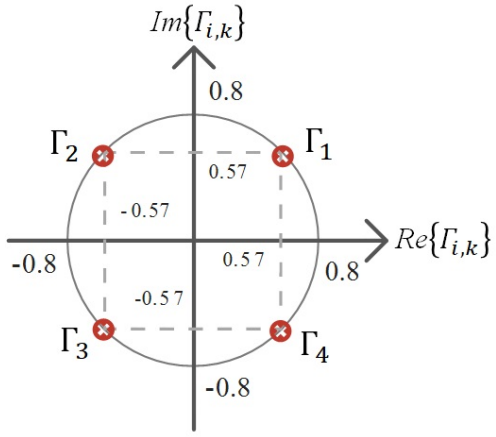

Figure 3.2: QPSK backscatter modulator design.

impedance values can be designed to keep $|\Gamma_{i,k}|^2$ constant while varying the phase of $\Gamma_{i,k}$. Therefore, let $\alpha_k = |\Gamma_{i,k}|^2$, representing the power reflection coefficient of the k-th tag. It is assumed that the tag design will achieve $0 < \alpha_k < 1$ [90, 91, 98, 99].

For example, Figure 3.2 shows the QPSK backscatter modulator for a tag. The power reflection coefficient (e.g., α) is 0.8 for all four modulation symbols, while the phase (e.g., θ_i) can be selected based on the tag's information bits.

A2: The SI cancellation process at the reader is imperfect. The reader's hardware circuits will not ideally suppress the SI signal. Parameter β is introduced as the hard SI suppression threshold to quantify the RSI level. This factor models the effect of passive/active SI cancellation techniques such as antenna isolation and filtering circuits. The case of $\beta = 0$ denotes the perfect SI cancellation case. The smaller β is, the better cancellation is reached. For instance, previous works [26, 48, 91] implicitly assume $\beta = 0$ (e.g., perfect cancellation). For practical systems, RF/analog circuits provide up to 90 dB SI suppression [94]. However, because of RF impairments and other imperfections, the $\beta = 0$ assumption may not be realistic.

A3: The EH process of each tag follows a linear model. Although practical EH circuits have non-linear characteristics and a rather limited linear region [38, 103], these may be linearized by concatenating multiple EH circuits, which extend the linear region.

A4: The reader has full CSI. This assumption is standard for all most studies. The reader

can perform channel estimation (CE) based on standard pilot transmission techniques. However, the ability of passive tags to transmit pilots is limited [104]. However, tags can reflect the pilots transmitted by the reader, enabling a least square estimator (LSE) [105]. Although CSI estimation is complicated in Ambient BackComm, some results are emerging (see [106] and reference therein). An alternative is blind CE (e.g., without pilots). Moreover, based on the RFID protocol, the overhead of the system for tag-reader frame synchronization signaling is at least $34\,\mu$s [107].

A5: The channels **R**-to-$\mathbf{T_k}$, $\mathbf{T_k}$-to-**R** are Rayleigh fading with $\mathbf{h}_{T_k}^f \in \mathcal{CN}\left(\mathbf{0}_{N_t\times 1}, \xi_{T_k}^f \mathbf{I}_{N_t}\right)$, $\mathbf{h}_{T_k}^b \in \mathcal{CN}\left(\mathbf{0}_{N_r\times 1}, \xi_{T_k}^b \mathbf{I}_{N_r}\right)$, where $\xi_{T_k}^f$ and $\xi_{T_k}^b$ indicate the downlink and uplink channels path-loss. The Rayleigh model is appropriate for environments that are highly scattered, where the line-of-sight (LoS) component is negligible or absent. Examples of such environments include dense urban areas and indoor settings.

A6: The SI channel $\mathbf{H}_{\text{SI}} = [h_{ij}^{\text{SI}}] \in \mathcal{C}^{N_r\times N_t}$ is modeled as a Rician fading channel [93]. Denote h_{ij}^{SI} the (i,j)-th element of H_{SI}. The SI channel comprises the LOS and the non-line-of-sight (NLOS) parts. Therefore, the SI channel model is given by

$$h_{ij}^{\text{SI}} = \sqrt{\frac{1}{\bar{K}+1}} h_{\text{LOS}}^{\text{SI}} + \sqrt{\frac{\bar{K}}{\bar{K}+1}} h_{\text{NLOS}}^{\text{SI}}, \tag{3.2}$$

where $\bar{K}$ denotes the Rician factor, $h_{\text{LOS}}^{\text{SI}}$ represent the deterministic part subject to $\|h_{\text{LOS}}^{\text{SI}}\|^2 = 1$, and $h_{\text{NLOS}}^{\text{SI}} \sim \mathcal{CN}(0,1)$. Consequently, higher $\bar{K}$ indicates a strong SI channel at the **R**.

A7: A block fading model is assumed for all the channels with a given coherence time, which depends on several factors, including the carrier frequency and the velocity of the reader. For instance, at 2.45 GHz and a speed of 2 km/h, it is roughly 83 ms [53], indicating that this coherence time is large enough for CE.

3.2.1 Transmission Scheme

Reader $\mathbf{R}$ transmits signal $\mathbf{x} = \sqrt{P_T}\mathbf{f}s$, where P_T is the transmit power, $s \sim \mathcal{CN}(0,1)$ is the $\mathbf{R}$ transmit symbol, and $\mathbf{f} \in \mathcal{C}^{N_t \times 1}$ denotes the precoding vector. It is assumed that the precoder vector is identical for all tags, which is optimal since the transmit signal is only used to power the tag circuits [48]. Consequently, the receives signal at $\mathbf{T_k}$, $k \in \mathcal{K}$ can be expressed as $y_{T_k} = (\mathbf{h}^f_{T_k})^T\mathbf{x},\ k \in \mathcal{K}$. Note that since the tag lacks RF components, it does not introduce any noise to the signal. Accordingly, the received signal at the $\mathbf{R}$ is given by

$$\mathbf{y}_R = \sum_{k=1}^{K} \sqrt{\alpha_k}\mathbf{h}^b_{T_k}(\mathbf{h}^f_{T_k})^T\mathbf{x}b_k + \hat{\mathbf{H}}_{\text{SI}}\mathbf{x}+\mathbf{n}_R, \tag{3.3}$$

where the first term in (3.3) is the reflected signals from all tags. The backscatter modulation symbol of the k-th tag is b_k, $k \in \mathcal{K}$, which is selected from the M-ary PSK constellation, and it satisfies the energy constraint $\mathbb{E}\{|b_k|^2\} = 1$, and $\alpha_k \in [0,1]$ is the reflection coefficient of $\mathbf{T}_k$, $k \in \mathcal{K}$.

Note that increasing the value of α_k increases the amount of power reflected back to the $\mathbf{R}$. The second term in (3.3) is the RSI at $\mathbf{R}$, where $\hat{\mathbf{H}}_{\text{SI}} = \sqrt{\beta}\mathbf{H}_{\text{SI}}$ and $0 \leq \beta \ll 1$ is a constant denoting the SI cancellation ability of $\mathbf{R}$. Furthermore, $\mathbf{n}_R \sim \mathcal{CN}(\mathbf{0}_{N_r \times 1}, \sigma^2_R\mathbf{I}_{N_r})$ is the additive white Gaussian noise (AWGN) at the $\mathbf{R}$.

Since the tags transmit simultaneously (i.e., SDMA), the reader must separate their signal signals. For this purpose, it applies the linear detection matrix, i.e., $\mathbf{G} = [\mathbf{g}_1, \ldots \mathbf{g}_k, \ldots, \mathbf{g}_K] \in \mathcal{C}^{N_r \times K}$, where $\mathbf{g}_k \in \mathcal{C}^{N_r \times 1}$ indicates the combiner vector to spatially separate data of $\mathbf{T}_k$ embedded in $\mathbf{y}_R$. Thus, by separating the desired signal, interference terms, and additive noise of (3.3), the received SINR at the $\mathbf{R}$ for the k-th data stream from $\mathbf{T}_k$, $k \in \mathcal{K}$, can be written as

$$\gamma_k = \frac{\alpha_k|\mathbf{g}_k^H\mathbf{h}^b_{T_k}|^2|(\mathbf{h}^f_{T_k})^T\mathbf{f}|^2}{\sum_{j\neq k}^{K}\alpha_j|\mathbf{g}_k^H\mathbf{h}^b_{T_j}|^2|(\mathbf{h}^f_{T_j})^T\mathbf{f}|^2 + \beta|\mathbf{g}_k^H\mathbf{H}_{\text{SI}}\mathbf{f}|^2 + \frac{\sigma^2_R}{P_T}\|\mathbf{g}_k\|^2}, \tag{3.4}$$

where the nominator term in (3.4) is the desired received signal power from $\mathbf{T}_k$, and the denominator comprises the powers of the interference signals, RSI, and noise, respectively. More specifically, the first term of the denominator is the total interference signal power

received from other tags, the second term represents the RSI at the **R**, and the last term is the additive Gaussian noise power. Unlike previous works [26, 48, 91], which ignore the RSI term ($\beta = 0$), this analysis fully considers the effect of RSI. Indeed, assuming perfect SI removal ($\beta = 0$), (3.4) reduces to

$$\gamma_k^{\mathrm{SIC}_P} = \frac{\alpha_k |\mathbf{g}_k^H \mathbf{h}_{T_k}^b|^2 |(\mathbf{h}_{T_k}^f)^T \mathbf{f}|^2}{\sum_{j \neq k}^{K} \alpha_j |\mathbf{g}_k^H \mathbf{h}_{T_j}^b|^2 |(\mathbf{h}_{T_j}^f)^T \mathbf{f}|^2 + \frac{\sigma_R^2}{P_T} \|\mathbf{g}_k\|^2}, \ k \in \mathcal{K}. \tag{3.5}$$

That is the case study of the previous works [48, Eq. (5)], [26, Eq. (5)], [91, Eq. (9)].

The backscattered sum rate for $\mathbf{T}_k$, $k \in \mathcal{K}$, at the **R** is given by

$$R_k = \log_2(1 + \gamma_k) \text{ [bps/Hz]}. \tag{3.6}$$

Note that this rate is a function of cascaded channels, RSI, and AWGN. At the system level, what matters is the sum throughput achieved by the **R** in the uplink. Thus, the total sum rate of interest can be expressed as

$$R_S = \sum_{k=1}^{K} \log_2(1 + \gamma_k) \text{ [bps/Hz]}. \tag{3.7}$$

The system metric R_S will form the basis for the subsequent optimization problems.

3.3 Problem Formulation

The basic passive tag architecture is shown in Figure 2.2. The tag has EH and modulation blocks. These blocks are described under assumptions A1 and A3. The fraction α_k of the incident RF signal is reflected to enable data communication [34]. The remaining $(1 - \alpha_k)$ propagates to the EH circuit consisting of a rectifier and a capacitor. As a result, the adjustable power reflection coefficient of the tag can also be interpreted as a power splitter [34]. Thus, the amount of harvested energy at $\mathbf{T_k}$, $k \in \mathcal{K}$ can be stated as $\mathrm{P}_{\mathrm{EH}_k} = (1 - \alpha_k)\eta P_T |(\mathbf{h}_{T_k}^f)^T \mathbf{f}|^2$, where $\eta \in (0, 1]$ is the efficiency of RF signal to direct current (DC) energy conversion [90]. In particular, η varies according to the different EH technologies. For

instance, photovoltaic and piezoelectric circuits can achieve up to 40% and 30% efficiency, respectively [36].

Our goal is to maximize the sum rate by jointly optimizing the precoder $\{\mathbf{f}\}$, combiners vectors $\{\mathbf{g}_k\}_{k=1}^K$, and reflection coefficients $\{\alpha_k\}_{k=1}^K$ while maintaining minimum harvested power at each tag and maximum RSI level at the $\mathbf{R}$. Indeed, the minimum EH constraint ensures that the passive tag is activated successfully. However, it can also help semi-passive tags reduce battery replacement or recharging cycles. As a result, the following problem formulation and the resulting algorithms can benefit both passive and semi-passive tags.

Remark 1. *In cellular networks, maximizing fairness among users plays a vital role in guaranteeing the minimum required rate for every user. However, the Monostatic BackComm tags employ passive backscatter modulation to transmit their data. Thus, fairness is not a critical issue here. Accordingly, the sum rate must be maximized [26, 48].*

As a result, the corresponding optimization problem can be formulated as follows:

$$
\begin{aligned}
(\text{P3.1}): \quad & \max_{\alpha_k, \mathbf{g}_k, \mathbf{f}} \quad R_S, && \text{(3.8a)}\\
& \text{s.t.} \quad \beta |\mathbf{g}_k^H \mathbf{H}_{\text{SI}} \mathbf{f}|^2 \leq \lambda, \ \forall k, && \text{(3.8b)}\\
& \qquad \text{P}_{\text{EH}_k} \geq P_{\text{th}}, \ \forall k, && \text{(3.8c)}\\
& \qquad 0 < \alpha_k < 1, \ \forall k, && \text{(3.8d)}\\
& \qquad \|\mathbf{f}\|^2 = 1, \|\mathbf{g}_k\|^2 = 1, \ \forall k, && \text{(3.8e)}
\end{aligned}
$$

where λ and P_{th} denote the software threshold of the RSI and power threshold, respectively. The software threshold refers to the fact that this suppression is done at the signal processing level, which is distinct from the hardware-aided RSI suppression at the $\mathbf{R}$ characterized by β. Constraint (3.8b) indicates the maximum RSI power level at the $\mathbf{R}$. Constraint (3.8c) denotes the minimum EH at each tag. Finally, constraints (3.8d) and (3.8e) are inherent limits for the reflection coefficients and unit norm of precoding as well as combining vectors, respectively. Note that the energy threshold is positive ($P_{\text{th}} > 0$). Therefore, α_k requires to meet strict inequality $0 < \alpha_k < 1$, denoted by constraint (3.8d). Evidently, (3.8c) and (3.8b) are intertwined from $\mathbf{f}$, and (3.8c) as well as (3.8d) are connected via α_k. This joint

optimization problem is non-convex as optimization variables are coupled, also constraint (3.8c) is non-convex.

Remark 2. *The proposed sum rate maximization problem (P3.1) is novel since the EH constraint (3.8c) and the RSI constraint at the* $\mathbf{R}$ *(3.8b) have not been studied previously (Table 3.1).*

3.4 Proposed Solution

Problem (P3.1) is non-convex as the objective function contains entangled terms involving the product of optimization variables. To handle this issue, the AO algorithm [108] is employed. The key idea of the AO algorithm is as follows. To solve, say, $\min_x f(x)$, where $x \in \mathbb{R}^s$ is partitioned into $m > 1$ blocks as $x = (x_1, x_2, \ldots, x_m)^T$, where $x_k \in \mathbb{R}^{s_k}$ and $\sum_{k=1}^{m} s_k = s$. The minimization is then performed over x_1 while $\{x_k | k \neq 1\}$ are kept constant at their previous values; next, the minimization is performed over x_2 while $\{x_k | k \neq 2\}$ are kept constant at their previous values. This cyclic process thus continues until convergence. The AO algorithm yields a locally optimum solution [108].

To apply the AO algorithm, (P3.1) is decomposed into three suboptimal problems. In each subproblem, the sum rate is maximized over each individual block variable $\mathbf{f}, \mathbf{G}$, and $\boldsymbol{\alpha} = [\alpha_1, \ldots, \alpha_k]$, while the other two block variables are fixed. The result is then used in the next subproblem. Therefore, each block variable is optimized iteratively until the objective function converges.

In the first subproblem, the combining vectors and reflection coefficients are fixed, and the precoding vector $\mathbf{f}$ is optimized. However, the objective in (P3.1) is a non-concave function over $\mathbf{f}$ due to the incorporation of interference and RSI. To address this, the SDR technique is applied, involving a new matrix definition that satisfies the rank-one constraint. The rate function is then rewritten in terms of the difference of convex functions, and the first-order Taylor approximation is applied to obtain a locally optimal solution, which is the essence of the SCA technique.

In the second subproblem, the precoding vector and power reflection coefficients are fixed, and the combiner is optimized. The specific structure of the obtained SINR of each tag is

exploited. The objective is cast as a generalized Rayleigh quotient, yielding the optimal combiner vector in a closed-form solution.

The third subproblem involves optimizing the reflection coefficients. Although the rate of each tag is a pseudo-linear function of α_k, the sum rate maximization problem is not a convex problem [48]. Therefore, no global optimal solution can be guaranteed. However, it can be interpreted as a wireless power control problem. To find a solution, GP, a power control technique, can be applied [109]. More specifically, the GP objective is a posynomial function of the form $f(x) = cx_1^{a_1} \dots x_n^{a_n}$ and equality constraints are monomial functions of type $f(x) = \sum_{k=1}^{K} c_k x_1^{a_{1k}} \dots x_n^{a_{nk}}$ [110].

The new optimization algorithms are developed next.

3.4.1 Optimization Over f

For given $\mathbf{g}_k$ and α_k, $\forall k \in \mathcal{K}$, the sum rate problem turns into a precoder optimization problem represented as follows:

$$
\begin{aligned}
(\text{P3.2}): \quad \max_{\mathbf{f}} \quad & R_S, && \text{(3.9a)}\\
\text{s.t.} \quad & \beta |\mathbf{g}_k^H \mathbf{H}_{\text{SI}} \mathbf{f}|^2 \leq \lambda, \ \forall k, && \text{(3.9b)}\\
& (1-\alpha_k) P_T \eta |(\mathbf{h}_{T_k}^f)^T \mathbf{f}|^2 \geq P_{\text{th}}, \ \forall k, && \text{(3.9c)}\\
& \|\mathbf{f}\|^2 = 1, \ \forall k. && \text{(3.9d)}
\end{aligned}
$$

Generally, the objective function of (P3.2) is not concave over $\mathbf{f}$. To address this, the SDR technique is applied [111]. Let us define a new optimization variable $\mathbf{F} = \mathbf{f}\mathbf{f}^H$, where matrix $\mathbf{F}$ is semidefinite and satisfies rank-one constraint, i.e., $\text{Rank}(\mathbf{F}) = 1$ [112]. By doing this, the quadratic ratio function inside the $\log(\cdot)$ in the objective function can be turned into its equivalent linear ratio over $\mathbf{F}$, ending with a concave objective function. Since $|\mathbf{g}_k^H \mathbf{H}_{\text{SI}} \mathbf{f}|^2$ is a scalar variable, it can be written as $\text{Tr}(\mathbf{g}_k^H \mathbf{H}_{\text{SI}} \mathbf{f}\mathbf{f}^H \mathbf{H}_{\text{SI}}^H \mathbf{g}_k)$. With the new optimization

variable, this becomes $\mathrm{Tr}(\mathbf{g}_k^H \mathbf{H}_{\mathrm{SI}} \mathbf{F} \mathbf{H}_{\mathrm{SI}}^H \mathbf{g}_k)$. Thus, problem (P3.2) can be reformulated as

$$
\begin{aligned}
(\mathrm{P3.2.1}): \quad \max_{\mathbf{F}} \quad & \Gamma, && \text{(3.10a)}\\
\text{s.t.} \quad & \beta \mathrm{Tr}\left(\mathbf{g}_k^H \mathbf{H}_{\mathrm{SI}} \mathbf{F} \mathbf{H}_{\mathrm{SI}}^H \mathbf{g}_k\right) \leq \lambda, \ \forall k, && \text{(3.10b)}\\
& \mathrm{Tr}\left((\mathbf{h}_{T_k}^f)^T \mathbf{F} \mathbf{h}_{T_k}^f\right) \geq P'_{\mathrm{th}}, \ \forall k, && \text{(3.10c)}\\
& \mathrm{Tr}(\mathbf{F}) = 1, && \text{(3.10d)}\\
& \mathrm{Rank}(\mathbf{F}) = 1, && \text{(3.10e)}
\end{aligned}
$$

where $P'_{\mathrm{th}} = \frac{P_{\mathrm{th}}}{(1-\alpha_k)\eta P_T}$ and

$$
\Gamma \triangleq \sum_{k=1}^{K} \log\left(1 + \frac{\alpha_k |\mathbf{g}_k^H \mathbf{h}_{T_k}^b|^2 \mathrm{Tr}\left((\mathbf{h}_{T_k}^f)^T \mathbf{F} \mathbf{h}_{T_k}^f\right)}{\sum_{j \neq k}^{K} \alpha_j |\mathbf{g}_k^H \mathbf{h}_{T_j}^b|^2 \mathrm{Tr}\left((\mathbf{h}_{T_j}^f)^T \mathbf{F} \mathbf{h}_{T_j}^f\right) + \beta |\mathbf{g}_k^H \mathbf{H}_{\mathrm{SI}} \mathbf{f}|^2 + \frac{\sigma_R^2}{P_T} \|\mathbf{g}_k\|^2}\right). \quad \text{(3.11)}
$$

Problem (P3.2.1) is still not a convex problem due to constraint (3.10e). To tackle it, we drop (3.10e) and resort to the SCA technique using the first-order Taylor series approximation near a feasible point $\mathbf{F}^o$. Indeed, the first-order Taylor approximation is a linear approximation of a function $f(x)$ near a feasible point $x = a$ (if it is differentiable at this point) such that $f(x) = f(a) + f'(a)(x - a)$, where $f'(\cdot)$ indicates the derivative of $f(\cdot)$. Subsequently, (P3.2.1) is relaxed into

$$
\begin{aligned}
(\mathrm{P3.2.2}): \quad \max_{\mathbf{F}} \quad & \sum_{k=1}^{K} \log\left(A_k\right) - B_k(\mathbf{F}, \mathbf{F}^o), && \text{(3.12a)}\\
\text{s.t.} \quad & \text{(3.10b)–(3.10d)}, && \text{(3.12b)}
\end{aligned}
$$

where the definition of A_k and $B_k(\mathbf{F}, \mathbf{F}^o)$ respectiely are:

$$A_k = \sum_{i=1}^{K} \alpha_i |\mathbf{g}_k^H \mathbf{h}_{T_i}^b|^2 \mathrm{Tr}\left((\mathbf{h}_{T_i}^f)^T \mathbf{F} \mathbf{h}_{T_i}^f\right) + \beta |\mathbf{g}_k^H \mathbf{H}_{\mathrm{SI}} \mathbf{f}|^2 + \frac{\sigma_R^2}{P_T} \|\mathbf{g}_k\|^2, \tag{3.13}$$

$$B_k(\mathbf{F}, \mathbf{F}^o) = \log\left(\sum_{j \neq k} \alpha_j |\mathbf{g}_k^H \mathbf{h}_{T_j}^b|^2 \mathrm{Tr}\left((\mathbf{h}_{T_j}^f)^T \mathbf{F}^o \mathbf{h}_{T_j}^f\right) + \beta \mathrm{Tr}\left(\mathbf{g}_k^H \mathbf{H}_{\mathrm{SI}} \mathbf{F}^o \mathbf{H}_{\mathrm{SI}}^H \mathbf{g}_k\right) + \frac{\sigma_R^2}{P_T} \|\mathbf{g}_k\|^2\right)$$
$$+ \mathrm{Tr}(\mathbf{F} - \mathbf{F}^o) \times \frac{\sum_{j \neq k} \alpha_j |\mathbf{g}_k^H \mathbf{h}_{T_j}^b|^2 \mathrm{Tr}\left((\mathbf{h}_{T_j}^f)^T \mathbf{h}_{T_j}^f\right) + \beta \mathrm{Tr}\left(\mathbf{g}_k^H \mathbf{H}_{\mathrm{SI}} \mathbf{H}_{\mathrm{SI}}^H \mathbf{g}_k\right)}{\sum_{j \neq k} \alpha_j |\mathbf{g}_k^H \mathbf{h}_{T_j}^b|^2 \mathrm{Tr}\left((\mathbf{h}_{T_j}^f)^T \mathbf{F}^o \mathbf{h}_{T_j}^f\right) + \beta \mathrm{Tr}\left(\mathbf{g}_k^H \mathbf{H}_{\mathrm{SI}} \mathbf{F}^o \mathbf{H}_{\mathrm{SI}}^H \mathbf{g}_k\right) + \frac{\sigma_R^2}{P_T} \|\mathbf{g}_k\|^2}. \tag{3.14}$$

The solution of (P3.2.2) provides an upper bound for (P3.2) due to the SCA technique and relaxing the rank-one constraint. To tighten the obtained upper bound, the feasible solution $\mathbf{F}$ in (P3.2.2) is updated iteratively by using convex optimization tools such as CVX [113] to find a suboptimal solution.

Algorithm 1 details the proposed SCA-based Algorithm, and the convergence proof can be found in [114]. Specifically, if $\mathbf{F}^*$ which is the optimal solution to (P3.2.2) satisfies the rank-one constraint, the optimal beamforming vector, $\mathbf{f}$, can be obtained by performing eigenvalue decomposition (EVD) over $\mathbf{F}^*$. Unlike [48], which applies Gaussian randomization to recover $\mathbf{f}^*$ as a suboptimal solution, the following Proposition reveals that the SDR solution of (P3.2.2) is tight and yields an optimal solution.

Proposition 1. *Let the optimal solution of problem (P3.2.2) be* $\mathbf{F}^*$*. If all channel links are statistically independent,* $\mathbf{F}^*$ *satisfies Rank*$(\mathbf{F}) = 1$.

Proof. Problem (P3.2.2) is a convex optimization problem and satisfies Slater's condition, indicating that the duality gap between the primal and dual problems is zero. Thus, the Lagrangian function of the associated problem is expressed as follows:

$$\mathcal{L}(\mathbf{F}, \mathbf{Z}, \phi_i, \mu_i) = \sum_{k=1}^{K} [\log(\mathrm{Tr}(\mathbf{V}_k \mathbf{F}) + C_k) - f(\mathbf{F}^o)$$
$$- \mathrm{Tr}(\mathbf{F} - \mathbf{F}^o) g(\mathbf{F}^o)] + \mathrm{Tr}(\mathbf{P}_k \mathbf{F}) - \mathrm{Tr}(\mathbf{E}\mathbf{F}) - \mathrm{Tr}(\mathbf{Z}\mathbf{F}) + d - c, \tag{3.15}$$

where

$$\mathbf{V}_k = \sum_{i=1}^{K} \alpha_i |\mathbf{g}_k^H \mathbf{h}_{T_i}^b|^2 \left(\mathbf{h}_{T_i}^f (\mathbf{h}_{T_i}^f)^T \right) + \beta \mathbf{H}_{\mathrm{SI}}^H \mathbf{g}_k \mathbf{g}_k^H \mathbf{H}_{\mathrm{SI}},$$
$$\mathbf{P}_k = \sum_{i=1}^{K} \mu_i \beta \mathbf{H}_{\mathrm{SI}}^H \mathbf{g}_k \mathbf{g}_k^H \mathbf{H}_{\mathrm{SI}}, \quad \mathbf{E} = \sum_{i=1}^{K} \phi_i \mathbf{h}_{T_i}^f (\mathbf{h}_{T_i}^f)^T,$$
$$c = \sum_{i=1}^{K} \mu_i \lambda, \quad d = \sum_{i=1}^{K} \phi_i P'_{\mathrm{th}}, \quad C_k = \frac{\sigma_R^2}{P_T} \|\mathbf{g}_k\|^2. \tag{3.16}$$

In particular, $\mathbf{Z} \succeq 0$, $\mu_i \geq 0$, and $\phi_i \geq 0$ indicate the no-negative Lagrangian multipliers associated with the constraints of (P3.2.2). In addition, $f(\mathbf{F}^o)$ and $g(\mathbf{F}^o)$ are two functions depending on the initial value of the SDR problem, $\mathbf{F}^o$. The Taylor expansion $\log(1+x) \approx x$ can be used in the low SNR region since the high powers of x are negligible. By further applying the Karush-Kuhn-Tucker (KKT) criteria, the following conditions arise:

$$\mathbf{Z}^* \succeq 0, \quad \mu_i^* \geq 0 \quad \phi_i^* \geq 0, \tag{3.17}$$
$$\mathbf{Z}^* \mathbf{F}^* = \mathbf{0}, \tag{3.18}$$
$$\mathbf{Z}^* = \underbrace{\sum_{k=1}^{K} \mathbf{V}_k^* - g(\mathbf{F}^o)\mathbf{I}_{N_t}}_{\mathbf{W} \succeq 0} + (\mathbf{P}_k^* - \mathbf{E}^*). \tag{3.19}$$

Subsequently, by using the fact that $\mathrm{Rank}(\mathbf{A}+\mathbf{B}) \leq \mathrm{Rank}(\mathbf{A}) + \mathrm{Rank}(\mathbf{B})$, (3.19) can be written as $\mathrm{Rank}(\mathbf{Z}^*) + \mathrm{Rank}(\mathbf{E}^* - \mathbf{P}_k^*) \geq \mathrm{Rank}(\mathbf{W}) = N_t$. As can be observed, one can reach the following inequality: $\mathrm{Rank}(\mathbf{Z}^*) \geq N_t - 1$. On the other hand, according to (3.18), it can be deduced that $\mathrm{Rank}(\mathbf{Z}^*) = N_t - 1$. Otherwise, one has $\mathrm{Rank}(\mathbf{F}^*) = 0$, which is not the optimal case. Consequently, it is clear that $\mathrm{Rank}(\mathbf{F}^*) = 1$, and the proof is completed. □

Based on Proposition 1, the optimal solution to (P3.2.2) can be obtained by performing EVD over $\mathbf{F}^*$. The solution steps are summarized in Algorithm 1. It starts with an initial precoder $(\mathbf{F}^o)^{(it)} = \mathbf{f}\mathbf{f}^H$ at iteration $it = 1$. Indeed, as this precoder should satisfy the RSI constraint, one possible choice is to select the eigenvector of the SI channel corresponding to its minimum eigenvalue. It continues to update $\mathbf{F}^o$ iteratively by solving (P3.2.2) until the objective function in (P3.2.2) converges. The optimal precoder $\mathbf{f}^*$ is recovered by computing

Algorithm 1 :Iterative Precoder Optimization

1: Input: Set $it = 1$, initial $\mathbf{f}$, and $(\mathbf{F}^o)^{(it)} = \mathbf{f}\mathbf{f}^H$.
2: **while** (3.12a) does not converge **do**
3: Solve (3.12a) to derive $\mathbf{F}^{(it)}$.
4: Update $(\mathbf{F}^o)^{(it)} \leftarrow \mathbf{F}^{(it)}$.
5: $it = it + 1$;
6: **end while**
7: **Return** $\mathbf{F}^{*(it)}$ where $\mathbf{f}^\star$ is simply the eigenvector corresponding to the non-zero eigenvalue of $\mathbf{F}^{*(it)}$.

the eigenvector corresponding to the non-zero eigenvalue of $\mathbf{F}^{*(it)}$ at iteration it.

3.4.2 Optimization Over Combiner $\mathbf{g}_k$

Since the corresponding SINR of each tag observed at the $\mathbf{R}$ depends on its associate combiner vector, the sum rate is maximized by optimizing the SINR of each tag individually. Accordingly, one has

$$(\text{P3.3}): \quad \max_{\mathbf{g}_k} \quad \frac{\alpha_k |\mathbf{g}_k^H \mathbf{h}_{T_k}^b|^2 |(\mathbf{h}_{T_k}^f)^T \mathbf{f}|^2}{\sum_{j \neq k} \alpha_j |\mathbf{g}_k^H \mathbf{h}_{T_j}^b|^2 |(\mathbf{h}_{T_j}^f)^T \mathbf{f}|^2 + \beta |\mathbf{g}_k^H \mathbf{h}_{\text{SI}} \mathbf{f}|^2 + \frac{\sigma_R^2}{P_T} \|\mathbf{g}_k\|^2}, \tag{3.20a}$$

$$\text{s.t.} \quad \|\mathbf{g}_k\|^2 = 1, \ \forall k. \tag{3.20b}$$

By rewriting the objective function in (3.20a), the following optimization problem arises:

$$(\text{P3.3.1}): \quad \max_{\mathbf{g}_k} \quad \frac{\mathbf{g}_k^H \mathbf{h}_{T_k}^b (\mathbf{h}_{T_k}^b)^H \mathbf{g}_k}{\mathbf{g}_k^H \mathbf{Q} \mathbf{g}_k}, \tag{3.21a}$$

$$\text{s.t.} \quad \|\mathbf{g}_k\|^2 = 1, \ \forall k, \tag{3.21b}$$

where

$$\mathbf{Q} = \mathbf{I}_{N_r} + \frac{P_T}{\sigma_R^2} \left(\sum_{j \neq k} \alpha_j \mathbf{h}_{T_j}^b (\mathbf{h}_{T_j}^b)^H |(\mathbf{h}_{T_j}^f)^T \mathbf{f}|^2 + \beta \mathbf{H}_{\text{SI}} \mathbf{F} \mathbf{H}_{\text{SI}}^H \right). \tag{3.22}$$

For a given precoder and set of reflection coefficients, the optimal combiner vector is

Algorithm 2 Iterative α_k optimization

1: Input: Set $it = 1$, tolerance $\epsilon > 0$, initial $\alpha_k^{(it)}$, given $\mathbf{f}$ and $\mathbf{g}_k$, initial guess of SINR, $\hat{\gamma}_m^{(it)}$.
2: **while** $\max_{m \in K} |\gamma_m^* - \hat{\gamma}_m^{(it)}| \geq \epsilon$ **do**
3: Solve (3.25a) to obtain $\alpha_k^{(it)}$ and γ_m^*.
4: Update $\hat{\gamma}_m^{(it)} \leftarrow \gamma_m^*$.
5: $it \leftarrow it + 1$;
6: **end while**
7: **Return** $\alpha_k^{*(it)}$.

given by

$$\mathbf{g}_k^* = \frac{\mathbf{Q}^{-1}\mathbf{h}_{T_k}^b}{\|\mathbf{Q}^{-1}\mathbf{h}_{T_k}^b\|}, \ k \in \mathcal{K}, \tag{3.23}$$

which is an MMSE filter [48].

Once both precoder $\mathbf{f}$ and combiners $\mathbf{g}_k$, $k \in \mathcal{K}$, are determined, the next step is to optimize the reflection coefficients of the tags.

3.4.3 Optimization Over α_k

As the objective function (3.8a) is a linear-fractional function of α, it is a pseudolinear (both pseudoconvex and pseudoconcave) for α_k [48]. However, the sum rate problem in (3.8a) does not preserve the pseudolinearity property. Thus, the globally optimal values cannot be achieved. Nevertheless, it can be represented as a conventional power allocation problem. Then, the problem can be recast as below:

$$\text{(P3.4)}: \quad \max_{\gamma_m, \alpha_k} \quad \sum_{m=1}^{K} \log(1 + \gamma_m), \tag{3.24a}$$

$$\text{s.t.} \quad \gamma_k > \gamma_m, \ \forall k \tag{3.24b}$$

$$0 < \alpha_k < 1, \ \forall k, \tag{3.24c}$$

$$\text{(3.8c)}, \tag{3.24d}$$

where γ_m is a slack variable. By considering that the objective of (3.24) is an increasing function over γ_m, and also $\log(\cdot)$ is a monotonically increasing function, it can be reformulated equivalently as $\min_{\gamma_m,\alpha_k} \prod_{m=1}^{K} (1+\gamma_m)^{-1}$. Note that the constraints of (P3.4) are posynomial functions. Therefore, if the objective is a monomial or posynomial function, (P3.4) becomes a GP, which is a convex problem. Since the objective is neither monomial nor posynomial, we must approximate $\prod_{m=1}^{K} (1+\gamma_m)^{-1} \approx \prod_{m=1}^{K} b\gamma_m^a$ near an arbitrary point $\hat{\gamma} > 0$, where $a = \hat{\gamma}_m (1+\hat{\gamma}_m)^{-1}$, $b = \hat{\gamma}_m^{-a}(1+\hat{\gamma}_m)$. The proof of this result is provided in [115, Lemma 1]. Since coefficient b is a scalar, ignoring it does not change the optimized value of the reflection coefficient. As a result, (P3.4) is reformulated as follows:

$$
\begin{aligned}
(\text{P3.4.1}): \quad \min_{\gamma_m,\alpha_k} \quad & \prod_{m=1}^{K} \gamma_m^{-\frac{\hat{\gamma}_m}{1+\hat{\gamma}_m}}, && \text{(3.25a)}\\
\text{s.t.} \quad & \gamma_k > \gamma_m, \ \forall k, && \text{(3.25b)}\\
& \nu^{-1}\hat{\gamma}_m < \gamma_m \leq \nu\hat{\gamma}_m, && \text{(3.25c)}\\
& 0 < \alpha_k < 1, \ \forall k, && \text{(3.25d)}\\
& \text{(3.8c)}, && \text{(3.25e)}
\end{aligned}
$$

where $\hat{\gamma}_m$ denotes the initial guess for the required SINR of each user, which can be obtained by substituting an initial precoder, combiners, and reflection coefficients into (4.4). Besides, $\nu > 1$ controls the desired approximation accuracy and the convergence speed as in each entry. In particular, $\hat{\gamma}_m$ can be increased or decreased by factor ν. Thus, ν near 1 provides an accurate approximation with the cost of slower convergence. On the other hand, ν larger than 1 converges faster with the cost of low accuracy. Reference [116] shows that $\nu = 1.1$ obtains a nice trade-off between accuracy and convergence speed in most practical cases.

Problem (P3.4.1) is a GP problem [109] that can be solved efficiently by using CVX [113]. Algorithm 2 represents the detailed steps to return optimal α_k. It starts with initial random value for α_k via given $\mathbf{f}$ and $\mathbf{g}_k$, $k \in \mathcal{K}$. Given these parameters, it calculates the initial guess of SINR, $\hat{\gamma}_m^{(it)}$, at iteration $it = 1$ based on (4.4). It then solves (P3.4.1) and updates $\hat{\gamma}_m^{(it)}$ for a optimized α_k^*. It continues until the SINR improvement is below a predetermined threshold. Ultimately, the overall AO algorithm is represented in Algorithm 3. It selects initial $\mathbf{f}$ and $\boldsymbol{\alpha}$

randomly and obtains optimal choices for $\mathbf{f}$, $\boldsymbol{\alpha}$, and $\mathbf{G}$. The outline is as follows. In the first step, initial values are set. Then for given $\mathbf{f}$ and $\boldsymbol{\alpha}$, it derives the combiners vector based on (3.23). It then uses $\mathbf{g}_k^{*(it)}$ and $\alpha_k^{(it)}$ to derive $\mathbf{f}^{*(it)}$ based on Algorithm 1. Afterward, it uses $\mathbf{f}^{*(it)}$ and $\mathbf{g}_k^{*(it)}$ to obtain reflection coefficients based on Algorithm 2. It continues to repeat until the improvement of the sum rate is below a certain threshold.

It is important to note that the reader can address and solve this optimization problem. Once the optimization is complete, the reader can communicate this optimized reflection coefficient to each tag using commands defined in the EPC Gen 2 standard [107]. The EPC Gen 2 standard provides a framework for command and control in RFID systems, specifying how readers and tags should interact. This includes a range of commands for tasks such as reading data, writing data, and configuring tag settings. Through this command and control sequence, the reader can instruct each tag to adjust its reflection coefficient, which is crucial for fine-tuning the tag's performance and improving overall system functionality.

Proposition 2. *Algorithm 3 converges to a suboptimal point since (P3.2) is non-increasing as the objective function value increases over each iteration in Algorithm 1. Specifically, after each iteration in Algorithm 1, the value of the objective function in (P3.2) improves.*

Proof. The convergence of Algorithm 3 is proven next. However, we do not consider the combiner vector since it has a closed-form solution, and as discussed previously, using (3.23) can maximize the received SINR of each tag at $\mathbf{R}$. Let us consider $\{\alpha_k^{(it+1)}, \mathbf{F}^{(it)}, \mathbf{g}^{(it)}\}$ as the feasible solution set to (P3.4.1); then it is also a feasible solution to (P3.2.2). Consequently, $\{\alpha_k^{(it)}, \mathbf{F}^{(it)}\}$ and $\{\alpha_k^{(it+1)}, \mathbf{F}^{(it+1)}\}$ are feasible to (P3.2.2) in the it-th and $(it+1)$-th iterations, respectively. By denoting the objective value of (P3.2.2) as $f(\alpha_k, \mathbf{F})$, one achieves $f(\alpha_k^{(it+1)}, \mathbf{F}^{(it+1)}) \geq f(\alpha_k^{(it+1)}, \mathbf{F}^{(it)})$. Consequently, for given reflection coefficients, $\alpha_k^{(it+1)}$, solution $\mathbf{F}^{(it+1)}$ is suboptimal. Moreover, one has $f(\alpha_k^{(it+1)}, \mathbf{F}^{(it)}) \geq f(\alpha_k^{(it)}, \mathbf{F}^{(it)})$ which eventually leads to $f(\alpha_k^{(it+1)}, \mathbf{F}^{(it+1)}) \geq f(\alpha_k^{(it)}, \mathbf{F}^{(it)})$. Based on the initial point of each iteration being the starting point of the previous one, the algorithm continues running to achieve a better solution in each iteration, i.e., increasing the sum rate. On the other hand, the objective function increases in each iteration or remains unchanged until the convergence is satisfied. Thus, the proof is completed. □

Algorithm 3 Iterative AO for Sum Rate Maximization

Input: $it = 1$, tolerance $\epsilon > 0$, initial $\alpha_k^{(it)}$, $\mathbf{f}^{(it)}$, and $R_S^{(it)} = 0$.
Do ▷ Iteration
  Derive $\mathbf{g}_k^{*(it)}$ by (3.23).
  Run Algorithm 1 to derive $\mathbf{f}^{*(it)}$.
  Run Algorithm 2 to obtain $\alpha^{*(it)}$.
  Set $R_s^{(it)} = \sum_{k=1}^{K} R_k$.
  $it \leftarrow it + 1$;
While $|R_s^{(it)} - R_s^{(it-1)}| \geq \epsilon$ ▷ Termination
Return $\mathbf{g}_k^{*(it)}$, $\mathbf{f}^{*(it)}$ and $\alpha_k^{*(it)}$.

3.4.4 Low-complexity combiners

Algorithm 3 uses the AO approach with three subproblems described in the previous sections. Specifically, it optimizes the receive combiner at the reader by maximizing the SINR (subproblem (P3.3)), which leads to the MMSE filter (3.23). This is an iterative process where the MMSE filter depends on the outputs of the two other subproblems. The complexity of this process can be reduced if one of the subproblems can be eliminated. One option is to use less than sub-optimal solutions for $\mathbf{g}_k$, $\forall k \in \mathcal{K}$. To this end, note that various practical receivers widely use sub-optimal MF and ZF combiners. While these two offer low-complexity advantages, MF cannot remove the multiple-tag interference. Moreover, the ZF is vulnerable to noise and works well in only the high SNR regime. Nevertheless, they have sometimes been used for backscatter networks [26]. Accordingly, MF and ZF combiners can be expressed as

$$\begin{aligned} \mathbf{G}_{\text{MF}} &= \mathbf{H}_b, \\ \mathbf{G}_{\text{ZF}} &= \mathbf{H}_b \left(\mathbf{H}_b^H \mathbf{H}_b\right)^{-1}, \end{aligned} \tag{3.26}$$

where $\mathbf{H}_b \in \mathcal{C}^{N_r \times K}$denotes the channel backward matrix with the k-th column vector being $\mathbf{h}_{T_k}^b$. Note that these combiners depend only on CSI. In contrast, the MMSE filter (3.23) depends on the tag reflection coefficients and the precoder. Thus, using these combiners (3.26) will achieve lower sum rates than otherwise. However, that reduces the three-stage AO algorithm (Algorithm 3) into two stages, resulting in a roughly 4 times faster algorithm (based on our numerical experiments) .

3.4.5 Complexity Analysis

The complexity of the proposed algorithm can be assessed as follows. To compute $\mathbf{f}^{(it)}$ which is a standard SDP problem, the complexity is $C_1 = \mathcal{O}(I_1(2K(N_t^2) + N_t + N_r)^{4.5})$ where I_1 is the number of iterations for converge. Considering the matrix inversion and multiplication computational complexity, the complexity to compute the combiner vectors is $C_2 = \mathcal{O}\left(N_r^3 + N_r^2 + (K-1)\left(N_t^2 N_r + N_t N_r^2\right)\right)$. Also, the complexity of Algorithm 2 is $C_3 = \mathcal{O}(I_2 K^{3.5})$ [110] in which I_2 is the number of its iteration to converge to its optimal value. Finally, the overall computational complexity of Algorithm 3 is $\mathcal{O}\left(I_{it}(C_1 + C_2 + C_3)\right)$ where I_{it} is the required number of iterations for the outer algorithm to converge.

3.5 Numerical Results and Discussion

This section evaluates the performance of the proposed beamforming and reflection coefficients design. Comparisons are thus made between the sum rate of Algorithm 3 and that of the three following baselines.

B1) It is essential to observe the system performance if the EH constraint (3.8c) is relaxed. In this case, the resources allocated to ensure each tag's EH targets can be repurposed for sum-rate improvements. Thus, this baseline omits the EH constraint (3.8c) but otherwise runs Algorithm 3. With removing the EH constraints, each tag can reflect more, i.e., a higher reflection coefficient. This process will improve the total sum rate. This can be observed in Figure 3.9 and is discussed there. In summary, this baseline helps us to understand the trade-off between sum rate maximization and satisfying the EH constraint.

B2) The cost, complexity, and hardware limitations determine the maximum level of RSI suppression at the $\mathbf{R}$ via physical means. Algorithm 3, which was developed in this work, enables further suppression of the RSI via software-based signal processing techniques. However, algorithmic suppression of the RSI does not come without cost. The idea of this baseline is to get a sense of this cost. Thus, baseline 2 solves Algorithm 3, excluding the RSI constraint (3.8b). As (3.8c) and (3.8b) are strict constraints to be

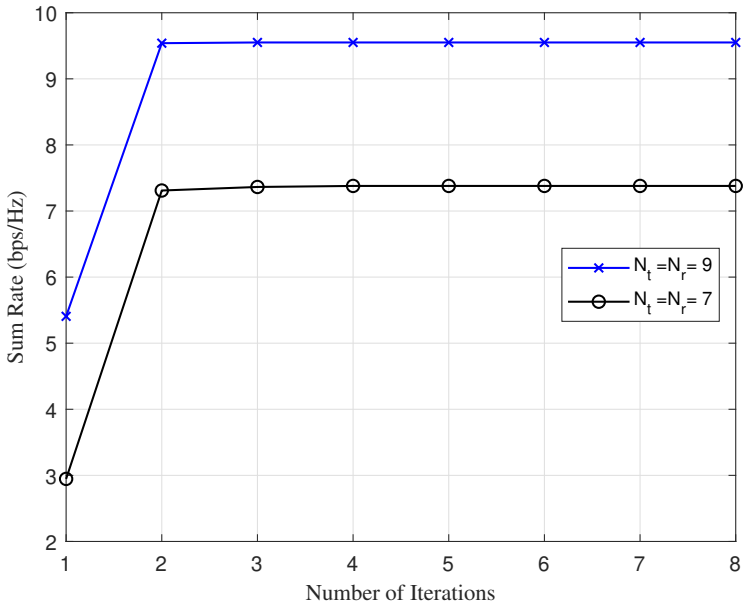

Figure 3.3: Convergence of Algorithm 3 for two antenna setups.

satisfied concurrently, removing (3.8b) reduces the complexity. This baseline reveals the sum rate penalty as a consequence of omitting the RSI suppression constraint.

B3) The tag's power reflection coefficient depends on the load impedance - see (1). Hence, optimizing the reflection coefficients helps choose proper impedances that result in a higher rate and range. However, to do so, $\mathbf{R}$ will require more computational resources. However, this may not be cost-effective for some low-cost applications. Therefore, this baseline aims to understand the impact of not optimizing the tag reflection coefficients. Thus, this baseline solves Algorithm 3 without EH constraint (3.8c) and uses random tag reflection coefficients. Although it reduces the complexity by not computing α_k (e.g., Algorithm 2), using non-optimized α_k penalizes the total sum rate.

Unless otherwise specified, the simulation parameters are set as follows: $K = 5$, $N_T = N_R = 7$, $P_T = 30$ dBm [48], $\sigma_n^2 = -120$ dBm, $\rho = 0$, $\epsilon = 10^{-3}$, $\eta = 0.4$ [90], $\beta = 10^{-9}$, $P_{\text{th}} = 1$ μw, $\lambda = -90$ dB, 100 m^2, and $\bar{K} = 0$ dB. The path-loss between the $\mathbf{R}$ and $\mathbf{T}_k$, $k \in \mathcal{K}$, is defined as $\xi_{T_k}^j = \left(\frac{3\times10^8}{4\mathsf{f}\pi}\right)^2 d_k^{-\varrho}$, where $j \in \{f, b\}$, $\mathsf{f} = 915$ MHz [48] is the carrier frequency, $\varrho = 2$ is the path-loss exponent, and d_k is the distance from the $\mathbf{R}$ to $\mathbf{T}_k$, $k \in \mathcal{K}$. Each simulation point is averaged over 10^3 Monte Carlo iterations.

3.5.1 Convergence Rates

The convergence behavior of **Algorithm 3** is studied first. After several iterations, it outputs the precoder, combiner vectors, and the reflection coefficients for different antenna configurations at the **R**. The stable sum rate at the end of several iterations illustrates the convergence behavior. Figure 3.3 is plotted for the achieved sum rate versus the number of iterations. The sum rate increases each iteration and converges to a fixed value after approximately three iterations. This fact suggests a fast convergence and validates the effectiveness of the proposed algorithm. Three iterations are approximately sufficient for both antenna configurations to reach good performance. Therefore, more than three iterations lead to minor performance enhancements.

3.5.2 Sum Rate versus Number of Tags

The impact of the number of tags, K, on the sum rate is depicted in Figure 3.4. To separate tag data spatially using the linear decoding vectors $\mathbf{g}_k$, the number of antennas should exceed the number of tags. We thus set $N_t = N_r = K+2$ to provide more spatial DoF for parameter design and satisfy the EH and RSI constraints. The increased number of tags is expected to increase the sum rate for all schemes. The figure clearly shows this trend. However, as the MMSE filter can only partially remove the inter-tag interference, more tags may increase interference. Thus, the sum rate versus the number of tags does not increase monotonically. More specifically, Algorithm 3 outperforms baselines two and three for more than five tags.

This performance arises from the following reasons. First, baseline two removes the RSI constraint (3.8b). Thus, it runs the algorithm to maximize the sum rate without (3.8b). The RSI term in the sum rate expression depends on the precoder, which in turn depends on the energy constraint. As a result, the choice of precoder, which satisfies the energy constraint, may not suppress the RSI term. Therefore, having the distinct RSI suppression constraint along the energy constraint limits the RSI, which results in Algorithm 3 outperforming baseline 2. Second, baseline 3 does not optimize the tag reflection coefficients.

A substantial gap is observed between baseline 1 and the other two baselines, increasing with the number of tags. However, the gap between Algorithm 3 and baseline 1 is more

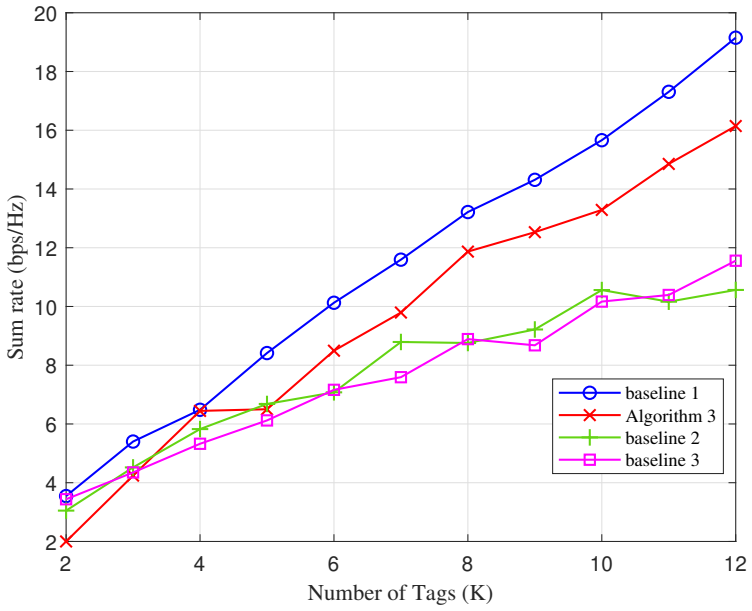

Figure 3.4: Sum rate versus the number of tags, K, with $N_t = N_r = K + 2$.

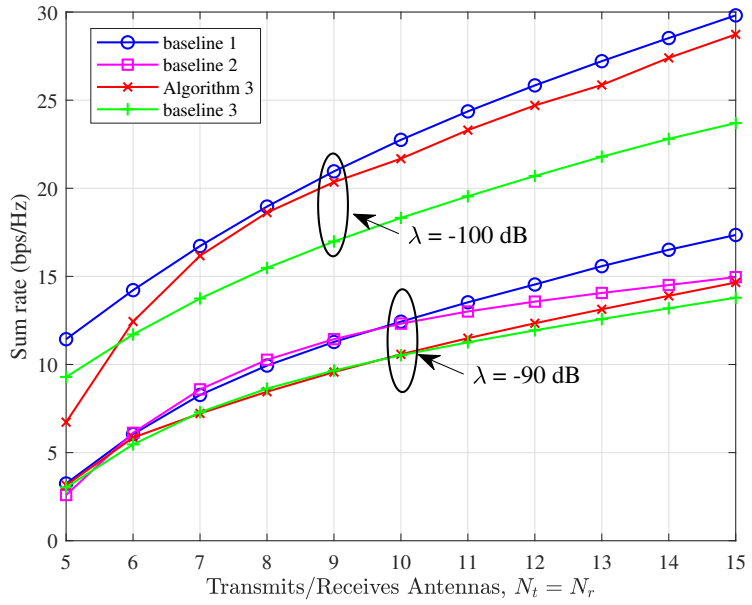

Figure 3.5: Sum rate versus the number of transmit/receive antennas.

or less constant. Hence, the proposed optimization yields substantial gains. Baseline 1, compared to Algorithm 3, is the price to pay for having longer lifetimes for tags (consistent with low power machine type communication target), which can harvest energy from the carrier itself. Also, it is possibly cheaper than achieving the same lifespan from an external power source. This fact shows the non-negligible impact of the RSI. Recall that tags are assumed to have enough power to perform their reflections in baseline 1 and thus do not perform EH. Therefore, this baseline releases some of the spatial DoFs that would have been utilized to ensure the tags meet the EH threshold for suppressing the effects of RSI. Thus, it suppresses the RSI effect more effectively and achieves a higher sum rate. However, when tags run on low power, replacing their batteries is not cost-effective and sometimes impossible (e.g., in toxic industrial regions). Therefore, EH from the **R** keeps the tag's operation. As a result, the proposed design can fairly compete and gain near results to the baseline one.

3.5.3 Sum Rate versus Number of Antennas

Here, the sum rate obtained by Algorithm 3 is compared against other baselines for the diverse number of transmit/receive antennas (N_t/N_r) and two different λ values. Referring to Figure 3.5, increasing the number of antennas at the **R** has a direct impact on the improvement of the sum rate as the system exploits the array gain in the downlink transmission and multiplexing gain in the uplink. This figure shows the superiority of our proposed design compared to the other baselines when RSI is strictly limited, say $\lambda = -100$ dB. Explicitly, as RSI's power is reduced more, better performance in terms of sum rate is achievable. Thus, Algorithm 3 with $\lambda = -100$ dB receives 96%, 21%, sum rate enhancement with $N_t = N_r = 15$ compared to the baseline 2 and baseline 3. However, it can be seen that for $\lambda = -90$ dB, the proposed design can only obtain better gain compared to baselines 2 and 3 for the number of antennas greater than 15. It confirms that Algorithm 3 excels other schemes for a higher number of antennas and lower RSI power.

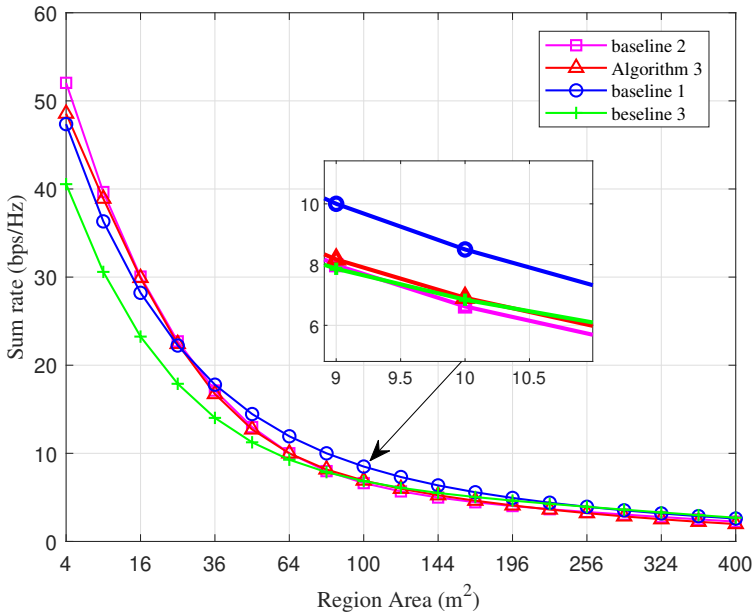

Figure 3.6: Sum rate versus region area, $r \times r$, for different baseline schemes.

3.5.4 Sum Rate versus Coverage Area

Figure 3.6 represents the impact of region area for different schemes on the sum rate. Note that as the coverage area increases, the sum rate decreases drastically. This decay arises because of the increased tags to **R** distances that exacerbate the double path-loss (dyadic channel). As the coverage area increases, there is a slight difference between the schemes. However, for a small area, specifically, 4 m^2 to 25 m^2, the proposed scheme and baseline 2 have a bit more gain than other baselines. Since their required power is better satisfied because of the strong forward links in short distances and they can reflect with their greater reflection. Baseline 1 slightly outperforms in the moderate coverage area, 36 m^2 to 144 m^2. Because, as the area increases, the distance of the tag from **R** also increases. Therefore, providing the required tag's power becomes more challenging while suppressing the RSI. Consequently, baseline 1 achieves more gain since the EH constraint is relaxed.

3.5.5 Sum Rate Versus Soft RSI Power Threshold

Figure 3.7 investigates the impact of the soft RSI power threshold, λ, on the sum rate for different schemes. Note that λ is the RSI threshold implemented in Algorithm 3. However,

β can be interpreted as a hardware-dependent SI threshold as it depends on the loss and impairments of the SI cancellation circuits at $\mathbf{R}$. Thus, the value of β is fixed beforehand. Whereas λ offers the on-the-fly control of the RSI as needed. As λ increases, the sum rate drastically decreases because the algorithm suppresses RSI to a lesser degree, which kills the sum rate. The proposed design works better than other benchmarks for smaller RSI thresholds. As λ gets smaller, our algorithm suppresses RSI more effectively, and hence, the impact of the RSI on the SINR becomes negligible. However, as the MMSE filter can partially remove the inter-tag interference, the amount of the reflected power from tags (α_k) becomes significant. Consequently, as seen in Figure 3.9, in baseline 1, most tags reach the high power reflection mode ($\alpha_k > 0.9$), which enhances the interference at the reader. Therefore, the proposed design performs slightly better than baseline 1 as the reflection power of the tags is controlled via EH. Furthermore, as the energy constraint is relaxed in baseline 1 (which releases more DoF for system optimization), it reaches a slightly better sum rate in higher λ. However, for a higher value of λ, all the schemes converge together and achieve a trivial sum rate. Besides, baseline 3 behavior highlights the importance of the optimized power reflection coefficient as it obtains a small sum rate compared to other schemes. This figure shows the importance of sufficient RSI suppression to gain a significant sum rate.

3.5.6 Sum Rate versus SNR

In Figure 3.8, the sum rate is depicted versus SNR defined as SNR $= \frac{P\bar{\xi}^i_{T_k}}{\sigma^2_R}$, where $\bar{\xi}^i_{T_k} = \frac{1}{K}\sum_{k=1}^{K}(\xi^i_{T_k})^2$ [48]. To justify the choice of the MMSE filter for the reader, we also plot the achieved SNR for Algorithm 3 with the ZF combiner and Algorithm 3 with the MF combiner. Algorithm 3 and baseline 2 perform roughly the same in the low SNR region. Because in this region, $\mathbf{R}$ transmits with low power, automatically reducing RSI and having a less harmful effect. However, as the SNR grows, the performance gap between Algorithm 3 and baseline 2 increases, and the former achieves a better sum rate. Although higher transmit power can increase the reflected power of tags, it also increases the RSI, causing a degradation of the sum rate. Baseline 1 has a slightly better output in low SNR than the two other schemes, and the gap increases in the high SNR region. This trend is clear since

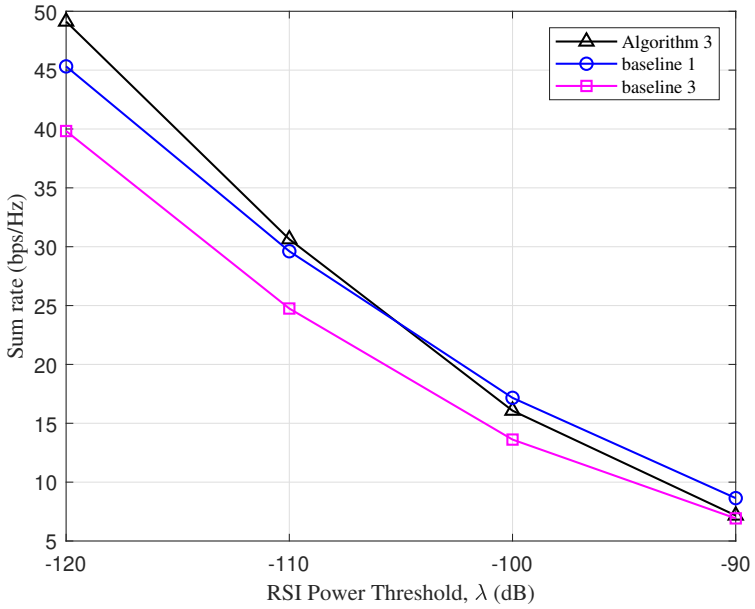

Figure 3.7: Sum rate versus RSI power threshold, λ.

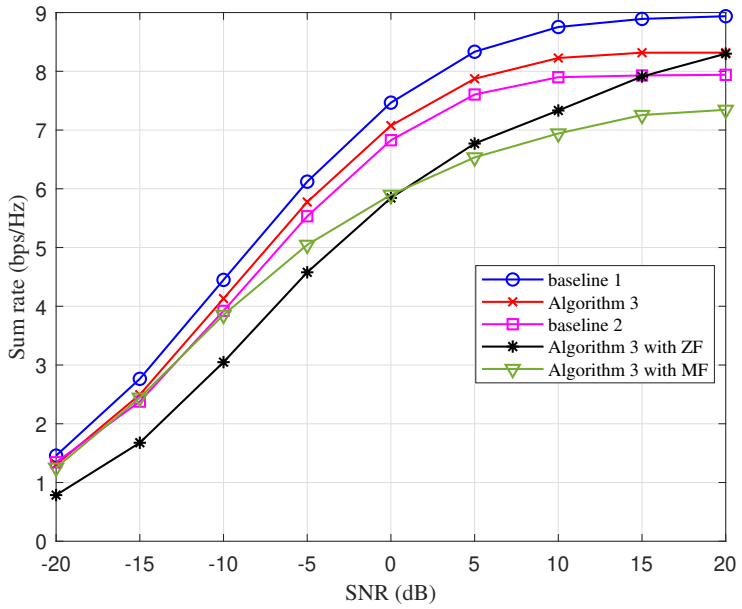

Figure 3.8: Sum rate versus SNR for different baseline schemes.

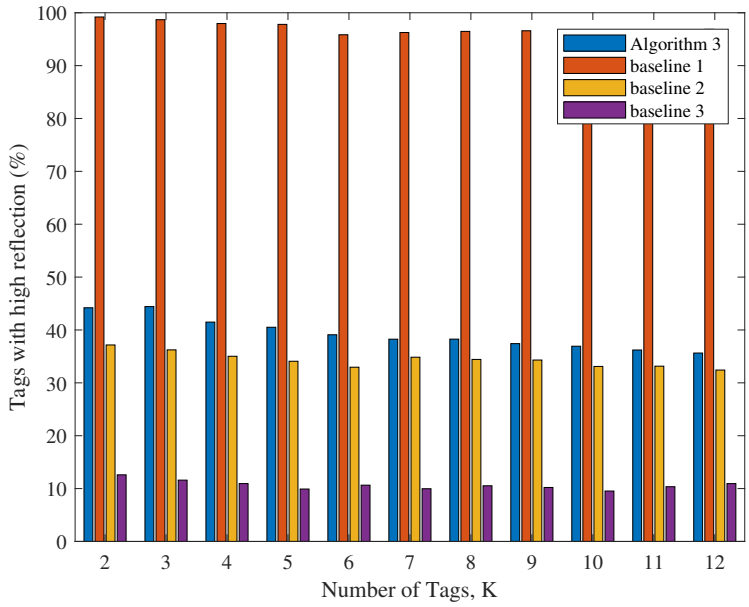

Figure 3.9: Tags with high reflection (%) versus the number of tags K.

satisfying power for each tag sets a more solid constraint on the system design. The ZF combiner performs poorly in the low SNR regime but outperforms Algorithm 3 for SNR$>$ 20 dB. The MF combiner outperforms the ZF in the low SNR regime. However, when SNR increases, it performs poorly than other baselines since the MF combiner cannot remove the intersymbol interference in tag data. Therefore, for a typical operating SNR regime ($\leq$ 20 dB), the choice of MMSE filter yields better performance.

3.5.7 Number of Tags with High Reflection

The number of tags achieving high reflection coefficients (values exceeding 0.9) can be counted to gain better insights into the proposed optimization. Figure 3.9 shows the percentage of tags meeting this criterion versus the total number of tags in the system. With Algorithm 3, approximately 35%-45% of tags operate in high reflection mode. This is because a significant portion of the received power at the tag is directed to the EH circuit to satisfy the minimum EH threshold. In baseline 1, the EH constraint is removed, allowing all tags to be in high reflection mode to maximize the sum rate. Consequently, rather than optimizing α_k, the reflection coefficients of all the tags can be set to the highest value, re-

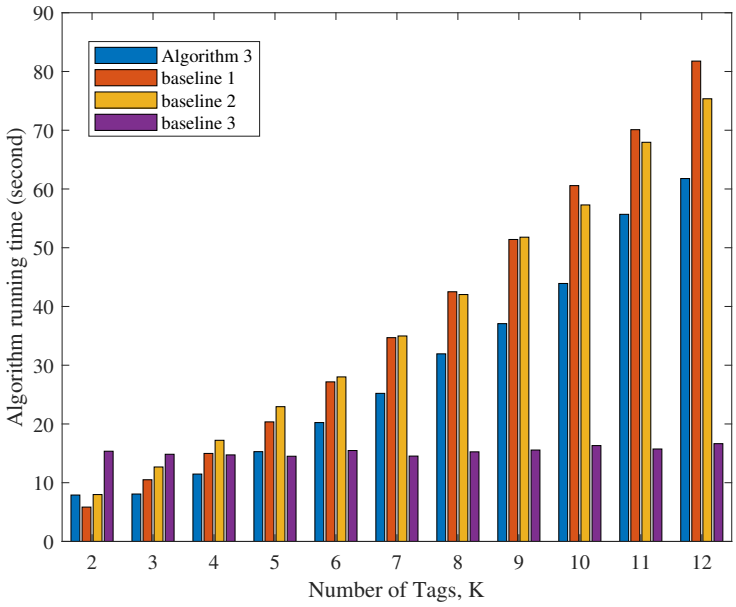

Figure 3.10: The running time versus the number of tags, K.

ducing the complexity and running time of baseline 1. The same trend as Algorithm 3 is observed in baseline 2. In baseline 3, since the reflection coefficients are selected randomly, approximately 10% of the tags operate in high reflection mode, resulting in a lower sum rate.

3.5.8 Software Running Time versus Number of Tags

Figure 3.10 represents the software running time cost versus the number of tags, K. It is the Matlab code runtime on a personal computer with Intel(R) Xeon(R) CPU at 3.5 GHz. The running time of all the schemes increases with more tags. However, interestingly, baseline 3 has a roughly fixed running time. Algorithm 3 is faster than baseline 2 and 3. The probable reason is the higher number of iterations for these baselines as K grows.

3.5.9 Imperfect CSI Knowledge

Suppose reader $\mathbf{R}$ has imperfect CSI, possibly due to CE errors. Let the channel estimate of the true channel $\mathbf{h}$ be $\hat{\mathbf{h}}$. Due to CE errors, the true channel and its estimate may thus be related as [117]: $\hat{\mathbf{h}} = \mathbf{h} + \mathbf{n}$, where $\mathbf{n} \in \mathbb{C}^{N\times 1}$ is an N-dimensional noise vector following $\mathcal{CN}(0, \sigma_n^2\mathbf{I})$, where $\sigma_n^2 = \rho\|\mathbf{h}\|^2$. Denote ρ as a ratio of the noise power to the channel gain

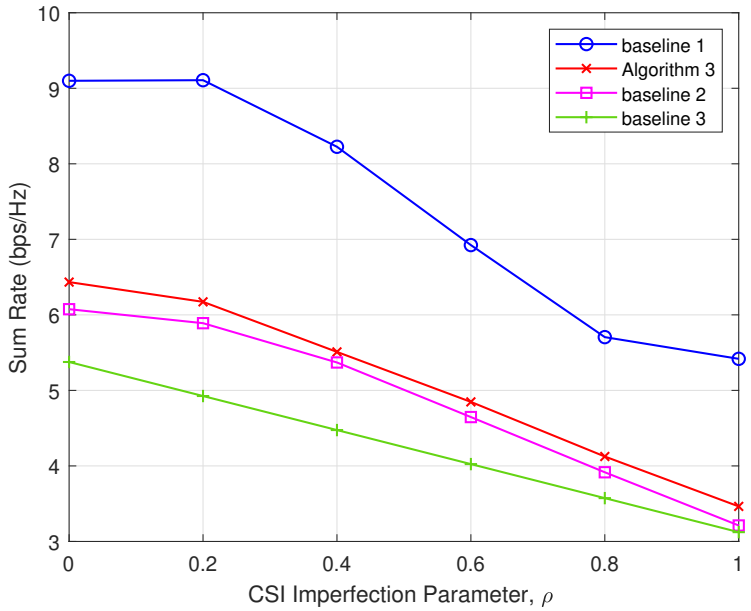

Figure 3.11: Sum rate versus CSI error parameter, ρ, for the different number of transmit/receive antennas.

representing the level of the CSI error. To get a better insight into CSI inaccuracy, Figure 3.11 represents the sum rate of the proposed scheme versus the CSI error parameter, ρ, for different baselines. Obviously, the performance of this system is highly impacted by the accuracy of CE. As ρ increases, the performance gap grows compared to the perfect CSI case ($\rho = 0$). For instance, the proposed scheme and baseline 1 decrease by about 46% and 40%, respectively, compared to the perfect CSI case. However, Algorithm 3 is more robust to CSI imperfections for a small range of ρ (i.e., $0 \leq \rho \leq 0.2$).

3.6 Conclusion

This chapter studied a multi-tag Monostatic BackComm network with a MIMO reader. Operating in FD mode, the reader's performance is significantly affected by RSI. This issue, not previously investigated, considers the imperfect nature of the reader's SI cancellation process represented by $\beta > 0$, whereas previous works assume $\beta = 0$. For finite $\beta > 0$, an algorithm was developed to limit the impact of RSI and enable the tags to harvest sufficient energy. The algorithm maximizes the sum rate by jointly optimizing the precoder, combiners,

and reflection coefficients, solving the resulting non-convex optimization problem via the AO approach. The algorithm was compared against several benchmarks and evaluated for robustness against imperfect CSI.

Several future extensions are possible. First, the achieved sum rate was susceptible to CSI accuracy, indicating that developing accurate CE techniques could be beneficial. Second, the reader used spatial DoFs to separate different tag signals, akin to SDMA. Investigating NOMA could improve the tags' overall sum rate and EH performance. Third, exploring multiple-antenna tags could enhance the data rate and increase the communication range. Finally, this study focused on uncoded backscatter links; the unitary query signaling approach [24, 97] could improve space-time codes for backscatter links, and its ability to mitigate RSI warrants investigation.

Chapter 4

IRS-Enabled Backscattering in a Downlink Non-Orthogonal Multiple Access System

This chapter examines a spectrum-sharing system that integrates BackComm with an IRS in a downlink NOMA system. The core concept is to leverage IRS transmit diversity for enhanced backscattering. To manage interference between the two systems, the AP splits its transmit signal into modulated and unmodulated components, transmitting two spectrally distinct streams that support both systems while controlling interference. The system is designed to maximize the primary system's rate while meeting the minimum requirements of the BackComm system. To address this non-convex problem, the AO algorithm, SDR, and a penalty-based approach are employed.

4.1 Introduction

Spectrum-sharing backscatter communications have been suggested as a potential remedy for the problems of spectrum scarcity and power limitation in IoT networks [118, 119]. A secondary BackComm and primary systems can coexist and share the spectrum. Moreover, IRS provides a large set of spatial degrees of freedom, which can be exploited to enhance the performance of backscattering tags.

Consequently, different primary and secondary configurations can be studied. However, this chapter studies a spectrum-sharing system, with two downlink NOMA users as a primary system and the IRS-enabled backscattering as a secondary system (Figure 4.1). The IRS is not only capable of backscattering its own data (secondary data) that can come from embedded sensors but also passively reflects the AP signals (primary data) to help the primary network [120,121]. In this concept, the IRS is embedded with environmental sensors and has its own data to transmit in addition to passively reflecting signals for ongoing links. This idea is new in two ways: 1) the IRS can backscatter its data using the downlink signal, and 2) it can simultaneously help the primary system. But how does the IRS modulate its data onto the AP signal and ensure that the IRS-data signal does not interfere with the decoding processes at two downlink NOMA users U_1 and U_2?

This chapter addresses these issues using the PS technique developed in [119,120]. Specifically, if the AP simultaneously transmits an unmodulated carrier and modulated carrier, then the IRS can backscatter its own data using the unmodulated part and reflect the AP signals too [120]. Thus, the AP splits its transmit power between these two carriers according to the PS ratio α (where $0 \leq \alpha \leq 1$). The modulated carrier transports the AP data for U_1 and U_2, and the unmodulated carrier is modulated by the IRS to send its own data, which is broadcast to both users. Since the rate of IRS data is much lower than that of the primary system, simple filtering can help U_1 and U_2 to decode the IRS data first and subtract it to avoid interference in decoding data. Then, when U_1 is decoding its data, the data of U_2 acts as interference. Thus, NOMA is leveraged to differentiate between U_1 and U_2. Specifically, NOMA can do that by exploiting the channel gain disparities (see [122] and references therein) and successive interference cancellation (SIC) decoding methods. IRS and NOMA together can boost the capacity, coverage, spectral efficiency, and other QoS metrics [123]. The process also supports data transmissions without requiring perfect symbol synchronization [119], which is important for low-complexity and low-cost IoT devices.

Previously, [119] was the first work that proposed splitting the AP signal into unmodulated and modulated carrier signals. Using this modified AP signal, [120] developed the concept of the IRS-enabled backscattering. However, these works [119, 120] differ from our study in several ways. The focus of [119] is to develop a cognitive BackComm system and an

associated cooperative receiver. Thus, the user can decode both the AP data and backscattered data successfully. Neither an IRS nor NOMA is considered in this work. It is limited to a single backscatter device. The focus of [120] is to enlist an IRS to send additional secondary data. The conceptual novelty of our study compared to [119, 120] is the integration of downlink NOMA with IRS-enabled backscattering.

Our study in this Chapter also differs from existing works [42,124], where the IRS assists in backscattering the AP signals. Further, our work differs from [125], where two NOMA users can receive a version of the BS signal reflected from a backscatter device. Also, in [122], authors use the IRS to assist the downlink NOMA users. However, the problem is non-convex, and widely available convex optimization techniques do not help.

In this chapter, the system depicted in Figure 4.1 is fully optimized. To achieve this, the PS factor, NOMA power coefficients, and IRS phase shifts are jointly optimized to maximize the rate of the stronger user. The problem is formulated by considering the decoding order of the users and guaranteeing QoS for both primary and secondary systems. The AO method is utilized as the optimization problem is non-convex. This method is an iterative procedure for maximizing a function jointly over all variables by alternatively maximizing over individual subsets of them. Therefore, the variables are split into three subsets: the PS factor, NOMA power coefficients, and IRS phase shifts. Closed-form solutions for the PS factor and NOMA power coefficients are derived for the first and second subproblems. SDR and penalty techniques are used to optimize phase shifts, subject to their unit-modulus constraints. These three tasks are combined into an overall algorithm (**Algorithm 4**) and compared to several baseline schemes, including one with orthogonal multiple access (OMA).

4.2 System Model

Figure 4.1 depicts the considered IRS-aided NOMA Ambient BackComm consists of a single-antenna AP operating based on the NOMA scheme, an M-passive reflecting elements IRS indexed by $m \in \mathcal{M} = \{1, \ldots, M\}$, and two single-antenna users in the set of $\mathcal{K} = \{1, 2\}$. There is no direct link between the AP and users due to high attenuation and signal blockages, a typical scenario [124, 126, 127]. This assumption holds for urban environments and

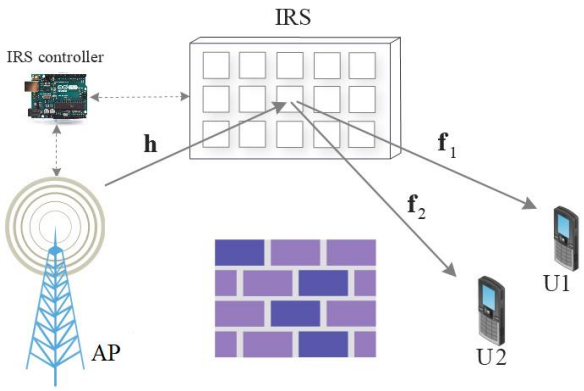

Figure 4.1: IRS-aided NOMA BackComm system model.

above-6 GHz frequency bands, such as millimeter waves, where signal blockages are frequent. In Figure 4.1, the IRS is also backscattering its sensed data. As mentioned, the AP simultaneously transmits modulated and unmodulated carriers and divides its power between these two parts. Therefore, the AP baseband transmit signal at time instant n can be represented as

$$x(n) = \sqrt{(1-\alpha)\,P_{\mathrm{T}}} + \sqrt{\alpha P_{\mathrm{T}}} \sum_{k=1}^{2} a_k s_k(n), \tag{4.1}$$

where α is the PS factor for the AP, P_{T} denotes the AP transmit power, s_k is the k-th user data that satisfies $\mathbb{E}\left[|s_k(n)|^2\right] = 1, k \in \mathcal{K}$, and a_k is the NOMA power allocation coefficient of the k-th user. To ensure fairness, the user with a lower channel gain gets assigned a higher a_k. The spectrum of the AP RF signal consists of a wideband message signal and an unmodulated carrier signal [120]. Upon receiving the RF signal, the IRS can modulate the unmodulated part, e.g., $\sqrt{(1-\alpha)P_T}e^{jw_c t}$, to send its own data usingbinary phase-shift keying (BPSK) modulation [120].

Denote channels from the AP-to-IRS and IRS-to-user k as $\mathbf{h} \in \mathcal{C}^{1\times M}$ and $\mathbf{f}_k \in \mathcal{C}^{M\times 1}$, $\forall k \in \mathcal{K}$, respectively. All the channels undergo quasi-static flat Rician fading and remain unchanged for several symbols [128] CSI availability is assumed. The Rician model applies to environments where the direct LoS component dominates over scattered paths, such as in open areas or with well-aligned antenna systems. It encompasses the Rayleigh model as a special case when the LoS component is absent or negligible. However, the primary difficulty is that, in practice, the required pilot/training overhead for channel estimation becomes unreasonably expensive due to the fact that the IRS often consists of a significant number of

reflecting elements. Grouping nearby IRS components into a subsurface—a process known as IRS element grouping—reduces the overhead associated with channel estimation by requiring the estimation of only the effective cascaded AP-IRS-Users channel for each subsurface [129]. These are standard assumptions in the literature. This system setup has the added advantage of easy synchronization because the time delay can be compensated through the passive reflecting elements at the IRS [120, 121]. Let $\mathbf{\Theta} = \text{diag}\left(\beta_1 e^{j\theta_1}, \ldots, \beta_m e^{j\theta_m}, \ldots, \beta_M e^{j\theta_M}\right)$ represents the reflection coefficient matrix at the IRS, where $\beta_m \in [0, 1]$ and $\theta_m \in [0, 2\pi)$, $\forall m \in \mathcal{M}$, are the reflection amplitude and phase shift of the m-th passive reflecting element at the IRS, respectively. To maximize the reflected signal power at the IRS and mitigate hardware costs, let $\beta_m = 1, \forall m \in \mathcal{M}$. Consequently, the received signal at each user can be written as

$$y_k(n) = \mathbf{h}\mathbf{\Theta}\mathbf{f}_k x(n) + z_k(n), \ \forall k \in \mathcal{K}, \tag{4.2}$$

where $z_k \sim \mathcal{CM}(0, \sigma^2)$, $\forall k \in \mathcal{K}$, is the received noise with variance σ^2, and it is assumed to be the same for all users.

4.3 Transmission Scheme

This works as follows. First, the AP transmits $x(n)$ with the symbol period T_s. Second, the IRS manipulates the unmodulated part of $x(n)$ to transmit its data, $b(n)$, by applying BPSK modulation with bit period $T_b \gg T_s$. For $b(n) = 1$ or 0, the IRS adds the following phase shifts: 0 or π. As a result, each user sees the original signal when $b(n) = 1$ and a negative of it when $b(n) = 0$. Since the primary system rate is much higher than the IRS data rate ($T_b = LT_s$, where $L \gg 1$), each user can decode the IRS data with a simple band-pass filter as each IRS data bit remains constant over LT_s duration. Accordingly, each user first decodes the IRS data, cancels the effect of the IRS data, and decodes its own data. The IRS data symbol is L times longer than the nominal user data symbol. Because each user must decode the IRS data symbol first before decoding its own data, this process will introduce a

delay of L bits. Thus, the received SNR of the secondary signal at each user is given by

$$\Gamma_{c_k} = \frac{L(1-\alpha)P_{\mathrm{T}}|\mathbf{h}\boldsymbol{\Theta}\mathbf{f}_k|^2}{\sigma^2},\ \forall k \in \mathcal{K}. \tag{4.3}$$

Consider $\Phi(k) \in \{0,1\}$ as the decoding order of user k, where $\Phi(k) = 1$ and $\Phi(\bar{k}) = 0$, $\forall k,\ \bar{k} \in \mathcal{K}$ indicate that the signal of user $\bar{k}$ is first decoded by treating user k's signal as interference. Then, by removing user $\bar{k}$'s signal via SIC, user k decodes its signal without the co-channel interference. Explicitly, it means that $|\mathbf{h}\boldsymbol{\Theta}\mathbf{f}_k|^2 \geq |\mathbf{h}\boldsymbol{\Theta}\mathbf{f}_{\bar{k}}|^2$. On the other hand, for $\Phi(k) = 0$ and $\Phi(\bar{k}) = 1$, one has $|\mathbf{h}\boldsymbol{\Theta}\mathbf{f}_{\bar{k}}|^2 \geq |\mathbf{h}\boldsymbol{\Theta}\mathbf{f}_k|^2$. Accordingly, the required SINR of user k can then be represented as

$$\Gamma_k = \frac{\alpha P_{\mathrm{T}} a_k |\mathbf{h}\boldsymbol{\Theta}\mathbf{f}_k|^2}{\Phi(\bar{k})\alpha P_{\mathrm{T}} a_{\bar{k}} |\mathbf{h}\boldsymbol{\Theta}\mathbf{f}_k|^2 + \sigma^2},\ \forall k, \bar{k} \in \mathcal{K}. \tag{4.4}$$

Subsequently, the rate achieved at user $k \in \mathcal{K}$ based on the Shannon capacity can be expressed as $R_k = \log(1 + \Gamma_k)$.

4.4 Problem formulation

The objective is to maximize the rate of the strong user while providing the QoS required for the weak user to decode its data. To achieve this, $\boldsymbol{\Theta}$, α, and a_k, $k \in \mathcal{K}$, are jointly designed, considering the decoding order. Let $\Phi(k)$ be an indicator function of the stronger user (i.e., the one with a larger channel gain). Specifically, if $\Phi(k) = 1$ and $\Phi(\bar{k}) = 0$, then user k is

the stronger user. The optimization problem is formulated as follows:

$$(\text{P4.1}): \max_{\boldsymbol{\Theta}, a_k, \alpha} \quad R_k = \log_2(1+\Gamma_k), \tag{4.5a}$$

$$\text{s.t.} \quad |\mathbf{h}\boldsymbol{\Theta}\mathbf{f}_k|^2 \geq |\mathbf{h}\boldsymbol{\Theta}\mathbf{f}_{\bar{k}}|^2, \text{ for } \Phi(k)=1, \Phi(\bar{k})=0, \tag{4.5b}$$

$$\Gamma_{\bar{k}} \geq \gamma_{\text{th}} \text{ for } \Phi(k)=1, \tag{4.5c}$$

$$\Gamma_{c_k} \geq \gamma_{\text{th}}, \ \forall k \in \mathcal{K}, \tag{4.5d}$$

$$|e^{j\theta_m}| \leq 1, \ \forall m \in \mathcal{M}, \tag{4.5e}$$

$$0 \leq \alpha \leq 1, \tag{4.5f}$$

$$a_1 + a_2 = 1, \tag{4.5g}$$

where (4.5b) indicates the decoding order at the NOMA users, and (4.5c) as well as (4.5d) are the QoS constraints that indicate the minimum SINR requirement of the weak user of the primary system and secondary system, respectively. (4.5e) denotes the unit-modulus constraints of the phase shifts at the IRS. Finally, (4.5f) and (4.5g) are the natural limits for α and a_k. The objective of this problem is non-concave, and constraints (4.5c) and (4.5d) are not convex. As a result, due to these factors and the coupling of optimization variables, P4.1 is non-convex.

4.4.1 Proposed Solution

The AO method is employed to solve (P4.1) efficiently. The AO paradigm is a widely used approach for tackling non-convex problems [123, 127, 128, 130]. An AO algorithm optimizes one block of variables at a time while keeping other blocks fixed. Following this paradigm, the problem is broken into three simpler sub-problems. Closed-form expressions for α and $a_k, \ \forall k \in \mathcal{K}$ are derived in the first and second subproblems, respectively. For $\boldsymbol{\Theta}$, SDR and penalty techniques are used by invoking SCA to optimize them.

Since the objective function in (P4.1) is a monotonically increasing $\log(\cdot)$ function and Γ_k for $\Phi(k)=1$ inside the $\log(\cdot)$ is a linear function of α, it is concluded that the objective is an increasing function over α. Thus, α achieves its optimum value in a corner of its feasible

regime. Based on (4.5d), the optimal value of α can be obtained as

$$\alpha_{\text{opt}} = \min\left(1 - \frac{\sigma^2\gamma_{\text{th}}}{LP_{\text{T}}|\mathbf{h}\boldsymbol{\Theta}\mathbf{f}_1|^2},\ 1 - \frac{\sigma^2\gamma_{\text{th}}}{LP_{\text{T}}|\mathbf{h}\boldsymbol{\Theta}\mathbf{f}_2|^2}\right). \tag{4.6}$$

However, to have a feasible regime for α, the following conditions also need to be satisfied:

$$\frac{\sigma^2\gamma_{\text{th}}}{a_2P_{\text{T}}|\mathbf{h}\boldsymbol{\Theta}\mathbf{f}_2|^2 - a_1P_{\text{T}}\gamma_{\text{th}}|\mathbf{h}\boldsymbol{\Theta}\mathbf{f}_2|^2} \leq \alpha_{\text{opt}}, \tag{4.7}$$

$$\frac{\sigma^2\gamma_{\text{th}}}{a_1P_{\text{T}}|\mathbf{h}\boldsymbol{\Theta}\mathbf{f}_1|^2 - a_2P_{\text{T}}\gamma_{\text{th}}|\mathbf{h}\boldsymbol{\Theta}\mathbf{f}_1|^2} \leq \alpha_{\text{opt}}, \tag{4.8}$$

if $|\mathbf{h}\boldsymbol{\Theta}\mathbf{f}_1|^2 \geq |\mathbf{h}\boldsymbol{\Theta}\mathbf{f}_2|^2$ and $|\mathbf{h}\boldsymbol{\Theta}\mathbf{f}_2|^2 \geq |\mathbf{h}\boldsymbol{\Theta}\mathbf{f}_1|^2$, respectively. Consequently, as a closed-form solution is derived for α, one can remove it from the optimization variables in (P4.1). However, the remaining optimization problem is still non-convex due to the multiplication of optimization variables, i.e., a_k and $\boldsymbol{\Theta}$ in the objective function and constraints. To overcome this via the AO approach, the NOMA power coefficients are optimized as shown below:

$$(\text{P4.2}): \max_{a_k}\ \log_2\left(1 + \frac{\alpha a_k P_{\text{T}}|\mathbf{h}\boldsymbol{\Theta}\mathbf{f}_k|^2}{\sigma^2}\right), \tag{4.9a}$$

$$\text{s.t.}\quad (4.5\text{c}),\ (4.5\text{g}). \tag{4.9b}$$

Upon replacing (4.5g) by (4.5c), one finds $a_k \leq (1+\gamma_{th})^{-1}\left[1 - \frac{\gamma_{th}\sigma^2}{\alpha P_T|\mathbf{h}\boldsymbol{\Theta}\mathbf{f}_{\bar{k}}|}\right]$. For the objective to be maximized, a_k must equal its upper bound:

$$a_k = (1+\gamma_{th})^{-1}\left[1 - \frac{\gamma_{th}\sigma^2}{\alpha P_T|\mathbf{h}\boldsymbol{\Theta}\mathbf{f}_{\bar{k}}|}\right],\ \forall k \in \mathcal{K}. \tag{4.10}$$

This indicates the allocation of power to the strong user. As a result, for the weak user, it

is $1-a_k$. Next, the optimization problem over $\mathbf{\Theta}$ can be rewritten as follows:

$$(\text{P4.3}): \max_{\mathbf{v}} \ \log_2\left(1+\frac{\alpha a_k P_{\mathrm{T}}|\mathbf{v}\mathbf{H}\mathbf{f}_k|^2}{\sigma^2}\right), \tag{4.11a}$$

$$\text{s.t.} \quad |\mathbf{v}\mathbf{H}\mathbf{f}_k|^2 \geq |\mathbf{v}\mathbf{H}\mathbf{f}_{\bar{k}}|^2, \ \text{for} \ \Phi(k)=1, \Phi(\bar{k})=0, \tag{4.11b}$$

$$\frac{\alpha a_{\bar{k}} P_{\mathrm{T}}|\mathbf{v}\mathbf{H}\mathbf{f}_{\bar{k}}|^2}{\Phi(k)\alpha a_k P_{\mathrm{T}}|\mathbf{v}\mathbf{H}\mathbf{f}_{\bar{k}}|^2+\sigma^2} \geq \gamma_{\mathrm{th}}, \ \text{for} \ \Phi(k)=1, \tag{4.11c}$$

$$\frac{L(1-\alpha)P_{\mathrm{T}}|\mathbf{v}\mathbf{H}\mathbf{f}_k|^2}{\sigma^2} \geq \gamma_{\mathrm{th}}, \ \forall k \in \mathcal{K}, \tag{4.11d}$$

$$|\mathbf{v}| = 1, \ \forall m \in \mathcal{M}, \tag{4.11e}$$

where $\mathbf{v} = \left[e^{j\theta_1}, \ldots, e^{j\theta_m}, \ldots, e^{j\theta_M}\right]$ and $\mathbf{H} = \mathrm{diag}\,(\mathbf{h})$. Nevertheless, (P4.3) is non-convex as it contains a quadratic form over $\mathbf{v}$. To address it, via the SDR technique, the non-convex problem is relaxed by defining a new variable as $\mathbf{V} = \mathbf{v}^H\mathbf{v}$ that satisfies $\mathrm{Rank}(\mathbf{V}) = 1$ and $\mathbf{V} \succeq \mathbf{0}$. Hence, the decoding order constraint at the users (4.5b) can be expressed as

$$\mathrm{Tr}(\mathbf{H}\mathbf{f}_k\mathbf{f}_k^H\mathbf{H}^H\mathbf{V}) \geq \mathrm{Tr}(\mathbf{H}\mathbf{f}_{\bar{k}}\mathbf{f}_{\bar{k}}^H\mathbf{H}^H\mathbf{V}), \ \text{for} \ \Phi(k)=1, \Phi(\bar{k})=0, \tag{4.12}$$

Finally, by dropping the non-convex rank-one constraint, (P4.3) can be reformulated as

$$(\text{P4.3.1}): \max_{\mathbf{V}} \ \log_2\left(1+\frac{\alpha a_k P_{\mathrm{T}}\mathrm{Tr}(\mathbf{H}\mathbf{f}_k\mathbf{f}_k^H\mathbf{H}^H\mathbf{V})}{\sigma^2}\right), \tag{4.13a}$$

$$\text{s.t.} \quad \frac{\alpha a_{\bar{k}} P_{\mathrm{T}}\mathrm{Tr}(\mathbf{H}\mathbf{f}_{\bar{k}}\mathbf{f}_{\bar{k}}^H\mathbf{H}^H\mathbf{V})}{\Phi(k)\alpha a_k P_{\mathrm{T}}\mathrm{Tr}(\mathbf{H}\mathbf{f}_{\bar{k}}\mathbf{f}_{\bar{k}}^H\mathbf{H}^H\mathbf{V})+\sigma^2} \geq \gamma_{\mathrm{th}}, \tag{4.13b}$$

$$\frac{L(1-\alpha)P_{\mathrm{T}}\mathrm{Tr}(\mathbf{H}\mathbf{f}_k\mathbf{f}_k^H\mathbf{H}^H\mathbf{V})}{\sigma^2} \geq \gamma_{\mathrm{th}}, \ \forall k, \tag{4.13c}$$

$$(4.12), \quad \mathrm{diag}(\mathbf{V}) = \mathbf{1}_M, \quad \mathbf{V} \succeq \mathbf{0}. \tag{4.13d}$$

However, (P4.3.1) usually results in a solution with a rank higher than one. A penalty term is thus defined for the rank-one constraint [130] to obtain a suboptimal solution. For the positive semidefinite matrix $\mathbf{Y} \in \mathbb{H}^{N\times N}$, the rank-one constraint can be expressed as the difference of two convex functions, i.e.,

$$\mathrm{Rank}(\mathbf{Y}) = 1 \Longleftrightarrow ||\mathbf{Y}||_* - ||\mathbf{Y}||_2 = 0, \tag{4.14}$$

where $||\mathbf{Y}||_* = \sum_j \delta_j$, $||\mathbf{Y}||_2 = \max_j\{\delta_j\}$, and δ_j is the j-th singular value of $\mathbf{Y}$. Consequently, the penalty-based approach is applied by integrating this constraint into the objective function of (P4.3.1), denoted by $F(\mathbf{V})$. This leads to the following optimization problem:

$$(\text{P4.3.2}) : \max_{\mathbf{V}} \quad F(\mathbf{V}) - \frac{1}{2\mu}(||\mathbf{V}||_* - ||\mathbf{V}||_2), \tag{4.15a}$$

$$\text{s.t.} \quad (4.12),\ (4.13b),\ (4.13c), \tag{4.15b}$$

$$\text{diag}(\mathbf{V}) = \mathbf{1}_M, \quad \mathbf{V} \succeq \mathbf{0}, \tag{4.15c}$$

Algorithm 4 Alternating Optimization Algorithm

1: **Input**: Initialize the number of iterations i, acceptable tolerance, $\epsilon \ll 1$, random phases, $\mathbf{\Theta}^{(i)}$, random NOMA power coefficients, $a_k^{(i)}$, and $R_k^{(i)} = 0$.
2: **repeat**
3: For given $\mathbf{\Theta} = \mathbf{\Theta}^{(i)}$ and $a_k^{(i)}$, calculate $\alpha_{\text{opt}}^{(i)}$ from (4.6).
4: Solve (4.10) to obtain $a_k^{(i+1)}$.
5: Solve (P4.3.2) to obtain $\mathbf{V}^{(i+1)}$ using Algorithm 1 in [128].
6: Decompose $\mathbf{V}^{(i+1)} = \mathbf{v}^{(i+1)}(\mathbf{v}^{(i+1)})^H$ and update
7: $\mathbf{\Theta}^{(i+1)} = \text{diag}(\mathbf{v}^{(i+1)})$.
8: Set $i = i + 1$;
9: **until** $|R_k^{(i)} - R_k^{(i-1)}| < \epsilon$.

where μ is a penalty factor for (4.14). Specifically, for a sufficiently small value of μ, solving (P4.3.2) yields a rank-one solution [130]. However, (P4.3.2) is still not a convex optimization problem yet due to the difference of concave functions form of the objective function. To address this, a lower bound is defined for $\Delta = ||\mathbf{V}||_2$ from its first-order Taylor series expansion, which is given by

$$\Delta(\mathbf{V}) \geq \Delta(\mathbf{V}^t) + \text{Tr}\Big(\nabla_{\mathbf{V}}^H \Delta(\mathbf{V}^t)(\mathbf{V} - \mathbf{V}^t)\Big) \triangleq \tilde{\Delta}(\mathbf{V}). \tag{4.16}$$

The transformed problem (P4.3.2) is a standard semi-definite programming (SDP) that can be solved efficiently by using CVX [131].

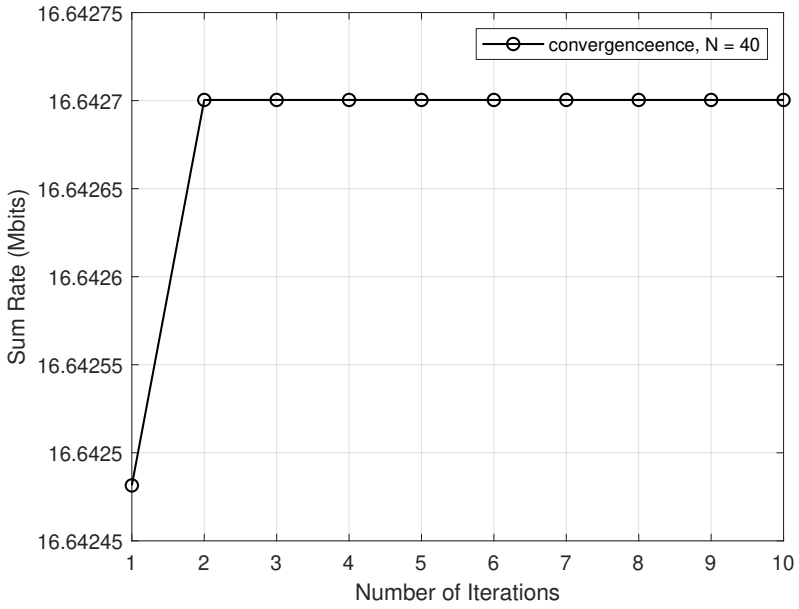

Figure 4.2: Convergence of the proposed algorithm for $M = 40$.

4.5 Performance evaluation

This section presents numerical results to evaluate the performance of **Algorithm 4**. The IRS comprises a two-dimensional uniform rectangular array of phase shifts. All users are randomly located in the $[2:20, 1:2]$ meters (m). The AP and IRS locations are considered as $(0, 0)$ m and $(2, 2)$ m, respectively. The Rician factor is set to 3 dB, $L = 10$, $\gamma_{\text{th}} = 10$ dB [120], $\sigma^2 = -110$ dBm, and $\mu = 5 \times 10^{-5}$ [130]. The average channel attenuation at a unit reference distance with $f = 915$ MHz is $(3 \times 10^8/4\pi f)^2 d^{-\xi}$, where d is the distance between nodes and $\xi = 2.1$ is the pathloss exponent [42]. For comparison, three benchmark system designs are studied, namely, i) Benchmark 1: **Algorithm 4** with random phase shifts, $\boldsymbol{\Theta}_{\text{rnd}}$; ii) Benchmark 2: **Algorithm 4** with OMA; iii) Benchmark 3: **Algorithm 4** with OMA and random phase shifts. These benchmarks allow us to discern the effect of not optimizing the phase shifts and not using NOMA. The OMA scheme is implemented as TDMA with equal transmission time to serve users. To maximize the SNR for each user, the optimal phase control policy can be achieved by aligning the phase of the IRS to match with the phase of the cascaded channels, i.e., $\mathbf{h}$ and $\mathbf{f}_k$.

Figure 4.2 illustrates the convergence of the proposed algorithm across iterations for a

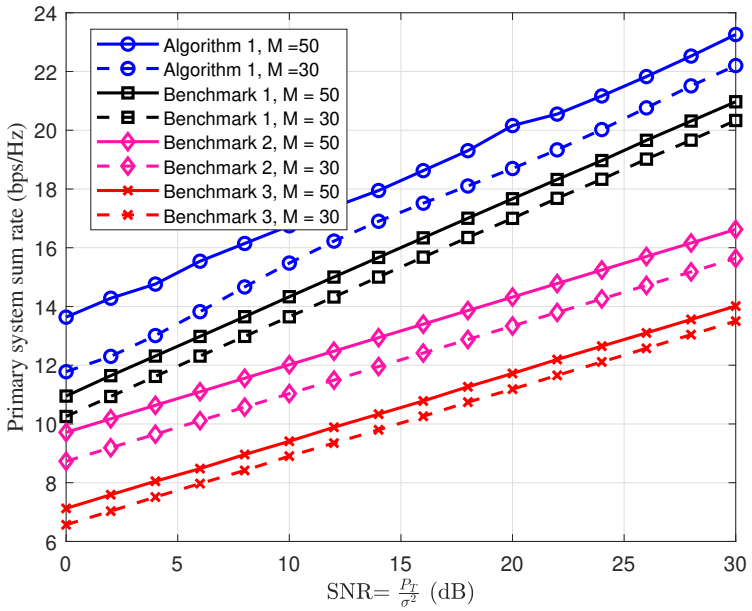

Figure 4.3: Primary system sum rate versus SNR.

constant number of reflectors at the IRS, M = 40. The graph clearly depicts the algorithm reaching its suboptimal point after just 2 iterations, highlighting the swift convergence of the proposed method. This observation underscores the efficiency and rapidity with which the algorithm approaches a satisfactory solution.

Figure 4.3 shows the impact of SNR $= \frac{P_T}{\sigma^2}$ (dB) on the sum rate of the primary system for two different numbers of phase shifts, M. The figure shows that **Algorithm 4** outperforms other schemes. The impact of the optimal phase shifts is essential for performance. However, Benchmark 1 also performs better than the OMA transmission scheme, indicating the effectiveness of NOMA even without optimized IRS phase shifts. Specifically, when $M = 30$, **Algorithm 4** improves the sum rate by 40% and 68% compared to Benchmark 2 and Benchmark 3, respectively. Furthermore, as the number of phase shifts increases, all the schemes achieve a higher sum rate. Indeed, the greater the number of phase shifts, the higher the number of multipath components, which improves the sum rate.

Figure 4.4 illustrates the impact of imperfect CSI and imperfect SIC on **Algorithm 4**. The channel estimation model is given as $\hat{\mathbf{h}} = \mathbf{h} + \mathbf{e}$, where $\mathbf{h}$ is the actual channel and $\mathbf{e}$ is the estimation error that is Gaussian distributed and zero mean, i.e., $\mathbf{e} \sim \mathcal{N}(0, \sigma_{\mathbf{e}}^2)$. Error variance satisfies $\sigma_{\mathbf{e}}^2 \triangleq \eta|\mathbf{h}|^2$, where η controls the level of CSI error. The right

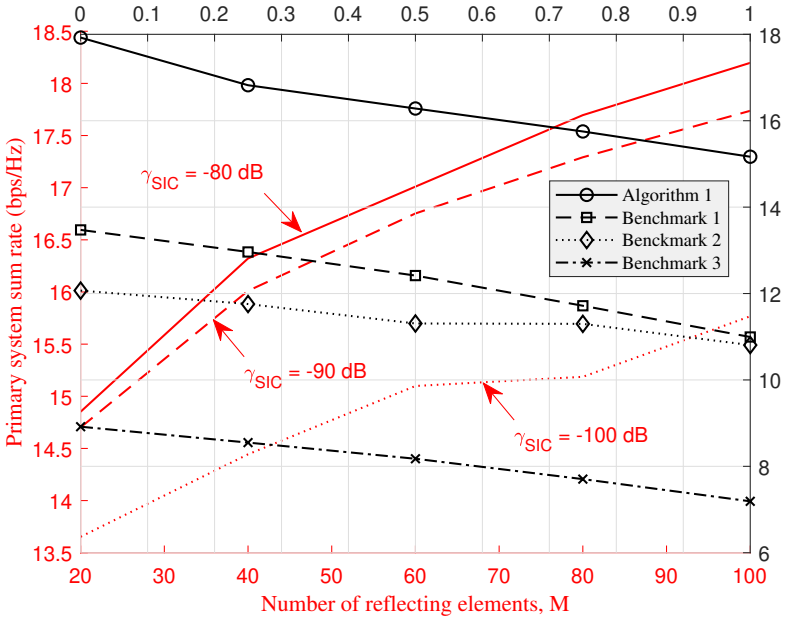

Figure 4.4: Primary sum rate versus M with $P_{\mathrm{T}} = 10$ dBm and CSI imperfection η .

figure shows the primary system sum rate versus the η. As the CSI error increases, the sum rate of all schemes decreases. For instance, the performance loss is %7.8 with $\eta = 0.5$ compared to the ideal CSI case (i.e., $\eta = 0$). Now, let us consider the impact of imperfect SIC. The strong user rate is then $\log_2\left(1 + \frac{a_k \alpha P_T |\mathbf{h}\boldsymbol{\Theta}\mathbf{f}_k|^2}{\beta a_{\tilde{k}} \alpha P_T |\mathbf{h}\boldsymbol{\Theta}\mathbf{f}_k|^2 + \sigma^2}\right)$, where $\beta \in [0, 1]$ denotes the SIC imperfection factor. For this simulation, $\beta = 0.1$. On the other hand, to control this destructive factor, the residual SIC term is replaced with a constant γ_{SIC}, satisfying the new constraint $\beta a_{\tilde{k}} \alpha P_T |\mathbf{h}\boldsymbol{\Theta}\mathbf{f}_k|^2 \leq \gamma_{SIC}$. As a result, the left figure shows the achieved sum rate versus M for different residual SIC thresholds. The rate is sacrificed as γ_{SIC} decreased because the phase shift needs to maximize the objective and satisfy the QoS while restricting the residual SIC.

Figure 4.5 shows the primary system sum rate versus x, where AP is at $(-x, 0)$. While keeping the location of the IRS and users fixed, x is increased. The resulting higher path loss decreases the primary sum rate. It is observed that optimizing $\boldsymbol{\Theta}$ in **Algorithm 4** yields a better sum rate compared to the random and the OMA cases. The gap between **Algorithm 4** with optimized and random $\boldsymbol{\Theta}$ is evident in both NOMA and OMA transmission. It highlights the spectrum efficiency advantage of NOMA with optimized phase shifts.

Although the eigenvalue decomposition or Gaussian randomization (GR) can be used

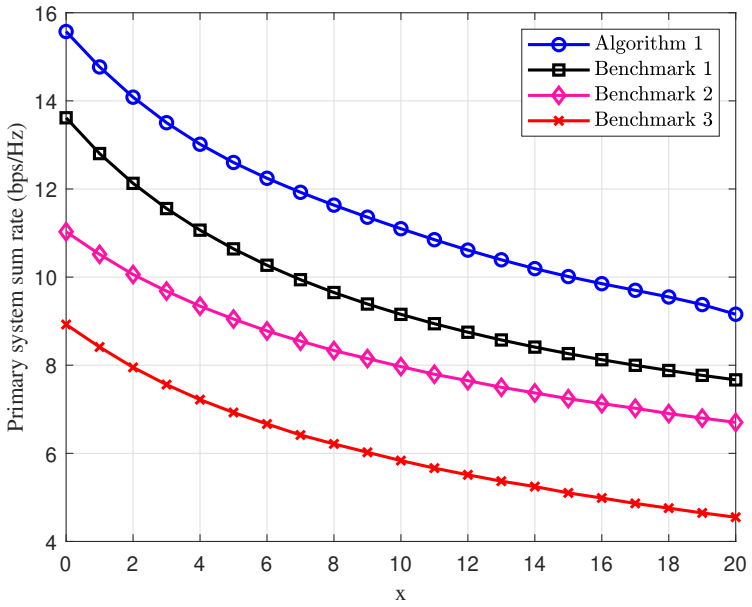

Figure 4.5: Primary sum rate versus x ($M = 30$ and $P_T = 10$ dBm).

to reconstruct the rank-one solution, the drawback is it uses a rank-one solution from the solution achieved by SDR, which may be infeasible for the original problem and may impose the performance loss. Therefore, the penalty factor is added to the objective for the rank-one constraint, which can be solved via SCA [132]. To validate the outperformance of the penalty-based rank-one solution, our proposed solution is compared with the one with GR in Figures 4.6, 4.7.

Figure 4.6 shows the primary sum rate versus the number of reflecting elements. Although Algorithm 1 with GR has a slightly better sum rate in small M, Algorithm 1 performs better as M increases. The reason is the GR is based on generating a large number of random Gaussian vectors, reconstructing the phase vector using it, and selecting one that maximizes the objective. However, this reconstructed phase shift matrix may not be feasible for the problem.

Furthermore, to quantify our proposed Algorithm's efficiency compared to GR, Figure 4.7 shows the running time of both approaches. As depicted, Algorithm 1 with GR has a higher running time since it reconstructs the phase shift matrix by generating many Gaussian random vectors and searching for the one that maximizes the objective.

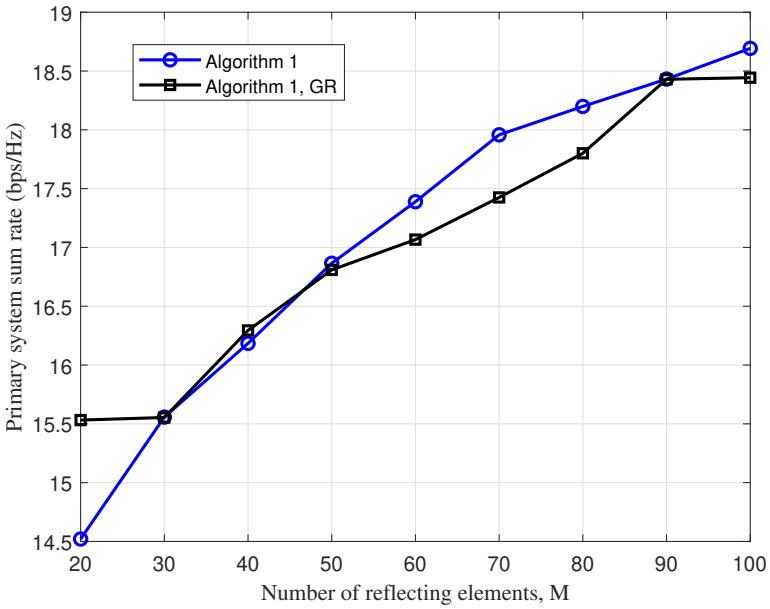

Figure 4.6: Primary sum rate versus M with $P_T = 10$ dBm.

4.6 Conclusion

To meet spectrum scarcity challenges, this chapter investigated a spectrum-sharing network consisting of two downlink users served by an AP as a primary system and an IRS backscattering as a secondary system. The IRS serves dual functions as a conventional relay while simultaneously backscattering its data. The AP splits its transmit power between modulated and unmodulated signal parts to enable this process and ease the detection at the receiver's side. The IRS uses the latter to convey its data to the NOMA users. The PS factor, IRS phase shifts, and NOMA power coefficients are optimized to maximize the rate of the strongest user in the primary while considering the decoding order at the users and satisfying QoS parameters for both weak user and IRS data of the primary and secondary systems, respectively. The simulation results demonstrate the outperformance of the proposed design compared to several defined benchmarks.

It is important to note that using IRS as a backscatter device can enhance signal quality and network coverage, but it also involves trade-offs related to complexity, cost, energy efficiency, and integration challenges. For instance, the system's overhead for channel training and CSI estimation increases because an IRS with many reflecting elements requires

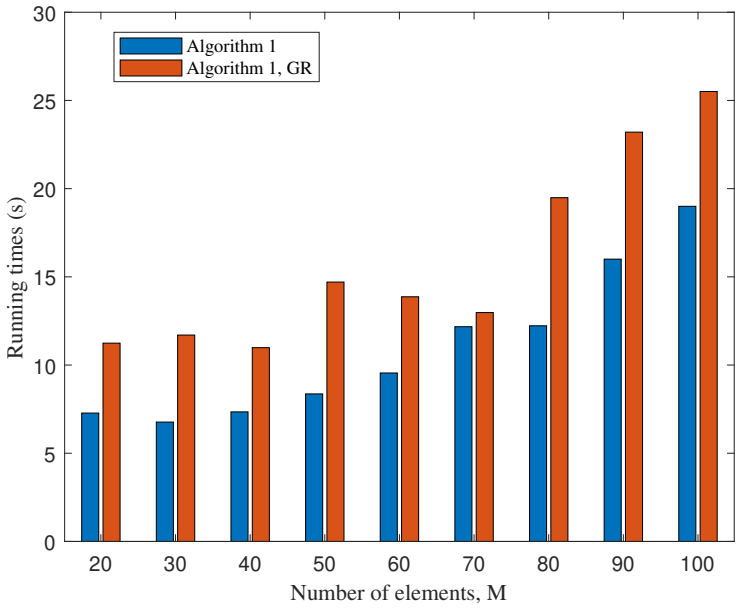

Figure 4.7: Running time versus the number of IRS elements.

more channel components to be estimated. Therefore, carefully balancing these trade-offs is essential for optimizing deployment and performance.

Chapter 5

Efficient Resource Management in Uplink Symbiotic and Cooperative Backscatter Networks

To address the challenges of deep dyadic fading in BackComm, this chapter explores an uplink transmission framework that integrates BackComm, SR, and cooperative communications. The key innovation lies in utilizing active nodes within the network to collaborate on the tag's data transmission, thereby mitigating the performance degradation caused by high attenuation in the backscatter link. The proposed transmission scheme operates in two phases. In the first phase, the designated BD reflects its data using the FD user equipment (UE) uplink signal to the BS. In the second phase, the UE supports the BD's transmission by sharing its power for the BD's data transmission. An algorithm to is developed maximize throughput while ensuring the QoS for the BD's throughput.

5.1 Introduction

The Rel 18 report of the Third Generation Partnership Project (3GPP) for advancing innovative cellular IoT technology has identified the need to explore passive IoT solutions and establish new standards. These standards should tackle emerging concerns, such as coexistence with UE and existing cellular technologies for spectrum-sharing [133]. Addressing these

concerns is critical due to the increasing strain on spectrum usage caused by the proliferation of connected devices. Thus, additional research is needed to handle network coexistence and cooperation in IoT networks, especially for BackComm.

However, to ensure seamless integration of wireless networks within an intelligent environment [134, 135], there is an anticipated increase in the deployment of BD equipped with sensors. For example, in a smart city, cellphone users (i.e., UE devices) navigate through urban landscapes. While the users walk, strategically positioned low-power sensors and intelligent devices (e.g., BDs) become attuned to the presence of UEs. These devices, ranging from smart streetlights and public benches to environmental sensors and security cameras, remain vigilant and poised to engage with their surroundings. Upon detecting a UE signal, they capitalize on the opportunity to initiate data transmissions. This evolving landscape necessitates the development of new techniques for effective cooperation and interaction between cellular users and these devices.

Therefore, BDs play a crucial role in real-time environmental monitoring across various sectors, including smart homes, smart cities, and manufacturing [136]. They transmit local environmental data to central nodes, typically AP, which aggregate this data at application servers for centralized processing. This facilitates comprehensive analysis and utilization for informed decision-making and resource management. Other applications include noise monitoring, pollution warnings, and traffic accident alert systems in smart cities to optimize energy, enhance security measures, and improve conveniences in smart homes [137]. Moreover, BDs enable advanced tracing and tracking functionalities, further enriching their utility.

However, despite being low-cost and low-power, BD's signal encounters bottlenecks, outlined as follows:

- Dyadic channel fading: As discussed in Chapters 1 and 2, the backscatter link suffers from dyadic channel effects due to its reliance on the forward link (RF source to BD) [3], leading to increased path loss, which curtails both range and data rate. Prior solutions include a hybrid approach combining active and passive transmission [138] or using either passive or active relays to mitigate dyadic fading.

- Interference-limited: Strong interference, such as an RF source signal, can easily dominate the weak backscattered signal. Therefore, the reliability and the decoding process are severely degraded. SIC, where interference is decoded and subtracted from the received signal, along with the widespread use of multi-antenna techniques, is a potential solution [3]. However, the SIC method increases complexity and suffers from error propagation problems. Another solution is to use multi-antenna systems to increase the SINR, thus enhancing the tag's signal detection [139].

To address these drawbacks, this Chapter utilizes the emerging concept of symbiotic radio (SR) where two networks share resources for mutual benefits [67, 118, 140–143]. The SR comprises a primary system and a secondary system, whereas the latter, in this case, is a BackCom system. The BD efficiently uses spectrum resources by superimposing its message onto the received signal from the primary system's transmitter and piggybacking its data on it. Thus, the BD envisions coexisting with an UE uplink transmission for sharing resources. In keeping with the futuristic outlook, the UE is assumed to be a FD wireless node [144]. In addition to SR, cooperative communication is employed, involving a cooperative receiver [67] and relaying the BD signal by the UE. Thus, this Chapter integrates both SR and cooperative communications.

5.1.1 Motivation and Contributions

Inspired by the above problem, but noting the need for symbiosis and cooperation from UE in the uplink to help the multi-BD system to improve its poor range and data rate, a novel two-phase cooperative uplink symbiotic BackComm system is presented here.

A1: Symbiotic phase - In this setup, each BD is allocated a time slot for the two-phase transmission while the remaining BDs remain inactive. In the first phase of each slot (i.e., symbiotic phase), the corresponding BD utilizes the uplink signal from FD UE to send its own data. The BS decodes the signals from the UE and BD via SIC methods. However, depending on the BD transmission rate, the BS may encounter different data rates for these uplink transmissions. If the BD symbol period is equal to the UE, there is no spectrum increase even when the BD transmission and primary transmission are

timed exactly. As this assumption is not too far from reality in the next generation with a high data rate, it serves as the case study for this work [145]. As a result, the backscatter link is parasitic for the primary system (uplink UE transmission).

A2: Cooperative phase - the uniqueness of this work stems from this phase. The UE integrates the decoded BD signal from the first phase into its own data stream during that time slot while assigning different transmit powers to each data stream to ensure that the BS can decode separately. This allows the UE to support and cooperate with the corresponding BD in each time slot. The BS utilizes SIC to decode the message the UE and BD superimposed.

The contributions of this chapter can be listed as follows:

- Unlike previous studies [140, 142, 143, 146, 147], this chapter proposes a cooperation scheme to enhance each BD performance. The FD-UE thus splits its power into two portions to integrate the previously decoded BD message into its signal. Such cooperation is beneficial for the BackComm system in two folds. First, the BD can use a more powerful active device like the UE for its transmission. Second, incorporating another node to assist with the BD reflection can improve its communication range and prevent the double-fading issue inherent in conventional Ambient BackComm.

- The UE throughput maximization problem is analyzed over all time slots while providing QoS for each BD's throughput. Our optimization variables include the combiner vector at the AP in both transmission phases, the power splitting factor at the UE in the second phase, and the time allocation for each transmission phase.

- The proposed optimization problem exhibits non-convexity, rendering traditional convex techniques ineffective. AO approach is applied to address this challenge, optimizing one variable at a time while keeping the others fixed. This method enables effective tackling of the problem and derivation of optimal solutions. Consequently, closed-form solutions for time allocation and power allocation variables in each time slot are derived. SDR and SCA techniques are applied during the first transmission phase to optimize the combiner vector. For the second transmission phase, optimization of the

combiner vector utilizes the maximum ratio combining (MRC) technique, a widely adopted method in wireless communication systems [148].

5.1.2 Literature Review

To our knowledge, this work is the first to introduce a novel concept of utilizing two transmission phases with UE cooperation in the uplink scenario. This specific scenario has not been investigated before. Nevertheless, an overview of related research studies is given next. In particular, [140] investigates the weighted sum rate of both the primary and the BD under both commensal (e.g., the symbol period for BD transmission is much greater than that of the primary one) and parasitic (e.g., the symbol period for BD transmission is equal to the primary system) setups. The authors propose a joint optimization scheme for the BD's reflection coefficient and the primary transmit power. In a similar vein, [143] focuses on the power minimization problem in a parasitic system by optimizing the primary transmit beamforming vector and the power-splitting factor at the BD. In [147], the authors investigate a multi-BD SR scenario in which BDs apply random code-assisted multiple access for their reflection. They first derive an asymptotic expression for the BD SINR. Then, by defining the optimization problem that maximizes the minimum SINR among BDs, they optimize the transmit power and reflection coefficients at the BDs. In another example, [67] considers both commensal and parasitic setups and defines two different optimization problems over transmit beamforming: weighted sum-rate maximization and the transmit power minimization problem. Furthermore, [23] proposes a FD SR system where the AP is both an RF transmitter and a receiver of multi-BDs. AP transmits an orthogonal frequency division multiplexing (OFDM) signal, while BD receives the signal through a NOMA dynamic-TDMA transmission scheme. The authors maximize the minimum throughput among all BDs while optimizing subcarrier power allocation, BDs' backscatter time allocation, and power reflection coefficients.

On the other side, performance analysis involves evaluating the quality and reliability to ensure optimal transmission and reception of data. Therefore, [142] investigates a symbiotic system of NOMA and Ambient BackComm. The BD leverages the NOMA signal from the base station to transmit data to the nearby NOMA user. The study derives expressions

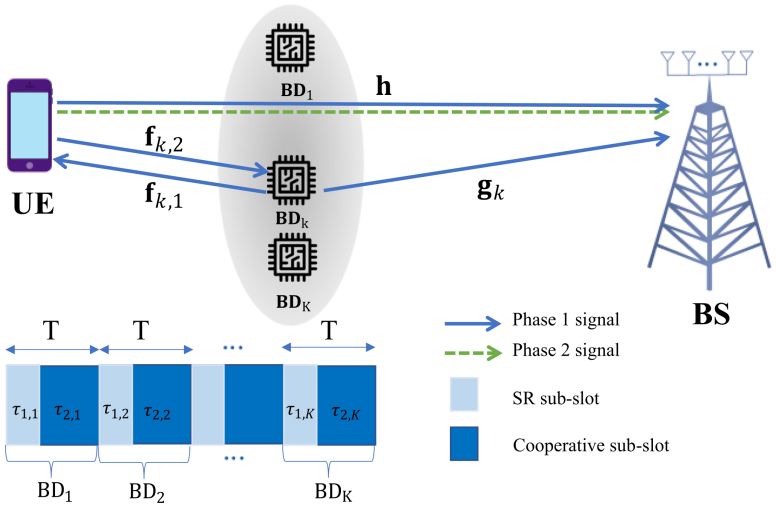

Figure 5.1: Cooperative symbiotic system model with two phases: (a) symbiotic phase $\tau_{1,k}$, (b) cooperative phase $\tau_{2,k}$.

for outage probabilities and ergodic rates and analyzes diversity orders. Similarly, [146] studies the performance of a downlink NOMA multiplexing-based SR where the channels are considered as Nakagami-m fading. The exact and asymptotic outage probabilities are determined using closed-form expressions. [149] analyzes the capacity in an SR system while keeping energy harvesting sensitivity at BD in mind.

5.2 System Model

The system model is depicted in Figure 5.1. It consists of a BS equipped with $M \geq 1$ antennas, $K \geq 1$ number of BDs where the k-th BD is denoted as BD_k, and a UE. Each BD and UE are equipped with two antennas, one each for receiving and transmitting (in the case of the BD and backscattering). The channel coefficients between the UE-BS, BD_k-BS, and the UE-BD_k transceiver are represented by $\mathbf{h} \in \mathbb{C}^{M\times 1}$, $\mathbf{g}_k \in \mathbb{C}^{M\times 1}$, and $f_{k,1}, f_{k,2} \in \mathbb{C}$, respectively, where $k \in \{1, \ldots, K\} \triangleq \mathcal{K}$. All the channels are assumed to undergo quasi-static flat-fading [63], and that CSI is available [67, 104, 140, 141, 143]. The transmission scheme for our system model consists of two phases, described as follows.

5.2.1 First phase (SR transmission):

The k-th time slot is assigned to the k-th BD. During the initial phase of each time slot ($\tau_{1,k}$ portion of T), the UE transmits its signal denoted as $s \sim \mathcal{CN}(0,1)$ [150]. This signal is also received by BD_k, which reflects $\sqrt{P_{\text{UE}}\alpha_k}sc_k$, where P_{UE} is the transmit power at the UE, $\alpha_k \in (0,1]$ is the reflection power coefficient at the BD_k, and c_k denotes the BD_k's data. Thus, the received uplink signal at the BS is given by

$$\mathbf{y}_{\text{BS},k}^{(1)} = \sqrt{P_{\text{UE}}}\mathbf{h}s + \sqrt{P_{\text{UE}}\alpha_k}f_{k,1}\mathbf{g}_k sc_k + \mathbf{z}_k^{(1)}, \tag{5.1}$$

where $\mathbf{z}_k^{(1)} \sim \mathcal{CN}(0, \sigma^2\mathbf{I}_M)$ denotes the additive white Gaussian noise (AWGN) in the SR phase of the k-th time slot at the BS. The BS implements a receiving beamforming vector, $\mathbf{w}_{s,k}, \mathbf{w}_{c,k} \in \mathbb{C}^{M\times 1}$, to decode the UE and BD_k signal in the SR phase, respectively. Thus, it performs SIC and decodes s first by treating the backscattered signal as interference. Then, the received SINR at the BS to decode s is given by

$$\gamma_{\text{UE},k}^{(1)} = \frac{P_{\text{UE}}|\mathbf{w}_{s,k}^H\mathbf{h}|^2}{\alpha_k P_{\text{UE}}|\mathbf{w}_{c,k}^H f_{k,1}\mathbf{g}_k|^2 + \sigma^2}, \ \forall k. \tag{5.2}$$

After subtracting s from the received signal, the SNR to decode c_k at BS can be expressed as

$$\gamma_{\text{BD}_k}^{(1)} = \frac{\alpha_k P_{\text{UE}}|\mathbf{w}_{c,k}^H f_{k,1}\mathbf{g}_k|^2}{\sigma^2}, \ \forall k. \tag{5.3}$$

In this work, the UE is envisioned as an FD node[1]. Therefore, in the SR phase of the k-th time slot, the UE also receives the reflected signal from BD_k and tries to decode it to cooperate in BD_k transmission in the cooperative phase. The received BD_k signal at the UE can be expressed as

$$y_{\text{UE},k}^{(1)} = \sqrt{\alpha_k P_{\text{UE}}}f_{k,1}f_{k,2}sc_k + w_k^{(1)}, \ \forall k, \tag{5.4}$$

[1]Self-interference (SI) is a fundamental impairment in FD nodes. However, various SI cancellation techniques are now available [151]. It is reasonable to assume that future realization of UEs will overcome SI bottlenecks.

where $w_k^{(1)} \sim \mathcal{CN}(0, \sigma^2)$ is the AWGN at the UE. The SNR for decoding c_k is given by

$$\gamma_{\mathrm{UE}\to\mathrm{BD}_k}^{(1)} = \frac{\alpha_k P_{\mathrm{UE}} |f_{k,1}|^2 |f_{k,2}|^2}{\sigma^2}, \ \forall k. \tag{5.5}$$

In the above two SNR expressions, dyadic fading terms appear.

5.2.2 Second phase (cooperative transmission):

In this phase of $\tau_{2,k}T$ duration, where $\tau_{2,k} = 1 - \tau_{1,k}$, the BD_k remains silent, and the UE cooperates by transmitting both its message and the BD_k message by splitting its power into two portions [152, 153]. The UE transmits a combined signal containing the user's and BD_k messages, given as $x_k = \sqrt{\beta_k P_{\mathrm{UE}}} s + \sqrt{(1-\beta_k) P_{\mathrm{UE}}} c_k, \ \forall k$, where $\beta_k \in (0, 1]$ is the PS factor at the UE. Then, the received signal at the BS can be represented as

$$\mathbf{y}_{\mathrm{BS},k}^{(2)} = (\sqrt{\beta_k P_{\mathrm{UE}}} s + \sqrt{(1-\beta_k) P_{\mathrm{UE}}} c_k)\mathbf{h} + \mathbf{z}_k^{(2)}, \tag{5.6}$$

where $\mathbf{z}_k^{(2)} \sim \mathcal{CN}(0, \sigma \mathbf{I}_M)$ is the AWGN at the BS in the second phase. Subsequently, the BS decodes the UE's and BD's signals using SIC. The required SINR and SNR for decoding s and c_k are given by

$$\gamma_{\mathrm{UE},k}^{(2)} = \frac{\beta_k P_{\mathrm{UE}} |\mathbf{w}_{2,k}^H \mathbf{h}|^2}{(1-\beta_k) P_{\mathrm{UE}} |\mathbf{w}_{2,k}^H \mathbf{h}|^2 + \sigma^2}, \ \forall k, \tag{5.7}$$

$$\gamma_{\mathrm{BD}_k}^{(2)} = \frac{(1-\beta_k) P_{\mathrm{UE}} |\mathbf{w}_{2,k}^H \mathbf{h}|^2}{\sigma^2}, \ \forall k, \tag{5.8}$$

respectively, where $\mathbf{w}_{2,k} \in \mathbb{C}^{M\times 1}$ is the receiving combiner vector at the BS in the cooperative phase of the k-th time slot. The proposed cooperative system follows the orthogonal relay channel model [154]. Thus, the sum throughput in both transmission phases can be expressed as [155, 156] :

$$R_{\mathrm{UE},k} = R_{\mathrm{UE},k}^{(1)} + R_{\mathrm{UE},k}^{(2)}, \ \forall k, \tag{5.9}$$

$$R_{\mathrm{BD}_k} = \min\left\{ R_{\mathrm{BD}_k}^{(1)} + R_{\mathrm{BD}_k}^{(2)}, R_{\mathrm{UE}\to\mathrm{BD}_k} \right\}, \ \forall k, \tag{5.10}$$

where $R^{(1)}_{\mathrm{UE},k} = \tau_{1,k}\log_2(1+\gamma^{(1)}_{\mathrm{UE},k})$, $R^{(2)}_{\mathrm{UE},k} = \tau_{2,k}\log_2(1+\gamma^{(2)}_{\mathrm{UE},k})$, $R^{(1)}_{\mathrm{BD}_k} = \tau_{1,k}\log_2(1+\gamma^{(1)}_{\mathrm{BD}_k})$, $R^{(2)}_{\mathrm{BD}_k} = \tau_{2,k}\log_2(1+\gamma^{(2)}_{\mathrm{BD}_k})$, and $R_{\mathrm{UE}\to\mathrm{BD}_k} = \tau_{1,k}\log_2(1+\gamma^{(1)}_{\mathrm{UE}\to\mathrm{BD}_k})$.

5.3 Optimization Problem

This section develops the framework to maximize the sum throughput of UE by jointly optimizing the PS/TS coefficients and receiving beamforming vectors. Since each node in this system operates within its designated time slot, the optimization problem can be formulated as maximizing throughput within each time slot as follows:

$$
\begin{aligned}
(\mathrm{P5}): \underset{\beta_k,\{\tau_{1,k},\tau_{2,k}\},\mathbf{w}}{\text{maximize}} \quad & R_{\mathrm{UE},k}, && \text{(5.11a)}\\
\text{s.t.} \quad & R_{\mathrm{BD}_k} \geq C_{\mathrm{th}},\ \forall k, && \text{(5.11b)}\\
& 0 \leq \beta_k \leq 1,\ \forall k, && \text{(5.11c)}\\
& \tau_{1,k} + \tau_{2,k} = T,\ \forall k, && \text{(5.11d)}\\
& 0 \leq \tau_{1,k} \leq T,\ \forall k, && \text{(5.11e)}\\
& 0 \leq \tau_{2,k} \leq T,\ \forall k, && \text{(5.11f)}\\
& \|\mathbf{w}_{l,k}\|^2 = \|\mathbf{w}_{2,k}\|^2 = 1,\ \forall k, l && \text{(5.11g)}
\end{aligned}
$$

where $\mathbf{w} = \{\mathbf{w}_{c,k}, \mathbf{w}_{s,k}, \mathbf{w}_{2,k}\}$ and $l \in \{c, s\}$. Constraint (5.11b) ensures the minimum rate at each BD. In addition, (5.11c), (5.11d)–(5.11f), and (5.11g) represent the inherent limits for the reflection coefficient, time allocation factor, and norm constraints for the beamforming vectors, respectively. It can be shown that (P5) is equivalent to the following optimization problem [155]:

$$
\begin{aligned}
(\mathrm{P5.1}): \underset{\beta_k,\{\tau_{1,k},\tau_{2,k}\},\mathbf{w}}{\text{maximize}} \quad & R_{\mathrm{UE},k}, && \text{(5.12a)}\\
\text{s.t.} \quad & R^{(1)}_{\mathrm{BD}_k} + R^{(2)}_{\mathrm{BD}_k} \geq C_{\mathrm{th}},\ \forall k, && \text{(5.12b)}\\
& R_{\mathrm{UE}\to\mathrm{BD}_k} \geq C_{\mathrm{th}},\ \forall k, && \text{(5.12c)}\\
& \text{(5.11c)} - \text{(5.11g)}, && \text{(5.12d)}
\end{aligned}
$$

in which (5.11b) is replaced by (5.12b) and (5.12c) in P5.1 [155].

This problem is non-convex because of the non-concave objective function and non-convex constraints in (5.12b) and (5.12c), making it challenging to find an optimal solution. To address this, we use the AO approach [63] to decompose the problem into three simpler sub-problems. In the first subproblem, $\mathbf{w}, \beta_k$ is fixed, and $\tau_{1,k}, \tau_{2,k}$ are optimized. In the second subproblem, β_k is optimized while keeping the other variables constant. Finally, the BS beamforming vectors are optimized in the third subproblem, with the other variables constant. This is done by employing the SDR approach. Optimal closed-form solutions are derived for the first and second sub-problems.

5.3.1 Optimizing over TS coefficient:

This subproblem focuses on optimizing the time allocation for each transmission phase. By isolating the variables and constraints relevant to this subproblem, the equivalent optimization can be rewritten as

$$(\text{P5.2}): \underset{\{\tau_{1,k},\tau_{2,k}\}}{\text{maximize}} \; R_{\text{UE},k}, \tag{5.13a}$$

$$\text{s.t.} \quad (5.12\text{b}) - (5.12\text{c}), \; (5.11\text{d}) - (5.11\text{f}). \tag{5.13b}$$

From (5.12c), one can find $\tau_{1,k} \geq C_{\text{th}}/\log_2(1+\gamma^{(1)}_{\text{UE}\to\text{BD}_k})$. Thus, $\tau^*_{1,k}$ can be expressed as $\tau^*_{1,k} = C_{\text{th}}/\log_2(1+\gamma^{(1)}_{\text{UE}\to\text{BD}_k})$. Then, by substituting $\tau^*_{1,k}$ in (5.12b), $\tau^*_{2,k}$ can be expressed as

$$\tau^*_{2,k} = \frac{C_{\text{th}} - \frac{C_{\text{th}}\mathcal{B}_K}{\mathcal{A}_k}}{\mathcal{D}_k}, \tag{5.14}$$

where $\mathcal{A}_k = R_{\text{UE}\to\text{BD}_k}$, $\mathcal{B}_k = R^{(1)}_{\text{BD}_k}$ and $\mathcal{D}_k = R^{(2)}_{\text{BD}_k}$. As both R_{BD_k} and $R_{\text{UE},k}$ in (5.9) and (5.10) exhibit an increase with respect to $\tau^*_{1,k}$ and$\tau^*_{1,k} + \tau^*_{2,k}$. By substituting $\tau^*_{1,k}$ and $\tau^*_{2,k}$ into (5.11d), each BD's throughput lower-bound can be represented as

$$C_{\text{th}} = \frac{T\mathcal{A}_k\mathcal{D}_k}{\mathcal{A}_k + \mathcal{D}_k - \mathcal{B}_k}. \tag{5.15}$$

This parameter is a lower bound for each BD's throughput, considering the feasibility of the optimal TS coefficient. Thus, the optimal time allocation is given by

$$\tau_{1,k}^{*} = \min\left(\max\left(0, \frac{T\mathcal{D}_k}{\mathcal{A}_k + \mathcal{D}_k - \mathcal{B}_k}\right), T\right). \tag{5.16}$$

In addition, $\tau_{2,k}^{*}$ can be obtained as $\tau_{2,k}^{*} = 1 - \tau_{1,k}^{*}$.

5.3.2 Optimizing over PS factor:

This subproblem optimizes the PS factor at the UE during the second phase of each k-th time slot. The resulting optimization problem is reformulated as below:

$$\begin{aligned}
(\text{P5.3}): \ \underset{\beta_k}{\text{maximize}} \ & R_{\text{UE},k}, && \text{(5.17a)}\\
\text{s.t.} \quad & R_{\text{BD}_k}^{(1)} + R_{\text{BD}_k}^{(2)} \geq C_{\text{th}}, \ \forall k, && \text{(5.17b)}\\
& \gamma_{\text{UE},k}^{(2)} \geq \gamma_{\text{BD}_k}^{(2)}, \ \forall k, && \text{(5.17c)}\\
& \text{(5.11c)}. && \text{(5.17d)}
\end{aligned}$$

The throughput of the cooperative phase, $R_{\text{UE},k}^{(2)}$, is solely dependent on the variable β_k in the objective function. However, after simplifying the objective expression of (P5.3), one finds

$$\begin{aligned}
(\text{P5.4}): \ \max_{\beta_k} \ & \mathcal{C} - \tau_{2,k}\log_2\left((1-\beta_k)P_{\text{UE}}|\mathbf{w}_{2,k}^{H}\mathbf{h}|^2 + \sigma^2\right), && \text{(5.18a)}\\
\text{s.t.} \quad & \tau_{2,k}\log_2\left(1 + \frac{(1-\beta_k)P_{\text{UE}}|\mathbf{w}_{2,k}^{H}\mathbf{h}|^2}{\sigma^2}\right) \geq \mathcal{E}, && \text{(5.18b)}\\
& \text{(5.11c)}, && \text{(5.18c)}
\end{aligned}$$

where $\mathcal{C} = R_{\text{UE,k}}^{(1)} + \tau_{2,k}\log_2(\sigma^2)$ and $\mathcal{E} = C_{\text{th}} - R_{\text{BD}_k}^{(1)}$. The objective is an increasing function over β_k. Also, it can be shown that using constraint (5.18b), an upper bound for β_k becomes

as

$$\mathrm{UB}_k = 1 - \frac{\sigma^2 \left[2^{\frac{C_{\mathrm{th}} - R^{(1)}_{\mathrm{BD}_k}}{\tau_{2,k}}} - 1 \right]}{P_{\mathrm{UE}} |\mathbf{w}_{2,k}^H \mathbf{h}|^2}. \tag{5.19}$$

Given the increasing nature of the objective over β_k, it follows that the optimal value of β_k is located in the upper corner of its feasible region, which implies $\beta_k^* = \mathrm{UB}_k$.

5.3.3 Optimizing over receiving beamformers:

This subproblem optimizes the receiving beamforming vectors of the first and second phase given as

$$(\mathrm{P5.5}): \underset{\mathbf{w}_{s,k}, \mathbf{w}_{c,k}}{\text{maximize}} \; R_{\mathrm{UE},k}, \tag{5.20a}$$

$$\text{s.t.} \quad (5.11\mathrm{b}), (5.11\mathrm{g}). \tag{5.20b}$$

Since the combiner vectors for each transmission phase are independent, they can be optimized separately. In the second phase, since the AP receives a signal from only one propagation channel ($\mathbf{h}$), the optimal combiner $\mathbf{w}_{2,k}^*$ is given by $\mathbf{w}_{2,k}^* = \frac{\mathbf{h}}{\|\mathbf{h}\|}$. However, the optimization problem over $\mathbf{w}_{l,k}$ is nonconvex.

As a result, the SDR approach is applied by defining $\mathbf{W}_{l,k} = \mathbf{w}_{l,k}\mathbf{w}_{l,k}^H$, to swap the quadratic form over $\mathbf{w}_{l,k}$ into a linear form, where $\mathbf{W}_{l,k} \succeq 0$, $\forall l$. Accordingly, (P5.5) is

reformulated as

$$(\text{P5.5.1}): \underset{\mathbf{W}_{c,k},\mathbf{W}_{s,k}}{\text{maximize}}\ \tau_{1,k}\log_2\left(1+\frac{P_{\text{UE}}\text{Tr}(\mathbf{H}\mathbf{W}_{s,k})}{\alpha_k P_{\text{UE}}\text{Tr}(\mathbf{G}_k\mathbf{W}_{c,k})+\sigma^2}\right) + R^{(2)}_{\text{UE},k} \tag{5.21a}$$

$$\text{s.t.}\quad \tau_{1,k}\log_2\left(1+\frac{\alpha_k P_{\text{UE}}\text{Tr}(\mathbf{G}_k\mathbf{W}_{c,k})}{\sigma^2}\right)\geq\mathcal{E},\ \forall k, \tag{5.21b}$$

$$\text{Tr}(\mathbf{W}_{l,k})=1,\ \forall k,l, \tag{5.21c}$$

$$\mathbf{W}_{l,k}\succeq 0,\ \forall k,l, \tag{5.21d}$$

$$\text{Rank}(\mathbf{W}_{l,k})=1,\ \forall k,l, \tag{5.21e}$$

where $\mathbf{H}=\mathbf{h}\mathbf{h}^H$ and $\mathbf{G}_k=f_{k,1}\mathbf{g}_k\mathbf{g}_k^H f_{k,1}^H$, $\forall k$. However, (P5.5.1) is not convex. To remove the non-convexity, the first term in objective functions of (P5.5.1) is defined as follows:

$$f(\mathbf{W}_{s,k},\mathbf{W}_{c,k})=\tau_{1,k}\rho(\mathbf{W}_{s,k})-\tau_{1,k}g(\mathbf{W}_{c,k}),\ \forall k, \tag{5.22}$$

where

$$\begin{aligned}\rho(\mathbf{W}_{s,k},\mathbf{W}_{c,k})&=\log_2\left(P_{\text{UE}}\text{Tr}(\mathbf{H}\mathbf{W}_{s,k})+\alpha_k P_{\text{UE}}\text{Tr}(\mathbf{G}_k\mathbf{W}_{c,k})+\sigma^2\right)\\ g(\mathbf{W}_{c,k})&=\log_2(\alpha_k P_{\text{UE}}\text{Tr}(\mathbf{G}_k\mathbf{W}_{c,k})+\sigma^2),\ \forall k.\end{aligned} \tag{5.23}$$

However, (5.22) is still non-concave as it is a difference of two convex functions (DC). Consequently, a locally optimal solution can be obtained by employing SCA [63]. To this end, $g(\mathbf{W}_{c,k})$ is approximated with its first-order Taylor series expansion given as

$$g\left(\mathbf{W}_{c,k}\right)\geq \underbrace{g(\mathbf{W}_{c,k}^{(i)})+\text{Tr}\left(\nabla^H_{\mathbf{W}_{c,k}}g\left(\mathbf{W}_{c,k}^{(i)}\right)\left(\mathbf{W}_{c,k}-\mathbf{W}_{c,k}^{(i)}\right)\right)}_{\tilde{g}(\mathbf{W}_{c,k})}, \tag{5.24}$$

where

$$\nabla^H_{\mathbf{W}_{c,k}}g\left(\mathbf{W}_{c,k}^{(i)}\right)=\frac{\alpha_k P_{\text{UE}}\mathbf{G}_k}{\left(\alpha_k P_{\text{UE}}\text{Tr}(\mathbf{G}_k\mathbf{W}_{c,k}^{(i-1)})+\sigma^2\right)\ln 2}. \tag{5.25}$$

Algorithm 5 Iterative successive convex approximation Algorithm

1: **Input**:Set number of iterations $i = 0,$ maximum number of iterations $I_{\max}$, and initialize $\mathbf{W}_{c,k}^{(0)}$.
2: **Repeat**
3: Calculate $\tilde{g}(\mathbf{W}_{c,k})$ according to (5.24).
4: Solve (P5.5.2) to obtain optimal solution as $\{\mathbf{W}_{l,k}^{(i)}\}$.
5: Set $i \leftarrow i + 1$;
6: **Until** objective in P5.5.2 converges or $i = I_{\max}$
7: Decompose $\mathbf{W}_{l,k}^{(i+1)} = \mathbf{w}_{l,k}^{(i+1)}(\mathbf{w}_{l,k}^{(i+1)})^H$ by performing EVD.
8: **Return:** Optimal solution $\mathbf{w}_{l,k}^*$.

Then, the optimization problem (P5.5.1) can be restated as

$$(\text{P5.5.2}): \underset{\mathbf{W}_{s,k},\mathbf{W}_{c,k}}{\text{maximize}} \ \tau_{1,k}\rho(\mathbf{W}_{s,k}) - \tau_{1,k}\tilde{g}(\mathbf{W}_{c,k}) + R_{\text{UE},k}^{(2)}, \tag{5.26a}$$

$$\text{s.t.} \quad \tau_{1,k}\log_2\left(1+\frac{\alpha_k P_{\text{UE}}\text{Tr}(\mathbf{G}_k\mathbf{W}_{c,k})}{\sigma^2}\right) \geq \mathcal{E}, \tag{5.26b}$$

$$(5.21\text{c}),\ (5.21\text{d}), \tag{5.26c}$$

By relaxing the non-convex rank-one constraint (5.21e), (P5.5.2) can be reformulated as a semidefinite program (SDP) that can be solved to global optimality using CVX [113]. Solving (P5.5.2) has a complexity of $\mathcal{O}((M^2+M)I+M^3)$, where I denotes the number of iterations needed by the interior-point algorithm.

The optimal beamforming solution meets rank-one constraints for $\mathbf{W}_{l,k}$, $\forall l$, ensuring global optimality, and is obtained through eigenvalue decomposition (EVD) [63]. The iterative SCA process for (P5.5.2) is summarized in Algorithm 5. The overall AO algorithm to solve (P5.1) is presented in Algorithm 6, which guarantees convergent solutions with non-increasing objective values [63].

5.4 Numerical results

Numerical results are next presented to evaluate the developed optimization algorithm and the proposed system. The BS and UE locations are $(0, 10)$ and $(10, 1.5)$. Distances are measured in meters. The BDs are randomly located in a circle centered at UE with a radius of

Algorithm 6 Alternating Optimization (AO) Algorithm

1: **Input**: Set the iteration counter $t = 0$, the convergence tolerance $\epsilon > 0$, initial feasible solution β_k. Initialize the objective function value $R_{\mathrm{UE},k}^{(0)} = 0$.
2: **while** $\frac{R_{\mathrm{UE},k}^{(t+1)} - R_{\mathrm{UE},k}^{(t)}}{R_{\mathrm{UE},k}^{(t+1)}} \geq \epsilon$ **do**
3: Obtain $\tau_{1,k}^{(t+1)}$ using (5.15) and (5.16).
4: Obtain $\beta_k^{(t+1)}$ using (5.19).
5: Solve (P5.5.2) to obtain $\mathbf{w}_{l,k}^{(t+1)}$.
6: Calculate the objective function value $R_{\mathrm{UE},k}^{(t+1)}$.
7: Set $t \leftarrow t + 1$;
8: **end while**
9: **Output**: Optimal solutions $\{\tau_{1,k}^*, \beta_k^*, \mathbf{w}_{l,k}^*\}$.

2 meters. Unless otherwise stated, $M = 10$, $K = 4$, $P_{\mathrm{UE}} = 23$ dBm, $\sigma^2 = -70$ dBm, $\alpha_k = 1$, and $I_{\max} = 20$. The distance-dependent pathloss model is given by $L(d) = C_0 \left(\frac{d}{D_0}\right)^{-\nu}$, where $C_0 = -30$ dB is the pathloss at the reference distance $D_0 = 1$ m, d is the link distance, and $\nu = 3$ denotes the pathloss exponent.

Two additional baselines are considered to evaluate our proposed design's performance. In Baseline 1, the receiving beamformer vector at the BS in the SR phase is designed based on the maximum ratio combining (MRC) criterion. This yields on receive beamformer in the SR phase as $\mathbf{w}_{\mathbf{k}}^{\mathrm{MRC}} = \frac{\mathbf{h}+\alpha_{\mathbf{k}}\mathbf{f}_{\mathbf{k},1}\mathbf{g}_{\mathbf{k}}}{\|\mathbf{h}+\alpha_{\mathbf{k}}\mathbf{f}_{\mathbf{k},1}\mathbf{g}_{\mathbf{k}}\|}$. In Baseline 2, the UE does not cooperate, which implies that $\tau_{1,k} = 1$, $\beta_k = 1$. These two baselines allow us to gauge the benefits of our design vis-a-vis the classical MRC design and the case of no cooperation. In addition, in each time slot, the BD_k message reflection only participates in the SR phase (i.e., the corresponding BD in each time slot is silent in the second phase).

Figure 5.2 displays the average throughput for UE and BD in a time slot versus the UE's transmit power, P_{UE}. The figure considers various values of β and both adaptive and fixed C_{th}. In Figure 5.2 (a), the proposed scheme with a fixed $C_{th} = 1$ bps outperforms those with adaptive C_{th}, particularly in the high SNR region. This is because an adaptive threshold limits the resources (such as β) available to meet the BD's constraints, thereby restricting the maximum UE throughput. Additionally, among schemes with adaptive C_{th}, the proposed scheme with fixed $\beta = 0.9$ and MRC achieves 2% and 1% better UE throughput than the scheme with optimal β^*, respectively. However, the scheme with fixed $\beta = 0.7$ performs

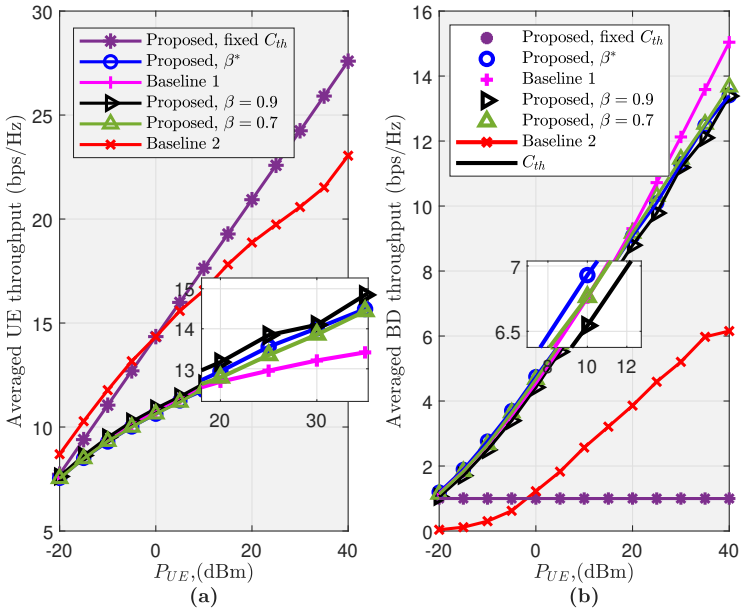

Figure 5.2: (a) UE throughput versus the UE transmit power, (b) BDs throughput versus the UE transmit power

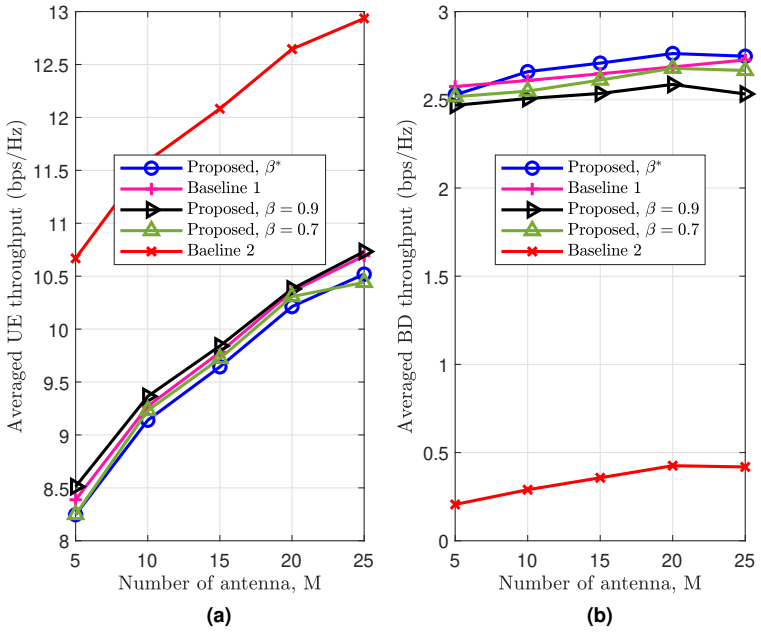

Figure 5.3: (a) UE throughput versus the number of BS antenna, (b) BDs throughput versus the number of BS antenna.

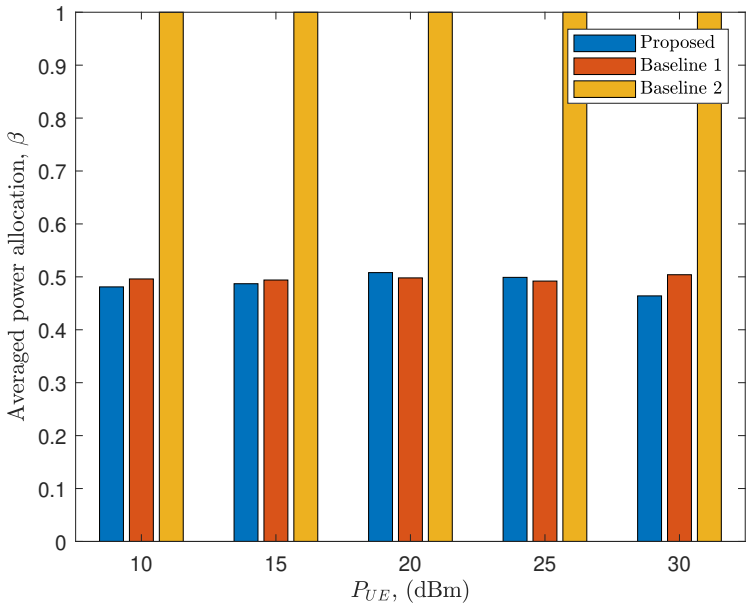

Figure 5.4: Optimal PS factor versus the SNR.

similarly to the one with optimal β. Higher β values lead to better UE throughput, explaining why Baseline 2 ($\beta_k = 1$) has the highest UE throughput. Conversely, BD performance is affected by β and TS coefficient, and the BD's throughput threshold, C_{th}, increases with transmit power, meaning that the BD's throughput must meet higher QoS standards as the UE's power increases. Consequently, the proposed scheme with optimal β effectively maximizes UE throughput while satisfying the BD's C_{th}. Figure 5.2 (b) shows that the proposed scheme achieves more than six times better BD throughput compared to Baseline 2. The solid lines in the figure confirm that the BD's throughput matches the required C_{th}, verifying that the QoS threshold is met.

In Figure 5.3, while there is a notable performance disparity between the proposed design and the non-cooperative scheme (Baseline 2), the difference between Baseline 1 and the proposed design with $\beta_k = 0.9$ is marginal. This highlights the significant impact of β_k on the performance of both UE and BD. A higher β_k improves UE performance at the cost of the BD throughput as it approaches a lower threshold C_{th} for BD. Consequently, since our design considers both UE and BD performance metrics, the optimal β_k it achieves is lower than that of other baselines to meet the BD QoS threshold C_{th}. This explains our design's lower UE throughput and higher BD throughput compared to other schemes.

Figure 5.3 shows the average throughput versus the number of BS antennas. While the proposed design significantly outperforms the non-cooperative scheme (Baseline 2), the difference between Baseline 1 and the proposed design with $\beta = 0.9$ is marginal. This underscores β's impact on both UE and BD performance. Higher β enhances UE performance but reduces BD throughput due to a lower C_{th}. Our design prioritizes UE performance while ensuring BD meets its adaptive QoS threshold C_{th}, resulting in a lower optimal β than other baselines (see 5.4 and 5.5). This explains the lower UE throughput and higher BD throughput in our design. The superior performance of Baseline 1 and the proposed design with β^* may be due to the suboptimal solution from the SCA used in our design.

Figures 5.4 and 5.5 display the average PS factor and TS coefficient across all schemes, respectively. For instance, referring to Figure 5.4, the averaged PS factor at the UE for each BD is approximately 0.5 across varying P_{UE}. In Baseline 1, this coefficient is approximately 0.7, while Baseline 2 does not contribute to BDs' message transmission ($\beta_k = 1$). On the other hand, Figure 5.5 indicates that the achieved optimal TS coefficient for the SR phase in the proposed scheme surpasses that of Baseline 1. This suggests that to maximize the sum throughput of UE, a significant portion of time needs to be allocated to the SR phase. However, to meet the QoS requirements of BDs, the algorithm assigns more power to the cooperative phase. Baseline 1 prioritizes UE throughput, leading to reduced time allocation for the SR phase and decreased power allocation for the cooperative phase compared to the proposed design.

5.5 Conclusion

Deep dyadic fading in backscatter channels results in poor data rates. A cooperative uplink backscatter configuration with a two-phase transmission scheme was introduced as a remedy. Each BD is assigned a time slot divided into two phases in this system. During the initial symbiotic phase, the BD sends its data by reflecting (i.e., backscatter) the uplink signal of the UE. The BS then acts as an integrated receiver that decodes UE and BD signals. In the cooperative phase, the UE allocates a part of its power to integrate the BD signal. The UE transmits this composite signal subsequently to the BS. This setup aims to maximize

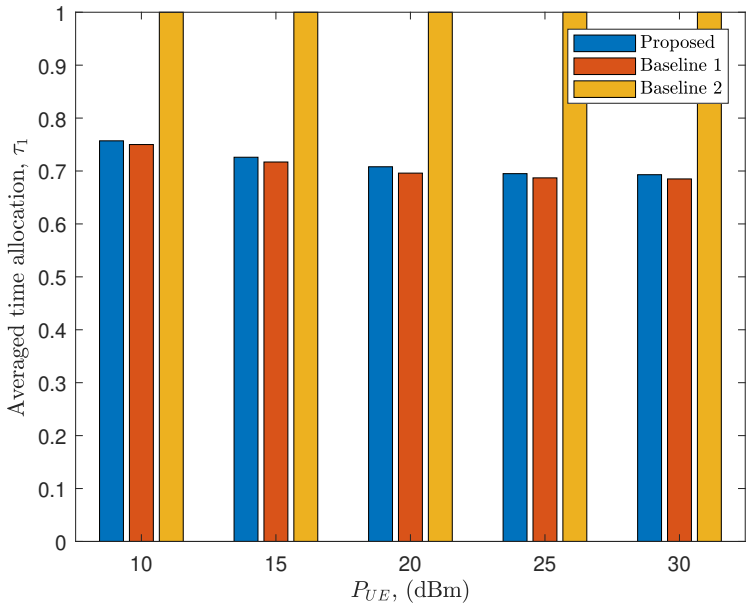

Figure 5.5: Optimal TS coefficient versus the SNR.

the sum UE throughput, optimizing the TS coefficient, PS factor, and received beamforming strategies at the BS. Simulations validate the proposed cooperative approach, demonstrating its ability to enhance BD throughput. This work can be extended to an uplink/downlink scenario where BDs reflect the BS signal to the UE in the downlink, and the UE transmits the BDs signal in the uplink.

Chapter 6

IRS Empowered BackComm Within a Broadcasting ISAC System

This chapter integrates IRS-enabled BackComm with an ISAC system as a spectrum-efficient solution for next-generation wireless communication. The system employs SR assisted by an IRS to enhance primary transmission and enable data conveyance through backscattering. Additionally, an FD-BS supports sensing performance. This chapter formulates a sum rate maximization problem that ensures both IRS data decoding and target sensing, employing a block coordinate descent (BCD) algorithm, along with SDR and SCA techniques.

6.1 Introduction

ISAC [157] unifies communication and sensing technologies, particularly crucial for applications demanding precise sensing capabilities, such as autonomous driving, navigation, and traffic monitoring [158]. To efficiently accommodate the demands of these extensive communication and sensing services while ensuring spectrum efficiency, joint design of sensing and communication systems that share the same frequency, resources, and hardware is advantageous [159].

The amalgamation of IRS with other technologies is another appealing technique [153, 157,160]. IRS comprises many passive programmable reflecting elements that can adjust and manipulate impinging signals' phase and/or magnitude to engineer a wireless propagation

environment. As a result, the integration of the IRS with ISAC is fruitful. For example, in [157], IRS creates a virtual LOS link for target sensing while assisting the downlink communication links between the BS and users. In [160], IRS can simultaneously assist the downlink communication link and track the eavesdropper target using the communication signal. The deep reinforcement learning algorithm is adopted here to maximize the secrecy rate. In addition, [161] proposes an IRS-assisted multi-user multi-target system simultaneously. The goal is to minimize the total transmit power at the BS by optimizing both active and passive beamformers. Furthermore, [162] studies the simultaneous transmitting and reflecting IRS-aided NOMA ISAC. The goal is to minimize the error of the desired sensing beampattern gain.

While the IRS is primarily known for its assisting capabilities, it also finds application in scenarios where it can transmit data via backscattering on incoming signals [153]. In BackComm, devices eschew generating RF signals themselves and instead modulate data over incident RF signals. In this context, each passive reflecting element of IRS can be outfitted with environmental sensors, serving as a backscatter device to re-modulate its data onto received RF signals for reflection [78]. Therefore, IRS-backscattering meets the merit of both backscatter and IRS communication, allowing for low-power, cost-effective passive antenna reflectors as transmitters [153].

Inspired by this discussion, this chapter aims to study the IRS-empowered backscatter in an ISAC system. Here are the contributions:

- A broadcasting system is proposed wherein the BS aims to transmit a common message to multiple recipients while simultaneously conducting target sensing. The communication links are augmented by the IRS.

- Despite the studies conducted in [157, 160, 161], IRS serves two primary functions. Firstly, it enhances communication links by establishing additional propagation paths alongside direct links. Secondly, it utilizes the transmit signal from the BS to modulate and convey its own data to the users.

- The goal is to maximize the sum rate of users by jointly optimizing the active beamformer and combiner vectors at the BS and the phase shifts at IRS. Also, Our design

provides QoS for both sensing target and IRS data at the BS and users, respectively.

6.2 System Model

Figure 6.1 considers an IRS-enabled backscatter in the ISAC broadcasting communication system, which comprises a multi-antenna BS with M antenna, $k \in \{1, \ldots, K\} \triangleq \mathcal{K}$ single-antenna users denoted as U_k, and one IRS with N elements where each element is denoted as $n \in \{1, \ldots, N\} \triangleq \mathcal{N}$. In this practical scenario, an IRS is strategically mounted on a surface, such as a building, offering support for indoor and outdoor applications. In this scenario, the IRS exhibits two distinct advantages. Firstly, it significantly enhances the broadcasting communication system by efficiently reflecting and transmitting BS signals to the users. Secondly, the IRS leverages its unique position to utilize the BS signal and deliver environmental information by piggybacking its data over it and directing it to users. This capability allows users to access real-time environmental information and broadcasting information, enhancing their situational awareness and potentially enabling various location-based services [163]. Let T and T_b be the periods of the primary (i.e., broadcasting message) and secondary (i.e., IRS message) signals. In this configuration, the secondary symbol period is significantly larger than the primary symbol period, denoted as $T_b = LT$, where $L \gg 1$ [163].

Denote $\mathbf{h}_{b,t} = \mathbf{a}_M(\theta) \in \mathcal{C}^{M\times 1}, \mathbf{h}_{b,k} \in \mathcal{C}^{M\times 1}$, $\mathbf{G} \in \mathcal{C}^{N\times M}$ and $\mathbf{h}_{r,k} \in \mathcal{C}^{M\times 1}$ as the complex baseband equivalent channels from the BS to the target, BS to the k-th user, BS to IRS and IRS to the k-th user, respectively. The channels follow the quasi-static fading model, in which the CSI is invariable during one symbol period of the IRS. In the above, $\mathbf{a}_D(\theta) = \left[1, e^{-j\pi\Delta\sin(\theta)}, \ldots, e^{-j\pi\Delta(D-1)\sin(\theta)}\right]^T$ is the array steering vector with dimension D for angle-of-arrival (AoA)/angle-of-departure (AoD) θ with normalized inter-element distance with respect to wavelength Δ.

The BS transmits the broadcast downlink and sensing signal for all recipients U_k as $\mathbf{x}(l) = \mathbf{w}_c s_c(l) + \mathbf{w}_s s_s \in \mathcal{C}^{M\times 1}$. Denote $\mathbf{w}_j \in \mathcal{C}^{M\times 1}, \quad j \in \{c, s\}$ as a beamforming vector pertinent to communication and sensing, and their associate symbol as $s_j(l)$, where $s_j(l) \sim \mathcal{CN}(0, 1)$ $\forall l \in L$, respectively. The IRS adopts binary phase shift-keying (BPSK) to modulate its

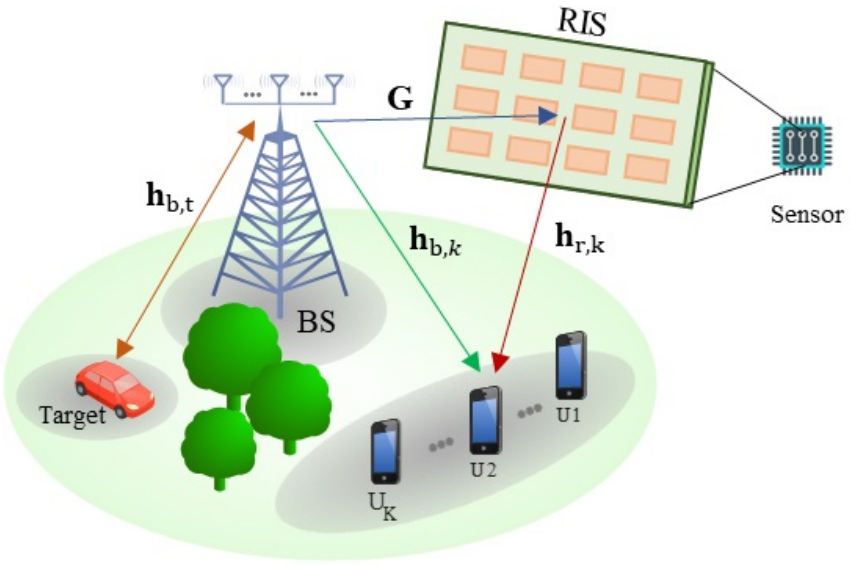

Figure 6.1: System model: IRS-assisted ISAC system.

data over the received BS signal. Thus, the IRS data is $c \in \{1, -1\}$. Therefore, the received signal at the k-th user can be expressed as

$$y_k(l) = \mathbf{h}_k^H \mathbf{w}_c s_c(l) + \underbrace{\mathbf{h}_k^H \mathbf{w}_s s_s(l)}_{\text{sensing interference}} + z_k, \tag{6.1}$$

where $\mathbf{h}_k^H = \mathbf{h}_{b,k}^H + \mathbf{h}_{r,k}^H \Theta \mathbf{G} c$ respectively, $\Theta = \text{diag}(\mathbf{v})$ where $\mathbf{v} = \left[e^{j\theta_1}, \ldots, e^{j\theta_n}, \ldots, e^{j\theta_N}\right]^T, \quad \theta_n \in (0, 2\pi]$, is phase shift matrix of IRS. Denote $z_k \sim \mathcal{CN}(0, \sigma_k^2)$ as additive white Gaussian noise (AWGN) at the k-th user. Therefore, the average rate of the received SINR for decoding s is given by

$$\gamma_k = \frac{|\mathbf{h}_k^H \mathbf{w}_c|^2}{|\mathbf{h}_{b,k}^H \mathbf{w}_s|^2 + |\mathbf{h}_{r,k}^H \Theta \mathbf{G} \mathbf{w}_s|^2 + \sigma_k^2}. \tag{6.2}$$

Therefore, the achievable rate of the k-th user can be expressed as

$$\begin{aligned} R_k &= \mathbb{E}_c \left[\log_2(1 + \gamma_k)\right], \\ &= \sum_{i=1}^{2} \frac{1}{2} \log_2 \left(1 + \frac{|\mathbf{h}_{k,i}^H \mathbf{w}_c|^2}{|\mathbf{h}_{b,k}^H \mathbf{w}_s|^2 + |\mathbf{h}_{r,k}^H \Theta \mathbf{G} \mathbf{w}_s|^2 + \sigma_k^2}\right), \end{aligned} \tag{6.3}$$

where $\mathbf{h}_{k,1}^H = \mathbf{h}_{b,k}^H + \mathbf{h}_{r,k}^H \Theta \mathbf{G}$ and $\mathbf{h}_{k,2}^H = \mathbf{h}_{b,k}^H - \mathbf{h}_{r,k}^H \Theta \mathbf{G}$ denotes as $\mathbf{h}_{k,i}^H$ when c is $\{1\}$ and $\{-1\}$, respectively. After decoding $s_c(l)$, the user performs the SIC to decode the IRS message. Therefore, the corresponding SINR for decoding the IRS message can be expressed as [163]:

$$\gamma_{b,k} = L \frac{|\mathbf{h}_{r,k}^H \Theta \mathbf{G} \mathbf{w}_c|^2}{|\mathbf{h}_{b,k}^H \mathbf{w}_s|^2 + |\mathbf{h}_{r,k}^H \Theta \mathbf{G} \mathbf{w}_s|^2 + \sigma_k^2}. \tag{6.4}$$

Alternatively, the BS utilizes the echo signal received from the target to acquire environmental data. The echo signal received at the BS from the target is consequently represented as:

$$\mathbf{y}_b(l) = \mathbf{h}_{b,t} \mathbf{h}_{b,t}^H \mathbf{x}(l) + \mathbf{z}_b. \tag{6.5}$$

Therefore, BS applies filter receive beamforming $\mathbf{u} \in \mathcal{C}^{M \times 1}$ for detecting the target. Thus, the post-processed signal for the target's sensing information can be given as

$$\mathbf{u}^H \mathbf{y}_b(l) = \mathbf{u}^H \mathbf{h}_{b,t} \mathbf{h}_{b,t}^H \left(\mathbf{w}_c s_c(l) + \mathbf{w}_s s_s \right) + \mathbf{u}^H \mathbf{z}_b, \tag{6.6}$$

As a result, the sensing SNR can be given as

$$\begin{aligned} \gamma_r &= \frac{\mathbb{E}\left[|\mathbf{u}^H \mathbf{H}_{b,t} \left(\mathbf{w}_c s_c + \mathbf{w}_s s_s \right)|^2 \right]}{\mathbb{E}\left[|\mathbf{u}^H \sigma_b^2|^2 \right]}, \\ &= \frac{\mathbf{u}^H \mathbf{H}_{b,t} \left(\mathbf{w}_c \mathbf{w}_c^H + \mathbf{w}_s \mathbf{w}_s^H \right) \mathbf{H}_{b,t}^H \mathbf{u}}{\mathbf{u}^H \sigma_b^2 \mathbf{I}_M \mathbf{u}} \end{aligned} \tag{6.7}$$

where $\mathbf{H}_{b,t} = \mathbf{h}_{b,t} \mathbf{h}_{b,t}^H$.

6.3 Sum User Rate Maximization Problem

This section formulates the sum user rate maximization problem while providing the minimum requirements for target sensing and IRS data decoding. An iterative algorithm is developed to solve this problem.

6.3.1 Problem Formulation

Parameters $\{\mathbf{w}_c, \mathbf{w}_s, \Theta, \mathbf{u}\}$ are jointly designed for maximizing the received sum rate of users, subject to minimum SINR requirement for IRS data decoding and minimum SNR requirement for target sensing. Correspondingly, the joint optimization problem can be expressed as

$$\begin{aligned}
(\text{P6}): \max_{\mathbf{w}_c, \mathbf{w}_s, \Theta, \mathbf{u}} \quad & \sum_{k=1}^{K} R_k\left(\mathbf{w}_c, \mathbf{w}_s, \Theta\right) \\
\text{s.t. } C_1: \quad & \frac{L|\mathbf{h}_{r,k}^H \Theta \mathbf{G} \mathbf{w}_c|^2}{|\mathbf{h}_{b,k}^H \mathbf{w}_s|^2 + |\mathbf{h}_{r,k}^H \Theta \mathbf{G} \mathbf{w}_s|^2 + \sigma_k^2} \geq \Gamma_{c,\min}, \\
C_2: \quad & \frac{\mathbf{u}^H \mathbf{H}_{b,t} \left(\mathbf{w}_c \mathbf{w}_c^H + \mathbf{w}_s \mathbf{w}_s^H\right) \mathbf{H}_{b,t}^H \mathbf{u}}{\mathbf{u}^H \sigma_b^2 \mathbf{I}_M \mathbf{u}} \geq \Gamma_{\min}, \\
C_3: \quad & \|\mathbf{w}_c\|^2 + \|\mathbf{w}_s\|^2 \leq P_{\max}, \\
C_4: \quad & \theta_n \in (0, 2\pi], \ \forall n \in \mathcal{N}.
\end{aligned}$$

Given the problem is non-convex, arising from the entangled optimization variables in the objective and non-convexity of constraints C_1 and C_2, a Block Coordinate Descent (BCD) approach is adopted to tackle this challenge. Specifically, the variables are partitioned into three distinct blocks: $\mathbf{w}_c, \mathbf{w}_s$, Θ, and $\mathbf{u}$. Each block is then optimized iteratively, with the remaining variables held constant during each optimization step. This iterative process allows us to address the nonconvexity effectively, achieving a near-optimal solution.

6.3.2 Receive Beamforming Optimization

For given $\{\mathbf{w}_c,\ \mathbf{w}_s\}$, and Θ, the optimization problem over receive beamforming vector at the BS can be written as a Rayleigh quotient problem [63]

$$(\text{P6.1}): \max_{\mathbf{u}} \quad \frac{\mathbf{u}^H \overbrace{\mathbf{H}_{b,t} \left(\mathbf{w}_c \mathbf{w}_c^H + \mathbf{w}_s \mathbf{w}_s^H\right) \mathbf{H}_{b,t}^H}^{\mathbf{A}} \mathbf{u}}{\mathbf{u}^H \underbrace{\sigma_b^2 \mathbf{I}_M}_{\mathbf{B}} \mathbf{u}}. \tag{6.9}$$

Therefore, the optimal $\mathbf{u}^*$ lies in the eigenvector pertinent to the maximum eigenvalue of the matrix $\mathbf{B}^{-1}\mathbf{A}$.

6.3.3 Transmit Beamforming Optimization

By fixing other variable blocks, the sub-problem for optimizing the transmit beamforming is given by

$$\begin{aligned}(\text{P6.2}): \max_{\mathbf{w}_c,\mathbf{w}_s} \quad & \sum_{k=1}^{K} R_k\left(\mathbf{w}_c, \mathbf{w}_s\right) \\ \text{s.t.} \quad & C_1, C_2, C_3.\end{aligned}$$

(P6.2) remains non-convex due to the quadratic nature of transmitting beamformers. The SDR method is employed to address this issue. Define $\mathbf{W}_c = \mathbf{w}_c\mathbf{w}_c^H$ and $\mathbf{W}_s = \mathbf{w}_s\mathbf{w}_s^H$. Then, P2 can be rewritten as

$$\begin{aligned}(\text{P6.2.1}): \max_{\mathbf{W}_c,\mathbf{W}_s} & \sum_{k=1}^{K}\sum_{i=1}^{2}\log_2\left(1+\frac{\text{Tr}(\mathbf{H}_{k,i}\mathbf{W}_c)}{\text{Tr}(\mathbf{H}_{b,k}\mathbf{W}_s)+\text{Tr}(\mathbf{E}\mathbf{W}_s)+\sigma_k^2}\right) \\ \text{s.t. } \dot{C}_1: & \frac{L\text{Tr}(\mathbf{E}\mathbf{W}_c)}{\text{Tr}(\mathbf{H}_{b,k}\mathbf{W}_s)+\text{Tr}(\mathbf{E}\mathbf{W}_s)+\sigma_k^2} \geq \Gamma_{c,\min}, \\ \dot{C}_2: & \frac{\mathbf{u}^H\mathbf{H}_{b,t}\left(\mathbf{W}_s+\mathbf{W}_c\right)\mathbf{H}_{b,t}^H\mathbf{u}}{\mathbf{u}^H\sigma_b^2\mathbf{I}_M\mathbf{u}} \geq \Gamma_{\min}, \\ \dot{C}_3: & \text{Tr}(\mathbf{W}_s)+\text{Tr}(\mathbf{W}_c) \leq P_{\max} \\ \dot{C}_4: & \text{Rank}(\mathbf{W}_s)=1, \quad \text{Rank}(\mathbf{W}_c)=1,\end{aligned}$$

where $\mathbf{H}_{b,k} = \mathbf{h}_{b,k}\mathbf{h}_{b,k}^H$, and $\mathbf{E} = \left(\mathbf{h}_{r,k}^H\Theta\mathbf{G}\right)^H\left(\mathbf{h}_{r,k}^H\Theta\mathbf{G}\right)$. Problem (P6.2.1) is still nonconvex due to the fractional expression of the objective. To tackle this nonconvexity, SCA is utilized by using the first-order Taylor series approximation near a feasible point $\mathbf{w}_s^{(x)}$ [63]. Therefore,

$$R_k \geq \frac{1}{2\ln 2}\left(\ln\left(1+\frac{|\hat{a}_{k,1}^{(x)}|^2}{\hat{b}_k^{(x)}}\right)-\frac{|\hat{a}_{k,1}^{(x)}|^2}{\hat{b}_k^{(x)}}+\frac{2\mathcal{R}\left\{(\hat{a}_{k,1}^{(x)})^H\hat{a}_{k,1}^{(x)}\right\}}{\hat{b}_k^{(x)}}-\frac{|\hat{a}_{k,1}^{(x)}|^2(|\hat{a}_{k,1}|^2+\hat{b}_k)}{\hat{b}_k^{(x)}(\hat{b}_k^{(x)}+|\hat{a}_{k,1}^{(x)}|^2)}\right.$$
$$\left.+\ln\left(1+\frac{|\hat{a}_{k,2}^{(x)}|^2}{\hat{b}_k^{(x)}}\right)-\frac{|\hat{a}_{k,2}^{(x)}|^2}{\hat{b}_k^{(x)}}+\frac{2\mathcal{R}\left\{(\hat{a}_{k,2}^{(x)})^H\hat{a}_{k,2}^{(x)}\right\}}{\hat{b}_k^{(x)}}-\frac{|\hat{a}_{k,2}^{(x)}|^2(|\hat{a}_{k,2}|^2+\hat{b}_k)}{\hat{b}_k^{(x)}(\hat{b}_k^{(x)}+|\hat{a}_{k,2}^{(x)}|^2)}\right)\triangleq\tilde{R}_k \tag{6.13}$$

(P6.2.1) can be rewritten as follows:

$$\begin{aligned}(\text{P6.2.2}):\max_{\mathbf{W}_c,\mathbf{W}_s}\ &\sum_{k=1}^{K}\sum_{i=1}^{K}\log_2\left(\text{Tr}(\mathbf{H}_{k,i}\mathbf{W}_c)+\text{Tr}((\mathbf{H}_{b,k}+\mathbf{E})\,\mathbf{W}_s)+\sigma_k^2\right),\\ &-\text{Tr}\left(\frac{\mathbf{H}_{k,1}(\mathbf{W}_s-\mathbf{W}_s^{(x)})}{(\mathbf{H}_{b,k}+\mathbf{E})\,\mathbf{W}_s^{(x)}+\sigma_k^2}\right)\\ \text{s.t.}\quad &\dot{C}_1,\dot{C}_2,\dot{C}_3,\dot{C}_4.\end{aligned}$$

After relaxing the rank constraint, the problem (P6.2.2) becomes a standard convex problem. However, its solution gives an upper bound. To tighten the obtained upper bound, the feasible solution $\mathbf{w}_s$ in (P6.2.2) is updated iteratively by using convex optimization tools such as CVX [113] to find a suboptimal solution.

Remark 3. *The transmit beamformers obtained in (P6.2.2) result in a rank-one solution. Thus, $\mathbf{w}_c^*$ can be derived by performing eigenvalue decomposition of $\mathbf{W}_c^*=\mathbf{w}_c^*\mathbf{w}_c^{H*}$. However, since $\mathbf{W}_s$ cannot guarantee a rank-one solution, Gaussian randomization is utilized when it is not rank-one.*

Proof. The proof follows similar steps as in the proof of Proposition 1 in Chapter 3. For the sake of brevity, the proof is emitted here. □

6.3.4 IRS reflection coefficient Optimization

The IRS phase shift is optimized while keeping other block variables constant. Therefore, the optimization problem over the IRS phase shift is

$$\gamma_{b,k} \geq L\frac{\mathbf{v}^{(x)H}\bar{\mathbf{R}}\mathbf{v}^{(x)} + \mathcal{R}\left\{\mathbf{v}^{(x)}(\bar{\mathbf{R}}+\bar{\mathbf{R}}^{H})(\mathbf{v}-\mathbf{v}^{(x)})\right\}}{\hat{b}_k} \triangleq \tilde{\gamma}_{b,k} \tag{6.14}$$

Algorithm 7 BCD Algorithm

1: **Input**: Set the iteration counter $x = 0$, the convergence tolerance $\epsilon > 0$, initial feasible solution $\mathbf{w}_s^{(0)}, \mathbf{v}^{(0)}$. Initialize the objective function value $F^{(0)} = 0$.
2: **while** $\frac{F^{(t+1)}-F^{(t)}}{F^{(t+1)}} \geq \epsilon$ **do**
3: Solve (P2.1) and obtain the optimal solution as $\mathbf{v}^{(x+1)}$.
4: Solve (P3.2) and obtain the optimal solution as $\mathbf{w}_j^{(x+1)}$.
5: Solve (6.9) and obtain the optimal solution as $\mathbf{u}^{(x+1)}$.
6: Calculate the objective function value $F^{(x+1)}$.
7: Set $x \leftarrow x + 1$;
8: **end while**
9: **Output**: Optimal solutions $\{\mathbf{w}_j^*, \mathbf{v}^*, \mathbf{u}^*\}$.

$$\begin{aligned}(\text{P6.3}) : \max_{\Theta} \quad & \sum_{k=1}^{K} R_k\left(\Theta\right) \\ \text{s.t.} \quad & C_1, C_4.\end{aligned}$$

Let us define $\hat{a}_{k,1} = \hat{d}_k + \mathbf{w}_c^H\mathbf{r}_k^H\mathbf{v}$, $\hat{a}_{k,2} = \hat{d}_k - \mathbf{w}_c^H\mathbf{r}_k^H\mathbf{v}$, $\hat{b}_k = \text{Tr}(\mathbf{H}_{b,k}^H\mathbf{W}_s) + \mathbf{v}^H\hat{\mathbf{R}}^H\mathbf{v} + \sigma^2$, $\bar{\mathbf{R}} = \mathbf{r}_k^H\mathbf{r}_k\mathbf{W}_c$, where $\mathbf{r}_k = (\text{diag}(\mathbf{h}_{r,k})^H)\mathbf{G}$, $\hat{d}_k = \text{Tr}(\mathbf{H}_{b,k}\mathbf{W}_c)$ and $\hat{\mathbf{R}} = \mathbf{r}_k^H\mathbf{r}_k\mathbf{W}_s$.

The sum users rate and IRS SNR can be rewritten as

$$R_k = \frac{1}{2}\log_2\left(1+\frac{|\hat{a}_{k,1}|^2}{\hat{b}_k}\right) + \frac{1}{2}\log_2\left(1+\frac{|\hat{a}_{k,2}|^2}{\hat{b}_k}\right), \quad \forall k \in \mathcal{K}, \tag{6.16}$$

The rate expression (6.16) and $C1$ are non-convex, rendering (P6.3) intractable. To overcome this, a viable approach is to apply an approximate transformation that converts the problem into a convex form. This can be done by utilizing the lower-bound of (6.16) as

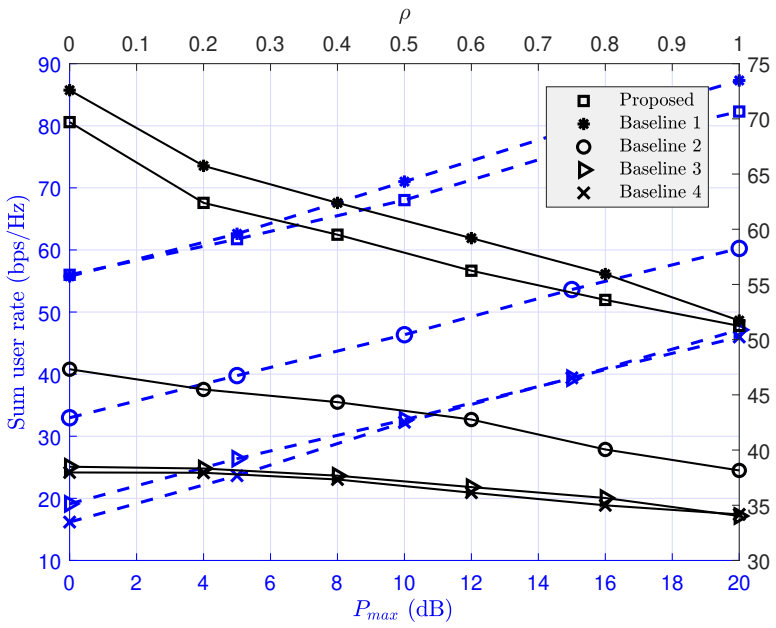

Figure 6.2: Sum user rate vs. maximum BS transmit power and CSI imperfection factor ρ.

(6.13) and lower bound of $C1$ as (6.14). Therefore, (P3) can be rewritten as

$$\begin{aligned} (\text{P6.3.1}) : \max_{\mathbf{v}} \quad & \sum_{k=1}^{K} \tilde{R}_k(\mathbf{v}) \\ \text{s.t.} \quad & \tilde{\gamma}_{b,k} \geq \Gamma_{c,\min}, \forall k \in \mathcal{K}, \\ & |\mathbf{v}[n]| \leq 1, \forall n \in \mathcal{N}. \end{aligned}$$

Now, it can be seen that (P6.3.1) is convex and can be solved using CVX. Nonetheless, the feasible solution of (P6.3.1) is iteratively updated to enhance the obtained lower bound. Algorithm 7 outlines all the steps to solve (P6). Overall, the BCD algorithm converges given a non-increasing objective [63] to a sub-optimal solution of (P6), albeit without guaranteeing global or local optimality. Our approach only provides a sub-optimal solution. Moreover, the proposed algorithm has a complexity of $\mathcal{O}(I_O((M^2+M)I_I + 2M^3))$, where I_O and I_I represent the number of iterations required for the outer BCD algorithm and the interior-point algorithm to converge, respectively.

6.4 Numerical Results

Simulation results are presented to assess the effectiveness of our proposed schemes. The setup consists of the following: the BS is positioned at the origin $(0, 0)$, the IRS is located at $(100, 0)$, users are distributed in a circle centered at the origin of the IRS with a radius of 5, and the target is situated at -40 angle from the BS. Unless specified otherwise, the simulation parameters are as follows: $K = 4$, $M = 10$, $N = 100$, $\kappa = 3$dB, $\sigma^2 = -80$dBm, $L = 50$, $\Gamma_{c,\min} = \Gamma_{\min} = 10$ dB, and the pathloss model is defined as $\text{PL} = 10^{-3}(\frac{d}{d_0})^{\nu}$, where $d_0 = 1$m, d denotes the distance between terminals in meters, and ν represents the pathloss exponent, which is set to 3.5, 2.8, 2, and 3, for BS-user, IRS-user, BS-IRS, and BS-target links, respectively [161,163]. The small-scale fading of the link related to BS to IRS and IRS to the k-th user is modeled as Rician fading given as $\mathbf{X} = \sqrt{\frac{\kappa}{\kappa+1}}\mathbf{X}_{\text{LoS}} + \sqrt{\frac{1}{\kappa+1}}\mathbf{X}_{\text{NLoS}}$, where $\mathbf{X} \in \{\mathbf{G}, \mathbf{h}_{r,k}\}$. Subscripts LoS, NLoS, and κ denote the line-of-sight (LoS) component, non-LoS component, and Rician factor, respectively. The NLoS component is modeled as the Rayleigh fading, where the element satisfies $\mathcal{CN}(0, 1)$, and $\mathbf{G}_{\text{LoS}} = \mathbf{a}_N(\theta_{\text{AoA}})\mathbf{a}_M(\theta_{\text{AoD}})^H$, $\mathbf{h}_{rk,\text{LoS}} = \mathbf{a}_N(\theta_{\text{AoD}})$. We assume a LoS channel between the BS and target to enhance accuracy and reliability, as required in applications like traffic management. This assumption is valid in urban environments with elevated BS placement and short-range scenarios, where the direct path dominates.

To validate our design, four baseline scenarios are tested. Baseline 1 includes a communication signal only without a dedicated sensing signal. Thus, the sensing is also performed with the same communication signal. Baseline 2 does not optimize the IRS but utilizes random phase shifts. Baseline 3 indicates a case where the IRS panel is replaced with a backscatter device with a single antenna. Baseline 4 does not include an IRS; thus, the IRS does not improve the downlink. Consequently, no messages are transmitted from the IRS to the receivers.

Figure 6.2 shows the sum of user rates as a function of the maximum BS transmit power (bottom x-axis) and the CSI imperfection factor, ρ (top x-axis), due to imperfect channel estimation (CE). Let $\hat{\mathbf{h}}$ be the estimate of the true channel $\mathbf{h}$. Generally, $\hat{\mathbf{h}} = \mathbf{h} + \mathbf{n}$, where $\mathbf{n}$ is a noise vector following $\mathcal{CN}(0, \sigma_n^2\mathbf{I})$, and $\sigma_n^2 = \rho\|\mathbf{h}\|^2$ [63], with ρ being the ratio of

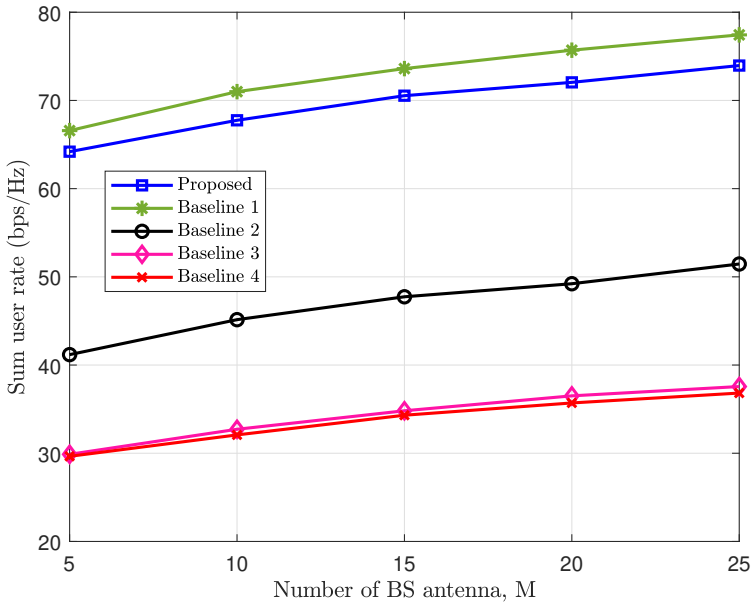

Figure 6.3: Sum user rate vs. number of BS antenna.

noise power to channel gain. For sum rate versus P_{max}, the proposed scheme outperforms Baselines 2-4, showing 53%, 120%, and 138% gains over Baseline 2, Baseline 3, and Baseline 4, respectively. This highlights the significant impact of the IRS and its phase optimization on communications. Baseline 3 slightly outperforms Baseline 4 due to the additional multipath provided by a single reflector in Baseline 3. However, Baseline 1 has a slightly higher sum rate due to the removal of the dedicated sensing signal, which reduces sensing interference in communications. This results in the proposed scheme having a 2% performance loss compared to Baseline 1. As the CE error ρ increases, rates decrease. Specifically, when perfect CSI is unavailable ($\rho = 1$), we see losses of 26% in the proposed scheme and 28%, 19%, 11%, and 10% in Baselines 1-4, respectively.

Fig. 6.3 illustrates the sum user rate versus the number of BS transmit antennas, in which a higher number correlates with an improved sum user rate. This trend is consistent in Fig. 6.2 as well. Specifically, Baseline 1 exhibits slightly better performance, e.g., 4% gain than the proposed scheme. This is because Baseline 1 does not have a dedicated sensing signal, which otherwise causes interference on the users. However, the proposed scheme outperforms Baselines 2, 3, and 4 by approximately 45%, 103% and 107%, respectively. This underscores the significance of optimized IRS phase shift design and the presence of IRS.

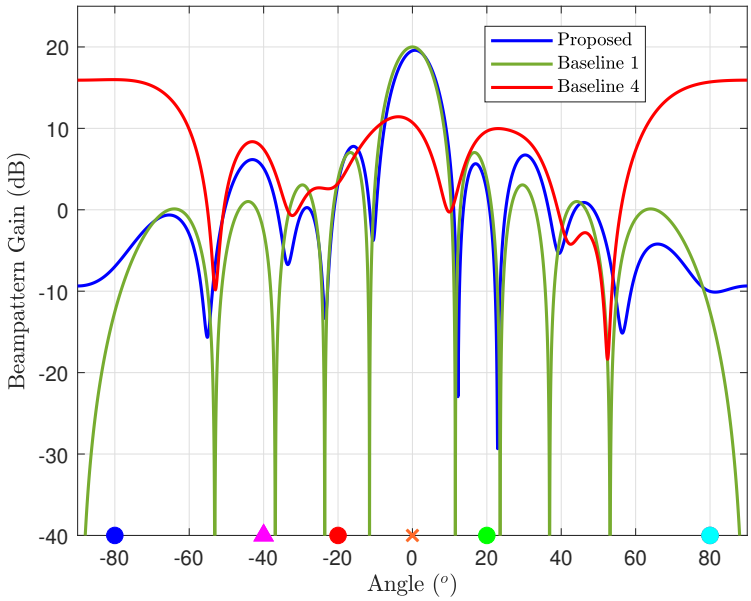

Figure 6.4: Beamgain vs. angles: The red circle marks the target angle, the blue circles represent the angles of the users, and the green circle denotes the angle of the IRS, which is set at zero degrees.

Fig. 6.4 illustrates the beam pattern gain. It demonstrates the alignment of beams toward users and the target. In both the proposed scheme and Baseline 1, the highest beam gain is directed towards the IRS due to the increased pathloss exponent experienced by the direct link. However, in the proposed scheme, the beam gain towards the target surpasses that of Baseline 1, attributed to the dedicated sensing beamformer employed. Conversely, in Baseline 4, the absence of the IRS redirects the majority of beam focus toward users, contrary to the other two schemes.

6.5 Conclusion

This study explores using IRS-empowered BackComm and ISAC. The BS transmit signal is engineered to serve both SR and sensing functions, with the latter augmented by IRS. In addition, IRS can modulate and backscatter data towards the downlink system. The analysis focuses on the sum user rate while ensuring QoS for sensing and IRS data decoding, considering BS transmitting and receiving beamforming and IRS phase-shifts. As this optimization problem is non-convex, the BCD algorithm is developed, utilizing SDR techniques

for transmit beamformer optimization. A lower bound is derived for designing IRS phase shifts, and a closed-form solution is provided for the receiving beamformer. The results demonstrate a significant improvement, exceeding 50% over other baseline approaches.

Chapter 7

Conclusion of Completed Works and Future Work

Completed works are reviewed, and conclusions are drawn. Extensions of the thesis research are outlined.

7.1 Conclusion of Completed Works

The completed research has resulted in three published papers (see Preface) [100,153]. Chapter 3 addressed challenges for Monostatic BackComm networks. The proposed MIMO reader provided a pivotal solution to avoid signal collisions among tags in multi-tag scenarios by employing spatial domain multiple access. Operating in a FD manner, the MIMO reader required effective control over RSI, validated through software-based optimization constraints. Energy constraints for batteryless tags were also integrated, ensuring robust sum rates while meeting network requirements.

Chapter 4, focusing on spectrum-sharing within BackComm, explored the use of IRS for BackComm, leveraging downlink NOMA signals. This work contributed by enabling IRS-enabled backscatter to modulate data over environmental sources and act as a relay for the primary network's messages. Power splitting at the source facilitated the transmission of distinct, frequency-separated signals to manage signal interference between networks, effectively mitigating interference from secondary systems on primary networks.

Chapter 5 investigated a cooperative spectrum-sharing SR system. This chapter centered on an uplink SR system where each BD is assigned to a time slot to perform two transmission phases. In the first phase (SR phase) of each time slot, scheduled BD utilized signals from UE to transmit its data by piggybacking and scattering to a BS. In the subsequent phase, the BD remained silent. At the same time, the UE collaborated to transmit BD's data by decoding and integrating it into its message, with different power levels allocated for each stream. Performance assessments focused on the sum throughput maximization problem. Sum throughput optimization highlighted enhanced BD throughput in the cooperative system compared to non-cooperative schemes.

Chapter 6 explored integrating IRS-backscattering within the SR communication and sensing network. Specifically, the BS has two primary functions: broadcasting information to downlink users and detecting targets in the uplink. Meanwhile, the IRS in this model can enhance the downlink communication link and convey supplementary data to users by modulating its data over the downlink signal. This proposed system model is advantageous in sensor-rich environments for data exchange. The performance analysis maximizes the sum user rate while ensuring QoS for target and IRS data decoding. Results highlight the superior performance of this design in serving both sensing and communication systems.

7.2 Future Research Directions

This section discusses diverse possibilities for expanding upon the thesis research and exploring avenues for further investigation and development.

7.2.1 FD-MIMO Monostatic BackComm with Suppressing RSI

Some potential avenues for future research on the FD-MIMO Monostatic BackComm with the suppression of RSI as discussed in Chapter 3 include:

- The suggested multiple access approach in this chapter relies on SDMA, where multiple antennas at the reader distinguish signals from various tags spatially. However, a constraint of SDMA is that the number of antennas at the receiver must exceed the

number of tags, posing a challenge for deploying such a system in dense IoT networks. Therefore, setting up NOMA as a multiple-access system is a viable extension of this chapter. Simultaneous reflections at the tags are permitted by NOMA transmission without any restriction on several tags. Tags can either reflect with a different codebook denoting code-domain-NOMA or backscatter with a different reflection power denoting power-domain-NOMA, which allows the reader to decipher each tag's signal.

- Another viable extension is to expand this system to multi-MIMO Monostatic Back-Comm pairs. This would be a practical system model as, in practice, there might be more than one reader-tag pair. In a manufacturing factory, for instance, the simultaneous operation of two or more handheld readers is feasible for tracking and reading sensor data. Consequently, a new problem formulation should account for managing interference between each reader-tag pair.

- Although linear EH models are often assumed when integrating various energy harvesting techniques, nonlinear models more accurately represent actual EH circuits. While linear models provide useful insights, they may oversimplify the complexities of real-world systems. Therefore, exploring nonlinear EH is crucial for capturing the intricacies of real energy harvesting systems, leading to a more comprehensive understanding of the associated challenges and opportunities.

7.2.2 IRS-Enabled Backscattering in a Downlink Non-Orthogonal Multiple Access System

Some potential avenues for future research on the IRS-backscattering in the NOMA system as discussed in Chapter 4, include:

- While investigating a two-user downlink NOMA scenario is practical, there is significant value in expanding this study to include scenarios with multiple NOMA users, involving more than just two users. Extending the scope of the study to encompass a greater number of users reflects real-world scenarios more accurately. However, handling the increased complexity associated with successive interference cancellation in scenarios

with multiple users poses a challenge. To address this challenge, employing a clustering algorithm becomes a worthwhile approach. By utilizing a clustering algorithm, such as K-means, Hierarchical Clustering, or other suitable methods, users can be organized into manageable groups of two NOMA users each.

- An intriguing avenue for research involves substituting IRS with STAR-IRS to enable backscatter. The STAR-IRS element splits the incident signal into two components: one is directed to the opposite side, referred to as the transmission space, and the other is reflected into the same space as the incident signal, denoted as the reflection space [164]. This characteristic allows STAR-IRS to offer complete coverage of the entire space. Consequently, replacing IRS with STAR-IRS facilitates relaying primary information to downlink NOMA users. Simultaneously, STAR-IRS can modulate its data and reflect it to the reader in the reflection space.

- While the IRS primarily functions by passively reflecting incident signals, it is essential to acknowledge the non-negligible power consumption associated with its operation, as highlighted in previous studies [165, 166]. The power consumption of the IRS is inherently tied to the quantity of reflective elements it incorporates. In the pursuit of addressing this energy-related concern, an intriguing extension to this research involves exploring the integration of a self-sustainable IRS powered by wireless power transfer. By incorporating wireless power transfer technology, the proposed extension aims to offset or compensate for the power consumption of the IRS while pursuing other system requirements. This addition not only contributes to the energy efficiency of the IRS but also introduces a dimension of sustainability.

7.2.3 Symbiotic Backscatter Networks Through Cooperative Communication

Some potential avenues for future research from Chapter 5 include:

- Chapter 5 research can be extended to uplink and downlink scenarios. In the downlink, the BS transmits its signal to the UE, while a BD leverages this signal to convey its

own data. The UE, after decoding both the BS's and BD's data, can integrate BD's data into its own transmission stream. This combined stream can then be assigned to different power levels and transmitted back to the BS in the uplink. Another extension is to examine the power requirements of the BD, particularly by exploring EH techniques.

- To further optimize the system's performance, integrating a massive MIMO BS holds considerable promise for several reasons. The spatial focusing capabilities inherent in massive MIMO facilitate more efficient signal delivery and reception to and from devices. This enhances overall coverage and mitigates dead zones [167]. Exploiting spatial diversity, massive MIMO effectively addresses fading effects induced by signal reflections and multipath propagation, leading to heightened signal reliability. Incorporating a massive MIMO BS introduces a new dimension to the system, impacting the analysis and the resolution of the sum throughput maximization problem. The unique capabilities of massive MIMO necessitate reevaluating the strategies discussed in Chapter 5.

7.2.4 IRS Empowered Backscatter in broadcasting ISAC system

Some potential avenues for future research on the IRS Empowered Backscatter in broadcasting ISAC as discussed in Chapter 6 include:

- The system model in this chapter is based on a single target. However, this work can be extended to multiple target detection in the uplink, which is particularly useful for scenarios like asset tracking or logistics. Additionally, the scenario can be generalized to include both uplink and downlink transmission. In the downlink, the BS transmits a communication signal to the user, and the IRS can also modulate its data onto it. In the uplink, the BS receives signals from users and the target echo. In this case, the design of the receive beamformer at the BS should also account for inter-user and target interference.

- In this chapter, the IRS backscatters its data and relays primary system information. It is assumed that there is no direct link between the IRS and the target, enhancing the

sensing link between the BS and the target. To further improve the sensory network, this work could focus on a scenario where the phase shift design at the IRS also considers enhancing the link toward the target. Another compelling scenario would involve using a separate IRS to support the sensing network.

Bibliography

[1] 3GPP, "3rd Generation Partnership Project; Technical Specification Group Services and System Aspects; Feasibility Study on New Services and Markets Technology Enablers for Massive Internet of Things; Stage 1 (Release 14)," Technical Report 3GPP TR 22.861 V14.1.0, 3rd Generation Partnership Project (3GPP), Sept. 2016.

[2] M. L. Memon, N. Saxena, A. Roy, and D. R. Shin, "Backscatter communications: Inception of the battery-free era—A comprehensive survey," *Electronics*, vol. 8, no. 2, p. 129, 2019.

[3] B. Gu, D. Li, H. Ding, G. Wang, and C. Tellambura, "Breaking the interference and fading gridlock in backscatter communications: State-of-the-art, design challenges, and future directions," *IEEE Commun. Surv. & Tutor.*, 2024.

[4] F. Rezaei, C. Tellambura, and S. Herath, "Large-scale wireless-powered networks with backscatter communications—A comprehensive survey," *IEEE open j. Commun. Soc.*, vol. 1, pp. 1100–1130, 2020.

[5] S. Gong, Y. Zou, D. T. Hoang, J. Xu, W. Cheng, and D. Niyato, "Capitalizing backscatter-aided hybrid relay communications with wireless energy harvesting," *IEEE Internet Things J.*, vol. 7, no. 9, pp. 8709–8721, 2020.

[6] 3GPP TSG RAN, "Rel-18 workshop: 5G evolution support of NR passive IoT." Electronic Meeting, June 2021. RWS-210453, Agenda Item: 4.2.

[7] D. L. Galappaththige, F. Rezaei, C. Tellambura, and S. P. Herath, "Link budget analysis for backscatter-based passive IoT," *IEEE Access*, vol. 10, pp. 128890–128922, 2022.

[8] F. Rezaei, C. Tellambura, and S. P. Herath, "Large-scale wireless-powered networks with backscatter communications - A comprehensive survey," *IEEE Open J. Commun. Soc.*, vol. 1, pp. 1100–1130, 2020.

[9] F. Rezaei, D. L. Galappaththige, C. Tellambura, and S. P. Herath, "Coding techniques for backscatter communications - A contemporary survey," *IEEE Commun. Surv. Tutor.*, vol. 25, no. 2, pp. 1020–1058, 2023.

[10] N. V. Huynh, D. T. Hoang, X. Lu, D. Niyato, P. Wang, and D. I. Kim, "Ambient backscatter communications: A contemporary survey," *IEEE Commun. Surv. Tutor.*, vol. 20, no. 4, pp. 2889–2922, 2018.

[11] 3GPP TSG RAN, "Moderators Summary for Discussion [RAN94e-R18Prep-28] Passive IoT (From RP-212688)," Dec. 2021. [Online]. Available: `https://portal.3gpp.org/ngppapp/TdocList.aspx?meetingId=60043`.

[12] J. Kimionis, A. Bletsas, and J. N. Sahalos, "Increased range bistatic scatter radio," *IEEE Trans. Commun.*, vol. 62, no. 3, pp. 1091–1104, 2014.

[13] X. Tang, G. Xie, and Y. Cui, "Self-sustainable long-range backscattering communication using RF energy harvesting," *IEEE Internet Things J.*, vol. 8, no. 17, pp. 13737–13749, 2021.

[14] S. Zargari, A. Hakimi, F. Rezaei, C. Tellambura, and A. Maaref, "Signal detection in ambient backscatter systems: Fundamentals, methods, and trends," *IEEE Access*, vol. 11, pp. 140287–140324, 2023.

[15] Q. Tao, Y. Li, C. Zhong, S. Shao, and Z. Zhang, "A novel interference cancellation scheme for bistatic backscatter communication systems," *IEEE Commun. Lett.*, vol. 25, no. 6, pp. 2014–2018, 2021.

[16] J. F. Ensworth, A. T. Hoang, T. Q. Phu, and M. S. Reynolds, "Full-duplex bluetooth low energy (BLE) compatible backscatter communication system for mobile devices," in *IEEE Topical Conference on Wireless Sensors and Sensor Networks, WiSNet, Phoenix, AZ, USA, January 15-18*, pp. 45–48, IEEE, 2017.

[17] "European Union document on 5G evolution." `https://eur-lex.europa.eu/legal-content/EN/TXT/HTML/?uri=CELEX:52016SC0303&from=SV`. Accessed: September 19, 2024.

[18] S. Xiao, H. Guo, and Y. Liang, "Resource allocation for full-duplex-enabled cognitive backscatter networks," *IEEE Trans. Wirel. Commun.*, vol. 18, no. 6, pp. 3222–3235, 2019.

[19] Z. Hu, S. Yang, and Z. Zhang, "Ambient backscatter-based power control strategies for spectrum sharing networks," *IEEE Trans. Cogn. Commun. Netw.*, vol. 8, no. 4, pp. 1848–1861, 2022.

[20] D. L. Galappaththige, F. Rezaei, C. Tellambura, and S. P. Herath, "RIS-empowered ambient backscatter communication systems," *IEEE Wirel. Commun. Lett.*, vol. 12, no. 1, pp. 173–177, 2023.

[21] Y. Zhang, B. Li, F. Gao, and Z. Han, "A robust design for ultra reliable ambient backscatter communication systems," *IEEE Internet Things J.*, vol. 6, no. 5, pp. 8989–8999, 2019.

[22] G. Yang, X. Xu, and Y. Liang, "Resource allocation in NOMA-enhanced backscatter communication networks for wireless powered iot," *IEEE Wirel. Commun. Lett.*, vol. 9, no. 1, pp. 117–120, 2020.

[23] Y. Liao, G. Yang, and Y. Liang, "Resource allocation in NOMA-enhanced full-duplex symbiotic radio networks," *IEEE Access*, vol. 8, pp. 22709–22720, 2020.

[24] C. He, S. Chen, H. Luan, X. Chen, and Z. J. Wang, "Monostatic MIMO backscatter communications," *IEEE J. Sel. Areas Commun.*, vol. 38, no. 8, pp. 1896–1909, 2020.

[25] D. Mishra and J. Yuan, "Optimizing backscattering coefficient design for minimizing BER at monostatic MIMO reader," in *IEEE International Conference on Acoustics, Speech and Signal Processing, ICASSP*, pp. 9165–9169, IEEE, 2020.

[26] A. Al-Nahari, R. Jäntti, D. Mishra, and J. Hämäläinen, "Massive MIMO beamforming in monostatic backscatter multi-tag networks," *IEEE Commun. Lett.*, vol. 25, no. 4, pp. 1323–1327, 2021.

[27] W. Liu, K. Huang, X. Zhou, and S. Durrani, "Next generation backscatter communication: systems, techniques, and applications," *EURASIP J. Wirel. Commun. Netw.*, vol. 2019, p. 69, 2019.

[28] K. Finkenzeller, *RFID handbook: fundamentals and applications in contactless smart cards, radio frequency identification and near-field communication*. John wiley & sons, 2010.

[29] J. Liao, X. Wang, K. Ruttik, R. Jäntti, and D.-T. Phan-Huy, "In-band ambient FSK backscatter communications leveraging LTE cell-specific reference signals," *IEEE Journal of Radio Frequency Identification*, vol. 7, pp. 267–277, 2023.

[30] W. Liu, K. Huang, X. Zhou, and S. Durrani, "Next generation backscatter communication: systems, techniques, and applications," *EURASIP J. Wirel. Commun. Netw.*, vol. 2019, p. 69, 2019.

[31] Huawei, "5G evolution support of NR passive IoT." 3GPP TSG RAN Rel-18 workshop, Accessed: RWS-210453, 2021.

[32] Huawei, "Study proposal on passive IoT ." 3GPP TSG RAN meeting 94e, Accessed: Dec. 6, RP-213368, 2021.

[33] X. Lu, H. Jiang, D. Niyato, D. I. Kim, and Z. Han, "Wireless-powered device-to-device communications with ambient backscattering: Performance modeling and analysis," *IEEE Trans. Wirel. Commun.*, vol. 17, no. 3, pp. 1528–1544, 2018.

[34] W. Ma, W. Wang, and T. Jiang, "Joint energy harvest and information transfer for energy beamforming in backscatter multiuser networks," *IEEE Trans. Commun.*, vol. 69, no. 2, pp. 1317–1328, 2021.

[35] T. D. P. Perera, D. N. K. Jayakody, S. K. Sharma, S. Chatzinotas, and J. Li, "Simultaneous wireless information and power transfer (SWIPT): recent advances and future challenges," *IEEE Commun. Surv. Tutorials*, vol. 20, no. 1, pp. 264–302, 2018.

[36] B. Pozo, J. I. Garate, J. Á. Araujo, and S. Ferreiro, "Energy harvesting technologies and equivalent electronic structural models," *Electronics*, vol. 8, no. 5, p. 486, 2019.

[37] "GAO RFID Inc.," Available Online: `https://gaorfid.com/`.

[38] D. Wang, F. Rezaei, and C. Tellambura, "Performance analysis and resource allocations for a WPCN with a new nonlinear energy harvester model," *IEEE Open J. Commun. Soc.*, vol. 1, pp. 1403–1424, 2020.

[39] E. Boshkovska, D. W. K. Ng, N. Zlatanov, and R. Schober, "Practical non-linear energy harvesting model and resource allocation for SWIPT systems," *IEEE Commun. Lett.*, vol. 19, no. 12, pp. 2082–2085, 2015.

[40] Y. Dong, M. J. Hossain, and J. Cheng, "Performance of wireless powered amplify and forward relaying over Nakagami-m fading channels with nonlinear energy harvester," *IEEE Commun. Lett.*, vol. 20, no. 4, pp. 672–675, 2016.

[41] D. Mishra and E. G. Larsson, "Monostatic backscattering detection by multiantenna reader," in *53rd Asilomar Conference on Signals, Systems, and Computers, ACSCC , Pacific Grove, CA, USA, November 3-6* (M. B. Matthews, ed.), pp. 697–701, IEEE, 2019.

[42] X. Jia, X. Zhou, D. Niyato, and J. Zhao, "Intelligent reflecting surface-assisted bistatic backscatter networks: Joint beamforming and reflection design," *IEEE Trans. Green Commun. Netw.*, vol. 6, no. 2, pp. 799–814, 2022.

[43] Z. B. Zawawi, Y. Huang, and B. Clerckx, "Multiuser wirelessly powered backscatter communications: Nonlinearity, waveform design, and SINR-energy tradeoff," *IEEE Trans. Wirel. Commun.*, vol. 18, no. 1, pp. 241–253, 2019.

[44] X. Lu, D. Niyato, H. Jiang, D. I. Kim, Y. Xiao, and Z. Han, "Ambient backscatter assisted wireless powered communications," *IEEE Wirel. Commun.*, vol. 25, no. 2, pp. 170–177, 2018.

[45] D. T. Hoang, D. Niyato, D. I. Kim, N. Van Huynh, and S. Gong, *Ambient backscatter communication networks*. Cambridge University Press, 2020.

[46] J. Kimionis, A. Bletsas, and J. N. Sahalos, "Bistatic backscatter radio for power-limited sensor networks," in *IEEE Global Communications Conference, GLOBECOM , Atlanta, GA, USA, December 9-13*, pp. 353–358, IEEE, 2013.

[47] J. G. Proakis and M. Salehi, *Digital communications*, vol. 4. McGraw-hill New York, 2001.

[48] D. Mishra and E. G. Larsson, "Sum throughput maximization in multi-tag backscattering to multiantenna reader," *IEEE Trans. Commun.*, vol. 67, no. 8, pp. 5689–5705, 2019.

[49] Z. Niu, W. Wang, and T. Jiang, "Spatial modulation for ambient backscatter communications: Modeling and analysis," in *IEEE Global Communications Conference, GLOBECOM , Waikoloa, HI, USA, December 9-13*, pp. 1–6, IEEE, 2019.

[50] G. Hu, Y. Zhu, W. Zhao, M. Jia, B. Juliyanto, and Y. Y. Nazaruddin, "Signal detection for batteryless backscatter systems with multiple-antenna tags," in *IEEE/CIC International Conference on Communications in China - Workshops, ICCC Workshops , Changchun, China, August 11-13,*, pp. 77–81, IEEE, 2019.

[51] J. K. Devineni and H. S. Dhillon, "Exact bit error rate analysis of ambient backscatter systems under fading channels," in *88th IEEE Vehicular Technology Conference, VTC Fall, Chicago, IL, USA, August 27-30*, pp. 1–6, IEEE, 2018.

[52] S. N. Daskalakis, R. Correia, G. Goussetis, M. M. Tentzeris, N. B. Carvalho, and A. Georgiadis, "Four-PAM modulation of ambient FM backscattering for spectrally efficient low-power applications," *IEEE Trans. Microw. Theory Tech.*, vol. 66, no. 12, pp. 5909–5921, 2018.

[53] C. Boyer and S. Roy, "Invited paper - backscatter communication and RFID: coding, energy, and MIMO analysis," *IEEE Trans. Commun.*, vol. 62, no. 3, pp. 770–785, 2014.

[54] E. Björnson, J. Hoydis, L. Sanguinetti, *et al.*, "Massive MIMO networks: Spectral, energy, and hardware efficiency," *Foundations and Trends® in Signal Processing*, vol. 11, no. 3-4, pp. 154–655, 2017.

[55] Q. Yang, H. Wang, Y. Zhang, and Z. Han, "Physical layer security in MIMO backscatter wireless systems," *IEEE Trans. Wirel. Commun.*, vol. 15, no. 11, pp. 7547–7560, 2016.

[56] F. Ke, Y. Peng, Y. Peng, and D. W. K. Ng, "Resource allocation for MIMO full-duplex backscatter assisted wireless-powered communication network with finite alphabet inputs," *IEEE Trans. Commun.*, vol. 69, no. 2, pp. 1275–1289, 2021.

[57] D. Mishra and E. G. Larsson, "Multi-tag backscattering to MIMO reader: Channel estimation and throughput fairness," *IEEE Trans. Wirel. Commun.*, vol. 18, no. 12, pp. 5584–5599, 2019.

[58] M. Mohammadi, Z. Mobini, D. L. Galappaththige, and C. Tellambura, "A comprehensive survey on full-duplex communication: Current solutions, future trends, and open issues," *IEEE Commun. Surv. Tutor.*, vol. 25, no. 4, pp. 2190–2244, 2023.

[59] B. Liu, S. Han, H. Peng, Z. Xiang, G. Sun, and Y. Liang, "A cross-layer analysis for full-duplex ambient backscatter communication system," *IEEE Wirel. Commun. Lett.*, vol. 9, no. 8, pp. 1263–1267, 2020.

[60] W. Liu, K. Huang, X. Zhou, and S. Durrani, "Full-duplex backscatter interference networks based on time-hopping spread spectrum," *IEEE Trans. Wirel. Commun.*, vol. 16, no. 7, pp. 4361–4377, 2017.

[61] G. Yang, D. Yuan, Y. Liang, R. Zhang, and V. C. M. Leung, "Optimal resource allocation in full-duplex ambient backscatter communication networks for wireless-powered IoT," *IEEE Internet Things J.*, vol. 6, no. 2, pp. 2612–2625, 2019.

[62] M. Katanbaf, A. Weinand, and V. Talla, "Simplifying backscatter deployment: Full-duplex lora backscatter," in *18th USENIX Symposium on Networked Systems Design and Implementation, NSDI, April 12-14* (J. Mickens and R. Teixeira, eds.), pp. 955–972, USENIX Association, 2021.

[63] A. Hakimi, S. Zargari, C. Tellambura, and S. P. Herath, "Sum rate maximization of MIMO monostatic backscatter networks by suppressing residual self-interference," *IEEE Trans. Commun.*, vol. 71, no. 1, pp. 512–526, 2023.

[64] D. Mishra and E. G. Larsson, "Monostatic backscattering detection by multiantenna reader," in *53rd Asilomar Conference on Signals, Systems, and Computers, ACSCC* (M. B. Matthews, ed.), pp. 697–701, IEEE, 2019.

[65] T. Wu, M. Jiang, Q. Zhang, Q. Li, and J. Qin, "Beamforming design in multiple-input-multiple-output symbiotic radio backscatter systems," *IEEE Commun. Lett.*, vol. 25, no. 6, pp. 1949–1953, 2021.

[66] J. Xu, Z. Dai, and Y. Zeng, "MIMO symbiotic radio with massive backscatter devices: Asymptotic analysis and precoding optimization," *IEEE Trans. Commun.*, vol. 71, no. 9, pp. 5487–5502, 2023.

[67] R. Long, Y. Liang, H. Guo, G. Yang, and R. Zhang, "Symbiotic radio: A new communication paradigm for passive internet of things," *IEEE Internet Things J.*, vol. 7, no. 2, pp. 1350–1363, 2020.

[68] Q. Zhang, Y. Liang, and H. V. Poor, "Reconfigurable intelligent surface assisted MIMO symbiotic radio networks," *IEEE Trans. Commun.*, vol. 69, no. 7, pp. 4832–4846, 2021.

[69] M. B. Janjua and H. Arslan, "Survey on symbiotic radio: A paradigm shift in spectrum sharing and coexistence," *arXiv preprint arXiv:2111.08948*, 2021.

[70] Y. Liang, Q. Zhang, E. G. Larsson, and G. Y. Li, "Symbiotic radio: Cognitive backscattering communications for future wireless networks," *IEEE Trans. Cogn. Commun. Netw.*, vol. 6, no. 4, pp. 1242–1255, 2020.

[71] J. Zhao, "A survey of intelligent reflecting surfaces (IRSs): Towards 6G wireless communication networks," *arXiv preprint arXiv:1907.04789*, 2019.

[72] Q. Wu, S. Zhang, B. Zheng, C. You, and R. Zhang, "Intelligent reflecting surface-aided wireless communications: A tutorial," *IEEE Trans. Commun.*, vol. 69, no. 5, pp. 3313–3351, 2021.

[73] J. Zuo, Y. Liu, L. Yang, L. Song, and Y. Liang, "Reconfigurable intelligent surface enhanced NOMA assisted backscatter communication system," *IEEE Trans. Veh. Technol.*, vol. 70, no. 7, pp. 7261–7266, 2021.

[74] P. Ramezani and A. Jamalipour, "Backscatter-assisted wireless powered communication networks empowered by intelligent reflecting surface," *IEEE Trans. Veh. Technol.*, vol. 70, no. 11, pp. 11908–11922, 2021.

[75] J. Hu, Y. Liang, and Y. Pei, "Reconfigurable intelligent surface enhanced multi-user MISO symbiotic radio system," *IEEE Trans. Commun.*, vol. 69, no. 4, pp. 2359–2371, 2021.

[76] J. Zhao, J. Ye, S. Guo, Z. Bai, D. Zhou, and A. Mohamed, "Reconfigurable intelligent surface enabled joint backscattering and communication," *IEEE Trans. Veh. Technol.*, 2023.

[77] S. Hu, C. Liu, Z. Wei, Y. Cai, D. W. K. Ng, and J. Yuan, "Beamforming design for intelligent reflecting surface-enhanced symbiotic radio systems," in *IEEE International Conference on Communications, ICC , Seoul, Korea, May 16-20*, pp. 2651–2657, IEEE, 2022.

[78] S. Xu, C. Chen, Y. Du, J. Wang, and J. Zhang, "Intelligent reflecting surface backscatter enabled uplink coordinated multi-cell MIMO network," *IEEE Trans. Wirel. Commun.*, vol. 22, no. 8, pp. 5685–5696, 2023.

[79] X. Jia, X. Zhou, D. Niyato, and J. Zhao, "Intelligent reflecting surface-assisted bistatic backscatter networks: Joint beamforming and reflection design," *IEEE Trans. Green Commun. Netw.*, vol. 6, no. 2, pp. 799–814, 2022.

[80] S. Xu, J. Liu, and J. Zhang, "Resisting undesired signal through IRS-based backscatter communication system," *IEEE Commun. Lett.*, vol. 25, no. 8, pp. 2743–2747, 2021.

[81] J. Wang, S. Xu, S. Han, and J. Li, "Multicast secrecy rate maximization for reconfigurable intelligent surface backscatter communication," *IEEE Commun. Lett.*, vol. 26, no. 12, pp. 2855–2859, 2022.

[82] X. Jia, J. Zhao, X. Zhou, and D. Niyato, "Intelligent reflecting surface-aided backscatter communications," in *GLOBECOM, Virtual Event, Taiwan, December 7-11, 2020*, pp. 1–6, IEEE, 2020.

[83] X. Wang, Z. Fei, and Q. Wu, "Integrated sensing and communication for RIS-assisted backscatter systems," *IEEE Internet Things J.*, vol. 10, no. 15, pp. 13716–13726, 2023.

[84] X. Fang, W. Feng, Y. Chen, N. Ge, and Y. Zhang, "Joint communication and sensing toward 6G: Models and potential of using MIMO," *IEEE Internet Things J.*, vol. 10, no. 5, pp. 4093–4116, 2023.

[85] Q. Tao, X. Hu, S. Zhang, and C. Zhong, "Integrated sensing and communication for symbiotic radio systems in mobile scenarios," *IEEE Trans. Wire. Commun.*, pp. 1–1, 2024.

[86] D. L. Galappaththige, C. Tellambura, and A. Maaref, "Integrated sensing and backscatter communication," *IEEE Wirel. Commun. Lett.*, vol. 12, no. 12, pp. 2043–2047, 2023.

[87] F. Jameel, R. Duan, Z. Chang, A. Liljemark, T. Ristaniemi, and R. Jäntti, "Applications of backscatter communications for healthcare networks," *IEEE Netw.*, vol. 33, no. 6, pp. 50–57, 2019.

[88] *Impinj RFID Reader*, Accessed: Jan. 7, 2019. [Online] Available: http://www.impinj.com/products/readers.

[89] Q. Shi, L. Liu, W. Xu, and R. Zhang, "Joint transmit beamforming and receive power splitting for MISO SWIPT systems," *IEEE Trans. Wirel. Commun.*, vol. 13, no. 6, pp. 3269–3280, 2014.

[90] X. Lu, H. Jiang, D. Niyato, D. I. Kim, and Z. Han, "Wireless-powered device-to-device communications with ambient backscattering: Performance modeling and analysis," *IEEE Trans. Wirel. Commun.*, vol. 17, no. 3, pp. 1528–1544, 2018.

[91] G. Sacarelo and Y. H. Kim, "Beamforming and reflection coefficient control for multi-antenna backscatter communication with non-orthogonal multiple access," *IEEE Access*, vol. 9, pp. 56104–56114, 2021.

[92] D. P. Villame and J. S. Marciano, "Carrier suppression locked loop mechanism for UHF RFID readers," in *IEEE International Conference on RFID (IEEE RFID 2010)*, pp. 141–145, IEEE, 2010.

[93] T. Kim, K. Min, and S. Park, "Self-interference channel training for full-duplex massive MIMO systems," *Sensors*, vol. 21, no. 9, p. 3250, 2021.

[94] A. Ayesha, M. Rahman, A. Haider, and S. Majeed Chaudhry, "On self-interference cancellation and non-idealities suppression in full-duplex radio transceivers," *Mathematics*, vol. 9, no. 12, p. 1434, 2021.

[95] J. D. Griffin and G. D. Durgin, "Complete link budgets for backscatter-radio and RFID systems," *IEEE Antennas and Propagation Magazine*, vol. 51, no. 2, pp. 11–25, 2009.

[96] A. Mohammadian and C. Tellambura, "RF impairments in wireless transceivers: Phase noise, CFO, and IQ imbalance - A survey," *IEEE Access*, vol. 9, pp. 111718–111791, 2021.

[97] C. He, Z. J. Wang, C. Miao, and V. C. M. Leung, "Block-level unitary query: Enabling orthogonal-like space-time code with query diversity for MIMO backscatter RFID," *IEEE Trans. Wirel. Commun.*, vol. 15, no. 3, pp. 1937–1949, 2016.

[98] G. Yang, C. K. Ho, and Y. L. Guan, "Multi-antenna wireless energy transfer for backscatter communication systems," *IEEE J. Sel. Areas Commun.*, vol. 33, no. 12, pp. 2974–2987, 2015.

[99] G. Yang, D. Yuan, Y. Liang, R. Zhang, and V. C. M. Leung, "Optimal resource allocation in full-duplex ambient backscatter communication networks for wireless-powered IoT," *IEEE Internet Things J.*, vol. 6, no. 2, pp. 2612–2625, 2019.

[100] A. Hakimi, S. Zargari, C. Tellambura, and S. Herath, "Sum rate maximization of full-duplex MIMO monostatic backscatter networks under residual self-interference," in *2022 17th Canadian Workshop on Information Theory (CWIT)*, pp. 103–108, IEEE, 2022.

[101] A. N. Parks, A. Liu, S. Gollakota, and J. R. Smith, "Turbocharging ambient backscatter communication," in *ACM SIGCOMM 2014 Conference, SIGCOMM'14, Chicago, IL, USA, August 17-22, 2014* (F. E. Bustamante, Y. C. Hu, A. Krishnamurthy, and S. Ratnasamy, eds.), pp. 619–630, ACM, 2014.

[102] R. Reed, F. L. Pour, and D. S. Ha, "An energy efficient RF backscatter modulator for IoT applications," in *IEEE International Symposium on Circuits and Systems, ISCAS 2021, Daegu, South Korea, May 22-28, 2021*, pp. 1–5, IEEE, 2021.

[103] S. Zargari, M. Kolivand, S. A. Nezamalhosseini, B. Abolhassani, L. R. Chen, and M. H. Kahaei, "Resource allocation of hybrid VLC/RF systems with light energy harvesting," *IEEE trans. green commun. netw.*, 2021.

[104] Y. Zhang, Q. Zhang, Y. Liang, and P. Y. Kam, "A semi-blind receiver for ambient backscatter communications with MPSK RF source," in *2 IEEE/CIC International Conference on Communications in China - Workshops, ICCC Workshops, Changchun, China, August 11-13,*, pp. 71–76, IEEE, 2019.

[105] D. Mishra and E. G. Larsson, "Optimal channel estimation for reciprocity-based backscattering with a full-duplex MIMO reader," *IEEE Trans. Signal Process.*, vol. 67, no. 6, pp. 1662–1677, 2019.

[106] S. Ma, G. Wang, R. Fan, and C. Tellambura, "Blind channel estimation for ambient backscatter communication systems," *IEEE Commun. Lett.*, vol. 22, no. 6, pp. 1296–1299, 2018.

[107] "EPC Radio-Frequency Identity Protocols Generation-2 UHF RFID," October 2013. Ratified.

[108] J. C. Bezdek and R. J. Hathaway, "Convergence of alternating optimization," *Neural, Parallel & Scientific Computations*, vol. 11, no. 4, pp. 351–368, 2003.

[109] Y. Dai and X. Dong, "Power allocation for multi-pair massive MIMO two-way AF relaying with linear processing," *IEEE Trans. Wirel. Commun.*, vol. 15, no. 9, pp. 5932–5946, 2016.

[110] S. Boyd, S. P. Boyd, and L. Vandenberghe, *Convex optimization*. Cambridge university press, 2004.

[111] Z. Luo, W. Ma, A. M. So, Y. Ye, and S. Zhang, "Semidefinite relaxation of quadratic optimization problems," *IEEE Signal Process. Mag.*, vol. 27, no. 3, pp. 20–34, 2010.

[112] Y. Huang and D. P. Palomar, "Rank-constrained separable semidefinite programming with applications to optimal beamforming," *IEEE Trans. Signal Process.*, vol. 58, no. 2, pp. 664–678, 2010.

[113] M. Grant and S. Boyd, "CVX: Matlab software for disciplined convex programming, version 2.1," 2014.

[114] S. Zargari, A. Khalili, Q. Wu, M. Robat Mili, and D. W. K. Ng, "Max-Min fair energy-efficient beamforming design for intelligent reflecting surface-aided SWIPT systems with non-linear energy harvesting model," *IEEE Trans. Veh. Technol*, vol. 70, no. 6, pp. 5848–5864, 2021.

[115] P. C. Weeraddana, M. Codreanu, M. Latva-aho, and A. Ephremides, "Resource allocation for cross-layer utility maximization in wireless networks," *IEEE Trans. Veh. Technol.*, vol. 60, no. 6, pp. 2790–2809, 2011.

[116] P. C. Weeraddana, M. Codreanu, M. Latva-aho, and A. Ephremides, "Resource allocation for cross-layer utility maximization in wireless networks," *IEEE Trans. Veh. Technol.*, vol. 60, no. 6, pp. 2790–2809, 2011.

[117] P. Ubaidulla and A. Chockalingam, "Relay precoder optimization in MIMO-relay networks with imperfect CSI," *IEEE Trans. Signal Process.*, vol. 59, no. 11, pp. 5473–5484, 2011.

[118] M. B. Janjua and H. Arslan, "A survey of symbiotic radio: Methodologies, applications, and future directions," *Sensors*, vol. 23, no. 5, p. 2511, 2023.

[119] H. Guo, R. Long, and Y. Liang, "Cognitive backscatter network: A spectrum sharing paradigm for passive IoT," *IEEE Wirel. Commun. Lett.*, vol. 8, no. 5, pp. 1423–1426, 2019.

[120] S. Y. Park and D. I. Kim, "Intelligent reflecting surface-aided phase-shift backscatter communication," in *IMCOM, Taichung, Taiwan, January 3-5, 2020*, pp. 1–5, 2020.

[121] W. Zhao, G. Wang, S. Atapattu, T. A. Tsiftsis, and C. Tellambura, "Is backscatter link stronger than direct link in reconfigurable intelligent surface-assisted system?," *IEEE Commun. Lett.*, vol. 24, no. 6, pp. 1342–1346, 2020.

[122] G. Yang, X. Xu, Y. Liang, and M. D. Renzo, "Reconfigurable intelligent surface-assisted non-orthogonal multiple access," *IEEE Trans. Wirel. Commun.*, vol. 20, no. 5, pp. 3137–3151, 2021.

[123] X. Mu, Y. Liu, L. Guo, J. Lin, and N. Al-Dhahir, "Exploiting intelligent reflecting surfaces in multi-antenna aided NOMA systems," *arXiv preprint arXiv:1910.13636*, pp. 0090–6778, 2019.

[124] W. Zhao, G. Wang, S. Atapattu, T. A. Tsiftsis, and X. Ma, "Performance analysis of large intelligent surface aided backscatter communication systems," *IEEE Wirel. Commun. Lett.*, vol. 9, no. 7, pp. 962–966, 2020.

[125] Y. Xu, Z. Qin, G. Gui, H. Gacanin, H. Sari, and F. Adachi, "Energy efficiency maximization in NOMA enabled backscatter communications with QoS guarantee," *IEEE Wirel. Commun. Lett.*, vol. 10, no. 2, pp. 353–357, 2021.

[126] J. Zuo, Y. Liu, E. Basar, and O. A. Dobre, "Intelligent reflecting surface enhanced millimeter-wave NOMA systems," *IEEE Commun. Lett.*, vol. 24, no. 11, pp. 2632–2636, 2020.

[127] F. Fang, Y. Xu, Q. Pham, and Z. Ding, "Energy-efficient design of IRS-NOMA networks," *IEEE Trans. Veh. Technol.*, vol. 69, no. 11, pp. 14088–14092, 2020.

[128] S. Zargari, S. Farahmand, B. Abolhassani, and C. Tellambura, "Robust active and passive beamformer design for IRS-aided downlink MISO PS-SWIPT with a nonlinear energy harvesting model," *IEEE Trans. Green Commun. Netw.*, vol. 5, no. 4, pp. 2027–2041, 2021.

[129] Q. Wu, X. Guan, and R. Zhang, "Intelligent reflecting surface-aided wireless energy and information transmission: An overview," *Proc. IEEE*, vol. 110, no. 1, pp. 150–170, 2022.

[130] S. Zargari, A. Khalili, Q. Wu, M. Robat Mili, and D. W. K. Ng, "Max-Min fair energy-efficient beamforming design for intelligent reflecting surface-aided SWIPT systems with non-linear energy harvesting model," *IEEE Trans. Veh. Technol.*, vol. 70, no. 6, pp. 5848–5864, 2021.

[131] M. Grant, S. Boyd, and Y. Ye, "CVX: Matlab software for disciplined convex programming," 2009.

[132] Z. Wang, Y. Liu, X. Mu, Z. Ding, and O. A. Dobre, "NOMA empowered integrated sensing and communication," *IEEE Commun. Lett.*, vol. 26, no. 3, pp. 677–681, 2022.

[133] "3GPP TSG RAN Rel-18 workshop Electronic Meeting," June 28th – July 2nd, 2021.

[134] V. K. Quy, N. V. Hau, D. V. Anh, N. M. Quy, N. T. Ban, S. Lanza, G. Randazzo, and A. Muzirafuti, "IoT-enabled smart agriculture: architecture, applications, and challenges," *Applied Sciences*, vol. 12, no. 7, p. 3396, 2022.

[135] M. H. Alsharif, A. Jahid, A. H. Kelechi, and R. Kannadasan, "Green IoT: A review and future research directions," *Symmetry*, vol. 15, no. 3, p. 757, 2023.

[136] J. Hu, Y.-C. Liang, Y. Pei, S. Sun, and R. Liu, "Reconfigurable intelligent surface based uplink MU-MIMO symbiotic radio system," *IEEE Trans. Wirel. Commun.*, vol. 22, no. 1, pp. 423–438, 2022.

[137] J. Hu, Y. Liang, Y. Pei, S. Sun, and R. Liu, "Reconfigurable intelligent surface based uplink MU-MIMO symbiotic radio system," *IEEE Trans. Wirel. Commun.*, vol. 22, no. 1, pp. 423–438, 2023.

[138] W. Zhou, "Max-min throughput in hybrid of wireless powered NOMA and backscatter communications," *IEEE Access*, vol. 8, pp. 204459–204470, 2020.

[139] Q. Tao, C. Zhong, X. Chen, H. Lin, and Z. Zhang, "Optimal detection for ambient backscatter communication systems with multiantenna reader under complex gaussian illuminator," *IEEE Internet Things J.*, vol. 7, no. 12, pp. 11371–11383, 2020.

[140] H. Guo, Y. Liang, R. Long, S. Xiao, and Q. Zhang, "Resource allocation for symbiotic radio system with fading channels," *IEEE Access*, vol. 7, pp. 34333–34347, 2019.

[141] H. Guo, Y. Liang, R. Long, and Q. Zhang, "Cooperative ambient backscatter system: A symbiotic radio paradigm for passive IoT," *IEEE Wirel. Commun. Lett.*, vol. 8, no. 4, pp. 1191–1194, 2019.

[142] Q. Zhang, L. Zhang, Y. Liang, and P. Kam, "Backscatter-NOMA: A symbiotic system of cellular and internet-of-things networks," *IEEE Access*, vol. 7, pp. 20000–20013, 2019.

[143] R. Long, H. Guo, L. Zhang, and Y. Liang, "Full-duplex backscatter communications in symbiotic radio systems," *IEEE Access*, vol. 7, pp. 21597–21608, 2019.

[144] S. Haghgoy, M. Mohammadi, Z. Mobini, and K.-K. Wong, "Decoupled UL/DL user association in wireless-powered hetnets with full-duplex small cells," *IEEE Trans. Veh.*, 2023.

[145] X. Chen, H. V. Cheng, K. Shen, A. Liu, and M. Zhao, "Stochastic transceiver optimization in multi-tags symbiotic radio systems," *IEEE Internet Things J.*, vol. 7, no. 9, pp. 9144–9157, 2020.

[146] M. Elsayed, A. Samir, A. A. A. El-Banna, X. Li, and B. M. ElHalawany, "When NOMA multiplexing meets symbiotic ambient backscatter communication: Outage analysis," *IEEE Trans. Veh. Technol.*, vol. 71, no. 1, pp. 1026–1031, 2022.

[147] S. Han, Y. Liang, and G. Sun, "The design and optimization of random code assisted multi-BD symbiotic radio system," *IEEE Trans. Wirel. Commun.*, vol. 20, no. 8, pp. 5159–5170, 2021.

[148] D. Li and Y. Liang, "Adaptive ambient backscatter communication systems with MRC," *IEEE Trans. Veh. Technol.*, vol. 67, no. 12, pp. 12352–12357, 2018.

[149] Y. Guo, G. Wang, R. Xu, R. He, X. Wei, and C. Tellambura, "Capacity analysis for wireless symbiotic communication systems with BPSK tags under sensitivity constraint," *IEEE Commun. Lett.*, vol. 26, no. 1, pp. 44–48, 2022.

[150] S. Zargari, A. Hakimi, C. Tellambura, and A. Maaref, "Enhancing ambc systems with deep learning for joint channel estimation and signal detection," *IEEE Trans. Commun.*, vol. 72, no. 3, pp. 1716–1731, 2024.

[151] M. Mohammadi, Z. Mobini, D. Galappaththige, and C. Tellambura, "A comprehensive survey on full-duplex communication: Current solutions, future trends, and open issues," *IEEE Commun. Surv. Tutor.*, 2023.

[152] A. E. Mostafa and V. W. S. Wong, "Connection density enhancement of backscatter communication systems with relaying," in *IEEE Global Communications Conference, GLOBECOM , Virtual Event, Taiwan, December 7-11*, pp. 1–6, IEEE, 2020.

[153] A. Hakimi, S. Zargari, C. Tellambura, and S. Herath, "IRS-enabled backscattering in a downlink non-orthogonal multiple access system," *IEEE Commun. Lett.*, vol. 26, no. 12, pp. 2984–2988, 2022.

[154] Y. Liang and V. V. Veeravalli, "Gaussian orthogonal relay channels: Optimal resource allocation and capacity," *IEEE Trans. Inf. Theory*, vol. 51, no. 9, pp. 3284–3289, 2005.

[155] W. Wang, K. Xu, Y. Yan, and L. Chen, "Relay selection-based cooperative backscatter transmission with energy harvesting: Throughput maximization," *IEEE Wirel. Commun. Lett.*, vol. 11, no. 7, pp. 1533–1537, 2022.

[156] B. Lyu, Z. Yang, H. Guo, F. Tian, and G. Gui, "Relay cooperation enhanced backscatter communication for internet-of-things," *IEEE Internet Things J.*, vol. 6, no. 2, pp. 2860–2871, 2019.

[157] M. Hua, Q. Wu, W. Chen, O. A. Dobre, and A. L. Swindlehurst, "Secure intelligent reflecting surface-aided integrated sensing and communication," *IEEE Trans. Wirel. Commun.*, vol. 23, no. 1, pp. 575–591, 2024.

[158] S. P. Chepuri, N. Shlezinger, F. Liu, G. C. Alexandropoulos, S. Buzzi, and Y. C. Eldar, "Integrated sensing and communications with reconfigurable intelligent surfaces: From signal modeling to processing," *IEEE Signal Process. Mag.*, vol. 40, no. 6, pp. 41–62, 2023.

[159] H. Hua, J. Xu, and T. X. Han, "Optimal transmit beamforming for integrated sensing and communication," *IEEE Trans. Veh. Technol.*, vol. 72, no. 8, pp. 10588–10603, 2023.

[160] Z. Zhu, M. Gong, Z. Chu, P. Xiao, G. Sun, D. Mi, Z. He, and F. Tong, "DRL-based STAR-RIS-assisted ISAC secure communications," in *International Conference on Ubiquitous Communication (Ucom)*, pp. 127–132, IEEE, 2023.

[161] M. Hua, Q. Wu, C. He, S. Ma, and W. Chen, "Joint active and passive beamforming design for IRS-aided radar-communication," *IEEE Trans. Wirel. Commun.*, vol. 22, no. 4, pp. 2278–2294, 2023.

[162] G. Sun, Y. Zhang, W. Hao, Z. Zhu, X. Li, and Z. Chu, "Joint beamforming optimization for STAR-RIS aided NOMA ISAC systems," *IEEE Wire. Commun. Lett.*, 2024.

[163] C. Zhou, B. Lyu, Y. Feng, and D. T. Hoang, "Transmit power minimization for STAR-RIS empowered symbiotic radio communications," *IEEE Trans. Cogn. Commun. Netw.*, vol. 9, no. 6, pp. 1641–1656, 2023.

[164] X. Mu, Y. Liu, L. Guo, J. Lin, and R. Schober, "Simultaneously transmitting and reflecting (STAR) RIS aided wireless communications," *IEEE Trans. Wirel. Commun.*, vol. 21, no. 5, pp. 3083–3098, 2022.

[165] Y. Zou, S. Gong, J. Xu, W. Cheng, D. T. Hoang, and D. Niyato, "Joint energy beamforming and optimization for intelligent reflecting surface enhanced communications," in *IEEE Wireless Communications and Networking Conference Workshops, WCNC Workshops, Seoul, Korea (South), April 6-9,*, pp. 1–6, IEEE, 2020.

[166] S. Hu, Z. Wei, Y. Cai, C. Liu, D. W. K. Ng, and J. Yuan, "Robust and secure sum-rate maximization for multiuser MISO downlink systems with self-sustainable IRS," *IEEE Trans. Commun.*, vol. 69, no. 10, pp. 7032–7049, 2021.

[167] E. Björnson, J. Hoydis, and L. Sanguinetti, "Massive MIMO networks: Spectral, energy, and hardware efficiency," *Found. Trends Signal Process.*, vol. 11, no. 3-4, pp. 154–655, 2017.